

RETURN TO  
SCIENTIFIC & TECHNICAL INFORMATION DIVISION  
(ESTI), BUILDING 1211

ESD ACCESSION LIST

ESTI Call No. *60622*

Copy No. *1*

ESD-TR-68-211  
ESTI FILE COPY

*ESD-TR-68-211*



A Geometrical Theory of Diffraction  
Analysis of the Radar Cross Section  
of a Sectionally Continuous Second-  
Degree Surface of Revolution  
TECHNICAL REPORT-2430-4

Charles E. Ryan

March 1968

*ESSXS*

DEPUTY FOR SURVEILLANCE AND CONTROL SYSTEMS  
ELECTRONIC SYSTEMS DIVISION  
AIR FORCE SYSTEMS COMMAND  
UNITED STATES AIR FORCE  
L. G. Hanscom Field, Bedford, Massachusetts

This document has been  
approved for public release and  
safe; its distribution is  
unlimited.

(Prepared for Contract No. AF 19(628)-67-C-0308 by The Ohio State  
University, ElectroScience Laboratory, Department of Electrical  
Engineering, 1320 Kinnear Road, Columbus, Ohio.)

AD669372

LEGAL NOTICE

When U. S. Government drawings, specifications or other data are used for any purpose other than a definitely related government procurement operation, the government thereby incurs no responsibility nor any obligation whatsoever; and the fact that the government may have formulated, furnished, or in any way supplied the said drawings, specifications, or other data is not to be regarded by implication or otherwise as in any manner licensing the holder or any other person or conveying any rights or permission to manufacture, use, or sell any patented invention that may in any way be related thereto.

OTHER NOTICES

Do not return this copy. Retain or destroy.

**ESD-TA-68-211**

---

A Geometrical Theory of Diffraction  
Analysis of the Radar Cross Section  
of a Sectionally Continuous Second-  
Degree Surface of Revolution  
TECHNICAL REPORT-2430-4

Charles E. Ryan

March 1968

**DEPUTY FOR SURVEILLANCE AND CONTROL SYSTEMS  
ELECTRONIC SYSTEMS DIVISION  
AIR FORCE SYSTEMS COMMAND  
UNITED STATES AIR FORCE  
L. G. Hanscom Field, Bedford, Massachusetts**



This document has been  
approved for public release and  
sale; its distribution is  
unlimited.

(Prepared for Contract No. AF 19(628)-67-C-0308 by The Ohio State  
University, ElectroScience Laboratory, Department of Electrical  
Engineering, 1320 Kinnear Road, Columbus, Ohio.)

---

## FOREWORD

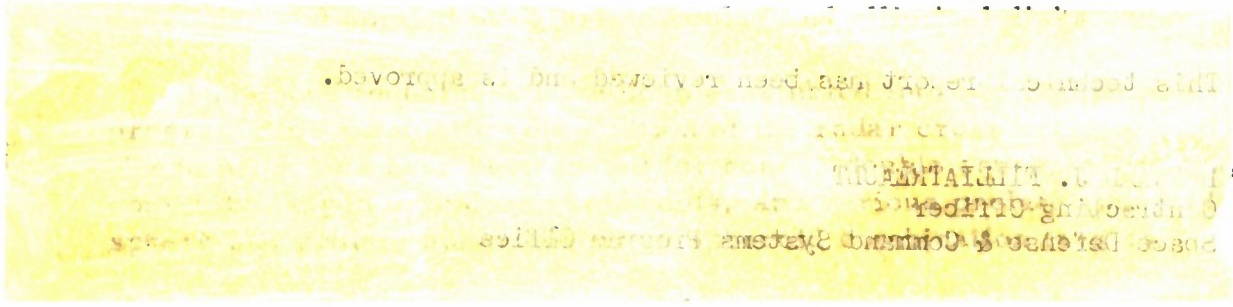
This report, OSURF report number 2430-4, was prepared by The Ohio State University ElectroScience Laboratory, Department of Electrical Engineering, 1320 Kinnear Road, Columbus, Ohio. Research was conducted under Contract F 19628-67-C-0308. Lt. Nyman was the Electronic Systems Division Program Monitor for this research. This report covers the period from 1 January to 31 March 1968.

The author acknowledges the assistance and guidance of his adviser Professor L. Peters, Jr. in the preparation of this report. The comments and suggestions of Professor J. H. Richmond and Professor R. C. Rudduck are also acknowledged. The assistance of Mr. S. A. Redick in obtaining measured data, and the cooperation of the Editorial Staff of the Ohio State University ElectroScience Laboratory is appreciated.

The material contained in this report is also used as a Dissertation submitted to the Department of Electrical Engineering, The Ohio State University as partial fulfillment for the degree Doctor of Philosophy.

## ABSTRACT

The radar cross section of a continuous, convex, body of revolution composed of  $N$  sections, each section described by a second-degree equation has been analyzed using the geometrical theory of diffraction. Wedge diffraction has been applied to determine the scattered field due to discontinuities in slope between sections of the target, and creeping wave theory has been applied to determine the scattered field due to propagation of energy around the target. A solution for the diffracted field on an axial caustic is presented. An approximate solution for the scattered field near and at the normal direction to a conical generator is developed. A "simplified ray path geometry" for the creeping wave is presented and related to the scattering by spheres and prolate spheroids. The H-plane field of the sphere is calculated using creeping wave techniques for a ray geometry defined by the Poynting vector at the shadow boundary. The approximate creeping wave solution for the edge-on backscattering of disks is



## CONTENTS

Chapter		Page
I	INTRODUCTION	1
	A. Components of the Backscattered Field from a Composite Target	1
	B. Description of the Principal Back- scattering Mechanisms	3
	C. Superposition of the Geometrical Optics, Wedge Diffraction and Creeping-Wave Contributions	6
II	GEOMETRICAL OPTICS	9
	A. Ray Optics	9
	B. Specular Scattering of the Reflecting Surface	14
III	WEDGE DIFFRACTION	20
	A. Single Diffraction	20
	B. Diffraction by a Pair of Wedges	30
	C. Multiply Diffracted Rays	36
	D. The Effects of Edge Curvature on Diffracted Rays	41
	E. Correction for Axial Caustics	45
IV	CREEPING WAVE ANALYSIS OF BODIES OF REVOLUTION	55
	A. The Creeping Wave Concept	55
	B. The Creeping Wave Solution for Scattering by a Sphere	59
	C. The Prolate Spheroid	85
	D. The Ogive	94
	E. The Extension of Creeping-Wave Analysis to Disks	105
V	COMPUTER PROGRAM RESULTS	116
	A. Circular Cylinder	118
	B. Cone	120
	C. Double Cone	122

	D. Conically Capped Cylinder	124
	E. Prolate Spheroid	126
	F. Prolate Spheroid-Sphere Combination	127
	G. Prolate Spheroid-Oblate Spheroid Combination	129
VI	CONCLUSIONS	132
Appendix		
I	THE GEOMETRIC PROPERTIES OF A GENERAL SECOND ORDER SURFACE OF REVOLUTION	134
II	DIFFRACTION BY A PERFECTLY CONDUCTING WEDGE	142
III	APPROXIMATION FOR THE SPECULAR SCATTERING BY A GENERATOR OF A CONE	150
IV	THE DETERMINATION OF THE GEODESIC PATHS ON A GENERAL QUADRIC OF REVOLUTION	152
V	THE COMPUTER SOLUTION FOR BACKSCATTER BY A SECTIONALLY CONTINUOUS BODY OF REVOLUTION DESCRIBED BY A SECOND DEGREE EQUATION	154
	REFERENCES	172

## SYMBOLS

### Co-ordinates

$(\xi, \zeta, \eta)$  ray coordinates

$(r, \theta, \phi)$  spherical coordinates system

$\hat{r}, \hat{\theta}, \hat{\phi}$  unit vectors in spherical coordinates

$(\rho, \phi, z)$  cylindrical coordinate system

$\hat{\rho}, \hat{\phi}, \hat{z}$  unit vectors in cylindrical coordinates

### Angles

$\theta, \theta_0, \theta_1, \zeta, \alpha, \beta, \delta$  angles indicated in figures

$\phi$  a phase angle

$\phi_1^p, \phi_1^m, \phi_2^p, \phi_2^m$  angles used as arguments of the diffraction coefficient

$\theta^i, \theta_i$  angles of the incident field

$\theta_d$  angle of the diffracted field

$\alpha, \alpha_1, \alpha_2$  wedge angles

$\beta, \theta', \delta$  angles used to describe diffraction by a curved edge

$\gamma$  half cone angle of the diffraction cone



## SYMBOLS (Cont.)

### Distances

$l_1, l_0, h, L_1, L_2, d, S$  distances indicated in figures

$s$  arc length

$ds$  incremental arc length

$a, a_1, a_2$  radius of a ring

### Constants

$A, A_0, B, C, D$  as indicated in equations

$A_1, \dots, A_{11}$  constants used to describe a general second order surface

$A_{R1}, A_{R3}, B_{R1}, A_{R9}, A_{R10}, A_{R11}$  constants used to describe a general second degree surface of revolution

### Geometrical Parameters

$F(l)$  spatial attenuation factor

$G(s)$  ray path geometry factor

$R$  far field distance

$\rho, \rho_1, \rho_2, \rho_Q, \rho_A, \rho_B$  radii of curvature

$r_s$  normal radius of curvature of a surface

$r^\phi, r^\theta$  principal radii of curvature

$K$  curvature or Gaussian curvature

$K_n$  normal curvature

$K_1, K_2$  principal curvatures

$M$  mean curvature

## SYMBOLS (Cont. )

$A, B, C, D$	surface parameters
$\hat{i}, \hat{t}, \hat{n}, \hat{d},$	unit vectors shown in figures
$\hat{n}$	unit normal vector to a surface
$\sigma_1, \sigma_2$	areas
$\sigma$	echo area
$\hat{v}_i$	incident unit vector

### Electrical symbols

$\epsilon_1, \epsilon_2$	permittivity of the media
$\mu$	permeability of the media
$n$	index of refraction
$k = 2\pi/\lambda$	propagation constant
$\lambda$	wavelength
$Z_0, Y_0$	impedance and admittance of free space respectively
$I^e$	electric current
$I^m$	magnetic current
$E$	the electric field
$E^i, E^s$	incident and scattered electric fields
$E_\theta, E_\phi$	$\theta$ and $\phi$ components of the electric field
$E^{cw}$	creeping wave electric field
$H$	the magnetic field
$H_\theta, H_\phi$	$\theta$ and $\phi$ components of the magnetic field

## SYMBOLS (Cont.)

$\bar{S}$	the Poynting vector
$\omega = 2\pi f$	angular frequency
$\gamma$	complex propagation constant
$R_t, T_t$	reflection and transmission coefficients
$\Gamma, \gamma$	reflection coefficients
$T_{Os}, T_{So}$	transmission coefficients
$p, m$	electric and magnetic dipole moments

### Scalar fields

$v^*(x, \phi)$	geometrical optics field
$v_B(x, n, \phi)$	diffracted scalar field
$u_i, u_D$	incident and diffracted fields
$U_{D_1}, U_{D_2}$	singly diffracted fields
$U_{D_2D_1}, U_{D_1D_2}$	doubly diffracted fields
$U_{TOT}$	a total field
$u(\ell)$	a scalar field

### Diffraction coefficients

$D(r, n, \phi)$	plane wave diffraction coefficient
$V_B(r, n, \phi), v_B(r, n, \phi)$	cylindrical wave diffraction coefficient
$G(n, \phi)$	angular part of the plane wave diffraction coefficient
$D_A, D_B$	creeping wave diffraction coefficients at points A and B

## SYMBOLS (Cont.)

$D_S$	creeping wave diffraction coefficient of the sphere
$D_d$	creeping wave diffraction coefficient for a disk
$D_W$	wedge diffraction coefficient

### Attenuation coefficients

$\alpha_s$	complex attenuation coefficient of a sphere
$\alpha_{og}$	complex attenuation coefficient of an ogive
$\alpha(\rho)$	complex attenuation function

### Miscellaneous

$e$	base of the natural logarithm
$\pi$	ratio of circumference to diameter of a circle
$\Delta(x)$	a small increment on $x$
$P_1, P_2$	points
$\tau$	dummy variable of integration
$P(\zeta)$	a pattern function
$X_0$	an argument of a function
$Q$	a scattering cross section
$f(\theta)$	a scattering amplitude
$J_0(x), J_1(x), J_2(x)$	Bessel functions
$H_v^{(1)}(x)$	Hankel function
$j = \sqrt{-1}$	
$u = 2 ka \sin(\theta)$	

## SYMBOLS (Cont.)

$A_i$	an Airy function
$q_i$	root of an Airy function
$m, N$	integers
$Y, M$	functions
$V_1$	a Foch function
$C_o$	a divergence factor
$w_i$	a function related to the Hankel function
$U(\theta), V(\theta)$	angular functions
$S_1, S_2$	functions
$\bar{r}_u, \bar{r}_v$	partial derivatives of the position vector
$E, F, G, e, f, g$	functions of differential geometry

## CHAPTER I INTRODUCTION

### A. Components of the Backscattered Field from a Composite Target

The determination of the backscattered fields of a composite conducting target is a practical problem of interest. Such a target which may be composed of smooth surfaces, flat facets, edges, fins, and cavities presents a formidable problem in analysis. An exact solution using analytical techniques such as separation of variables is, in general, impractical for such a target. Thus the usual approach to the analysis is by summation of solutions for the backscatter of the component parts of the target. This approach has enjoyed good success in determining the major scattering mechanisms for complex targets. However, previous analysis has been devoted to specified targets. An approach which will apply to a class of targets whose individual characteristics may be varied at will is needed. Several techniques have been developed for the analysis of the general target. These consist of the point-matching computer solution, and the wire grid model computer solution. Both of these approaches yield good results for targets whose electrical size is

small, resulting in a set of  $N$  linear equations which are within the capacity of present digital computers to handle. The "Third Generation" computers with their greatly expanded capabilities promise extension of these techniques to larger targets. However, the time involved in such computations is great resulting in a high cost per data point. Thus a relatively rapid and inexpensive technique would be valuable, especially where real time simulation of radar problems is desirable. An analysis based upon geometrical optics, and the geometrical theory of diffraction, is presented herein which yields approximate results with relatively little expenditure of computer time. This technique is suited to real time computation for simulation of radar problems.

Thus the task of this study consists of assembling known solutions for the particular scattering mechanisms involved, extending these solutions where necessary and applying the solutions in the development of a computer program to determine the monostatic radar cross section for a large class of axially symmetric targets. Future problems involved in extending the computer program include nonsymmetric targets and bistatic scattering. These problems are discussed briefly and it is seen that such extensions are possible using the solutions which have been applied to the restricted class

of targets. The objective of this study is to demonstrate the capability of these techniques in a practical manner.

B. Description of the Principal Backscattering Mechanisms

The principal backscattering mechanisms of a composite target can best be illustrated pictorially. Figure 1 illustrates a composite target viewed by an interrogating radar signal. The numbered positions on the target correspond to different scattering mechanisms

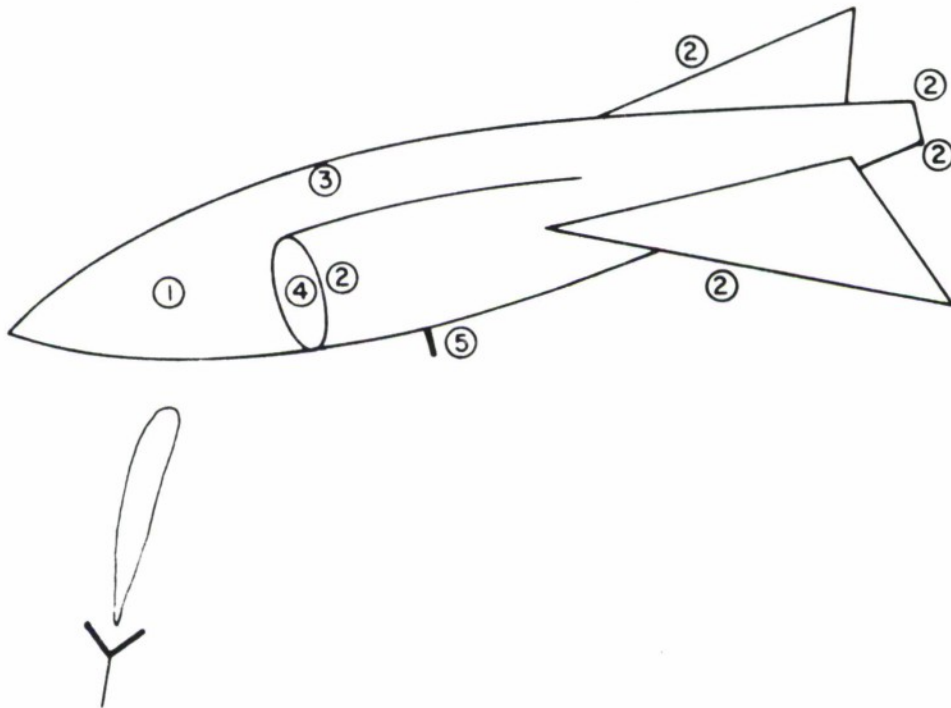


Fig. 1--A general target.



on the target which may contribute to the backscattered field. We divide these mechanisms into five classes as follows:

1. The geometrical optics field

The geometrical optics field results from reflection of the incident energy at the specular point on the target. The resulting contribution to the backscattered field may be evaluated using geometrical optics techniques involving the Gaussian curvature at the specular point. The specular point is defined as that point in the illuminated region where the surface normal is parallel with the direction of incident wave propagation.

The geometrical optics field solution fails for some targets such as the cone, cone sphere junction, and flat plates. For such targets the physical optics solution is required.

2. Wedge diffracted fields

The wedge diffracted fields result from diffraction at slope discontinuities on the target. This contribution can be evaluated using the techniques of the Geometrical Theory of Diffraction developed by Keller[ 1] .

The effects of fins at aspects removed from the normal to the plane of the fin may be evaluated using wedge diffraction techniques. Normal to the plane of the fin the techniques of physical optics may

applied. However, the vertices of fins cannot be treated using the geometrical theory of diffraction as the diffraction coefficient of a vertex is not known.

### 3. Creeping wave fields

The creeping wave backscattered fields arise from that portion of the incident energy which is trapped at the surface of the target, and propagates around the target, eventually reradiating energy in the backscatter direction. These fields may be computed using the geometrical theory of diffraction and knowledge of the differential geometry of the target surface.

### 4. Cavity fields

The cavity fields are caused by concavities in the target which may focus energy as for a corner reflector. The point matching technique[ 2] has been applied to the determination of cavity contributed fields. In some cases these cavity contributions can be analyzed as antenna contributions.

### 5. Antenna mode fields

The antenna contributions are due to antennas on the target which receive and then reradiate energy in the backscatter direction. These contributions can be treated using antenna scattering techniques[ 3, 4] .

It is apparent that an analysis which combines all the scattering mechanisms listed above would be a truly formidable task. It is the purpose of this study to treat the contributions due to the first four mechanisms, i. e. , geometrical optics fields, wedge diffracted fields, fin diffracted fields, and creeping wave fields, for a general convex second degree surface of revolution.

C. Superposition of the Geometrical Optics, Wedge Diffraction and Creeping-Wave Contributions

In order to obtain a solution for the backscattered fields, the contributing mechanisms and their locations on the target must be identified. Thus it is necessary to scan the surface of the target to obtain the specular point, the location of wedges, and the points of attachment and reradiation of the creeping waves. This portion of the solution thus deals with the geometrical properties of the target. In particular, the normal vector to the surface must be calculated in order to determine the location of the specular point and the attachment and reradiation points of the creeping waves. The normal vector is also needed to identify the location and included angle of the wedges. In order to calculate the creeping wave path lengths the differential arc length on the surface is needed as well as the principal radii of curvature at each point along the path. The

Gaussian curvature at the specular point is needed to calculate the geometrical optics field.

Given the geometrical properties of the surface of the target, the solutions for the scattered fields must next be obtained. The specular scattered field is easily obtained from the Gaussian curvature at the specular point. The wedge diffracted fields may be obtained using the Keller[ 1] or Pauli[ 5] solution for wedge diffraction and the ray techniques of the Geometrical Theory of Diffraction. However the creeping wave contributions are not easy to obtain since the complete creeping wave solution is available only for the cylinder and sphere. The behavior of the creeping wave diffraction and attenuation coefficients and the geodesic ray paths are not known for a general body. Thus it is necessary to obtain an approximate solution for the behavior of a creeping wave on a general surface. The effects of ray path geometry on the sphere have been examined in order to obtain an approximate simplified ray path for a general target. Diffraction and attenuation coefficients have been developed empirically for such a simplified ray path and have been shown to yield good results for prolate spheroids, ogives, and disks. The assumption of a simplified ray path on the surface reduces the computation complexity and allows one to reduce the determination of the ray path on a general target to a single numerical iteration of

the differential equation for the geodesic on a surface. In addition, such a simplified ray picture allows one to take into account the effects of intersections on the surface which have discontinuities in the first derivative along the ray path. These effects are treated only in the first order in this study but extension to higher order effects is straightforward.

The determination of the backscattered fields from a general target is thus accomplished by utilizing geometrical optics and wedge diffraction techniques for the illuminated portions of the target and an approximate creeping wave solution for the contributions from the shadow zone of the target. A computer program coded in Fortran IV is the end result of this investigation. This program computes the backscattered fields of a general second order surface of revolution using geometrical optics, wedge diffraction, and creeping wave techniques for the case of parallel polarization, and geometrical optics and wedge diffraction techniques for the case of perpendicular polarization of the incident field. The program is suited for on-line simulation of radar problems. This program has been tested for both canonical shapes and complex targets and the results have been compared to measured data of test targets. Results to date indicate that the computer solution is accurate to within 3 dB of the measured data in the regions where the solutions applied are valid.

## CHAPTER II GEOMETRICAL OPTICS

### A. Ray Optics

The analysis of wave propagation using geometrical optics is based upon the assumption that energy travels along straight lines, called rays, except when modified by reflection or refraction. Orthogonal to the ray trajectories there exists a set of equiphase surfaces. Figure 2 illustrates this orthogonal coordinate set. The relation of geometrical optics to electromagnetic theory has been derived by Luneberg[ 6] through the application of Maxwell's equations and the boundary conditions. For the purposes of this study a brief description of the methods required to calculate the scattered fields of interest will be presented here.

In an isotropic, homogeneous medium the rays are straight lines, and the law of reflection and Snell's law of refraction describe the behavior of the rays at a boundary.

$$(1) \quad \theta_0 = \theta_1 \quad (\text{Law of Reflection})$$

$$(2) \quad \sqrt{\epsilon_1} \sin \theta_0 = \sqrt{\epsilon_2} \sin \theta_2 \quad (\text{Snell's Law}).$$

where  $\epsilon_1, \epsilon_2$  are the permittivities of the media.

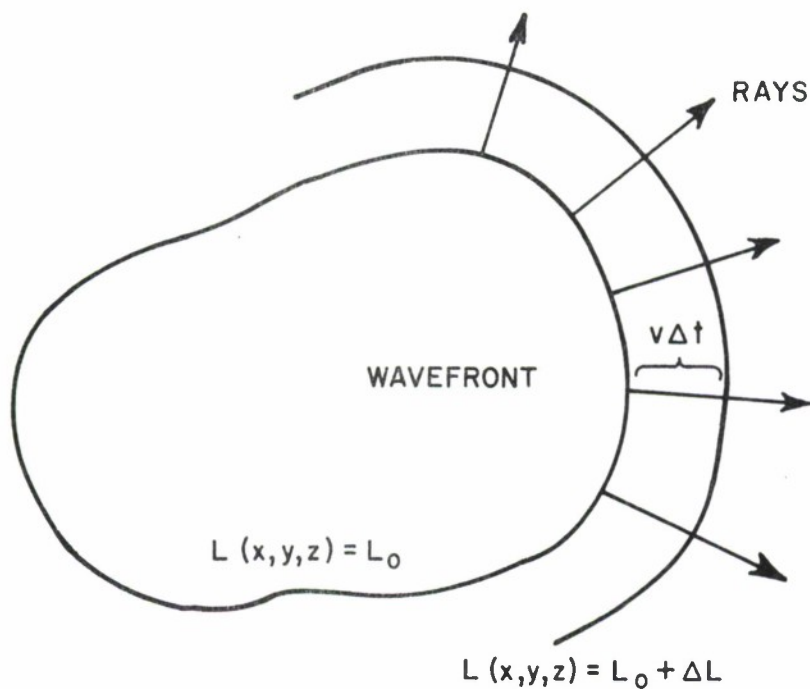


Fig. 2--The relation of rays and wavefronts.

Figure 3 illustrates these laws; the incident, reflected, and refracted rays and the normal to the surface at the point of encounter are coplanar. In the investigation of scattering by conducting bodies the law of reflection is used. However scattering by penetrable bodies such as dielectric spheres requires use of Snell's Law. Such analyses have been performed by Peters and Thomas[ 7] , Kouyoumjian, Peters, and Thomas[ 8] , Swarner and Peters[ 9] , and Peters, Kawano, and Swarner[ 10] .

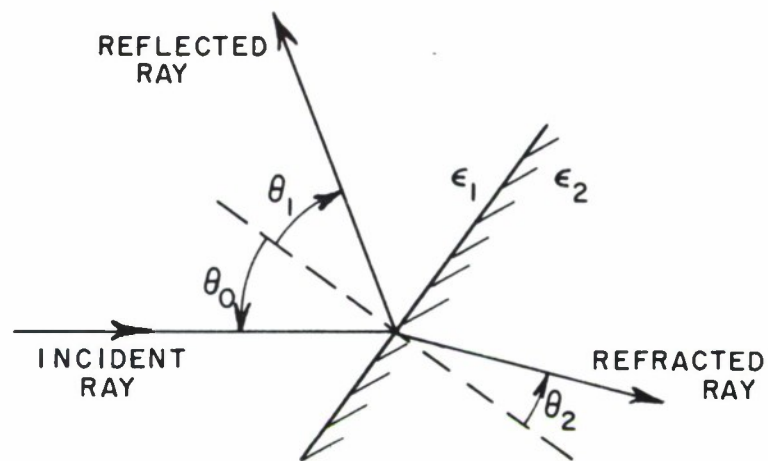


Fig. 3--Reflection and refraction at a boundary between two media

In addition to specifying the ray trajectories it is necessary to account for the amplitude behavior of the field. This is accomplished by applying conservation of energy within the astigmatic flux tube depicted in Fig. 4. It is assumed that the field associated with a particular ray  $u(\ell)$  can be described as

$$(3) \quad u(\ell) = A_0 e^{j\phi} F(\ell) e^{-jk\ell}$$

where

$A_0$  is the amplitude at a reference point,

$\phi$  is the phase at the reference point,

$F(\ell)$  is the spatial attenuation factor, and

$e^{-jk\ell}$  is the phase factor .



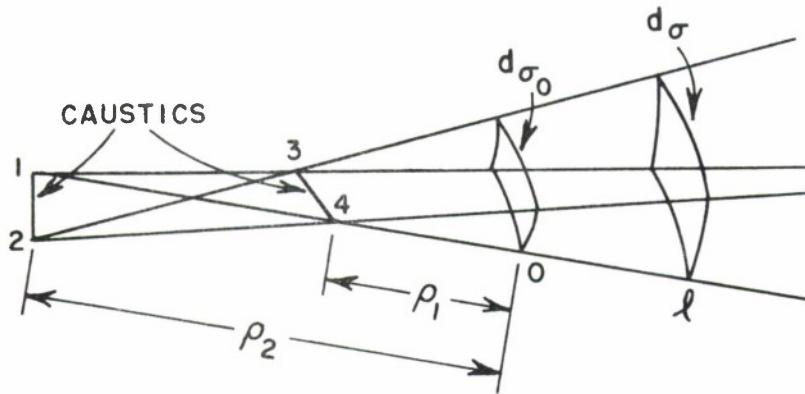


Fig. 4--An astigmatic ray tube

$F(\ell)$  is dependent upon the nature of the reference equiphase surface and accounts for the convergence or divergence of the flux tube in the direction  $\ell$ . The flux tube depicted in Fig. 4 is used to determine  $F(\ell)$  as follows. It is seen that the principal radii of curvature of the cross section  $d\sigma_0$  are  $\rho_1$  and  $\rho_2$ . The field amplitude at the reference point  $O$  is taken to be  $A_0$ , and the field amplitude at the distance  $\ell$  is  $A$ . The energy in the wave is proportional to the square of the amplitude. Applying conservation of energy within the flux tube we have

$$(4) \quad A_0^2 d\sigma_0 = A^2 d\sigma = \text{constant}$$

where  $d\sigma$  is the cross section of the flux tube at  $\ell$ , having principal radii of curvature  $\rho_1 + \ell$  and  $\rho_2 + \ell$ .

The ratio of their areas can be written as

$$(5) \quad \frac{d\sigma}{d\sigma_0} = \frac{(\rho_1 + l)(\rho_2 + l)}{\rho_1 \rho_2} .$$

Inserting this result into Eq. (4) yields

$$(6) \quad F(l) = \frac{A}{A_0} = \sqrt{\frac{\rho_1 \rho_2}{(\rho_1 + l)(\rho_2 + l)}} .$$

The field  $u(l)$  is then

$$(7) \quad u(l) = A_0 e^{j\phi_0} \sqrt{\frac{\rho_1 \rho_2}{(\rho_1 + l)(\rho_2 + l)}} e^{-jkl} .$$

At the locations  $l = -\rho_1$  and  $l = -\rho_2$  the field given by Eq. (7) becomes infinite, and the ray optics solution fails to obtain the correct value of  $u(-\rho_1)$  or  $u(-\rho_2)$ . These locations are termed "caustics" of the geometrical field. In order to calculate the field at such a caustic point Kay and Keller[11] have derived a caustic correction factor. The derivation of such a correction factor proceeds from a solution of the scalar wave equation, and will not be presented here. However, certain results of this derivation are necessary. It has been demonstrated that in the region away from the caustics the geometrical optics solution is correct if a phase shift of  $\left(-\frac{\pi}{2}\right)$  is introduced upon traversal of a caustic line. This phase shift is accounted for by Eq. (7) if the sign of  $l$  is preserved. If

$-\rho_2 < l < -\rho_1$ , i. e., the caustic line has been crossed, then  $\rho_1 + l < 0$ ,  $\rho_2 + l > 0$ , and  $u(l)$  is

$$(8) \quad u(l) = A_0 e^{j\phi_0} \sqrt{\frac{\rho_1 \rho_2}{-(\rho_1 + l)(\rho_2 + l)}} e^{-jkl}$$

$$= A_0 e^{j\phi_0} \sqrt{\frac{\rho_1 \rho_2}{(\rho_1 + l)(\rho_2 + l)}} e^{-j\frac{\pi}{2}} e^{-jkl}$$

and the phase shift is apparent.

If a ray strikes a boundary, and is transformed into reflected and refracted rays with directions specified by the laws of reflection and refraction the values of  $A_0$ ,  $\phi_0$ ,  $\rho_1$ , and  $\rho_2$ , must be determined for both the reflected and refracted rays. In the general case the reflection and transmission coefficients are polarization sensitive except for normal incidence. This polarization sensitivity does not concern us here as the targets to be treated are conducting bodies. However, in the case of penetrable bodies these coefficients must be evaluated ( see for example Thomas[ 12] ).

### B. Specular Scattering of the Reflecting Surface

Consider a ray incident upon a curved surface as shown in Fig. 5. The two dimensional case is illustrated for simplicity. The source of cylindrical rays is a point P located a distance  $l_0$  from point Q, the intercept of the rays and the reflecting surface S.

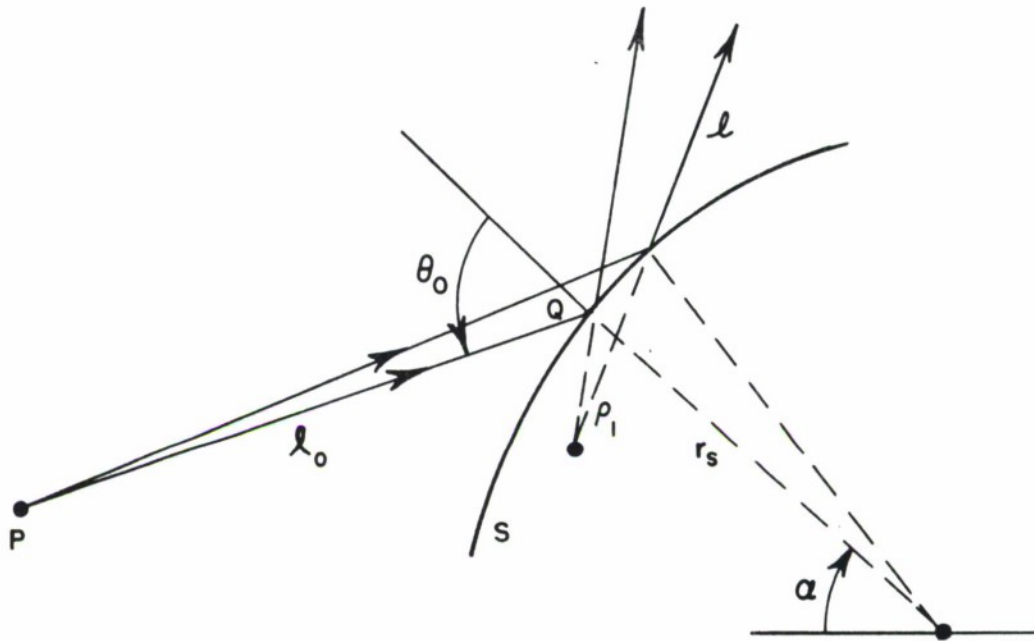


Fig. 5--Reflection by a singly curved surface

The surface has a radius of curvature  $r_s$  at point  $Q$ , and the angle between the incident ray and the surface normal at  $Q$  is  $\theta_0$ . It is now a geometrical problem to determine using the law of reflection, the direction and divergence of the reflected rays. In order to determine the spatial attenuation factor two rays originating at  $P$  are used.

These rays have a small angular deviation  $\beta$ . Provided the angular difference  $\Delta\alpha$  of the reflected rays is small we have

$$(9) \quad l_0 \frac{\Delta(\theta_0 - \alpha)}{\cos \theta_0} = \rho_1 \frac{\Delta(\theta_0 + \alpha)}{\cos \theta_0} = r_s \Delta\alpha \quad .$$

Upon reduction one has

$$(10) \quad \frac{1}{\rho_1} = \frac{2}{r_s \cos \theta_o} + \frac{1}{\ell_o} \quad .$$

Thus we have obtained the caustic distance  $\rho_1$  of the virtual focus in terms of the local radius of curvature of the surface, the reflection angle and the caustic distance of the incident ray.

A similar situation exists for the case of a three-dimensional problem. A three-dimensional problem will involve two caustics of the reflected ray tube (which may not be coincident) similar to the case shown in Fig. 6. The same procedure may be used to obtain the caustic distances by separating the problem into two cylindrical problems. In this case the two principal radii of curvature of the surface at the reflection point are required. The principal radii of curvature may be used in conjunction with Euler's theorem to determine the radius of curvature in a direction which is not coincident with a coordinate direction as noted in Appendix I.

Once the reflection point, angle of reflection and the local radius of curvature are known the divergence factor can be determined. This information in connection with Eq. (10) allows the reflected field to be calculated. In a later chapter it will be demonstrated that these techniques are more generally applicable, specifically to the case of diffraction by a curved edge in connection with the geometrical theory of diffraction.

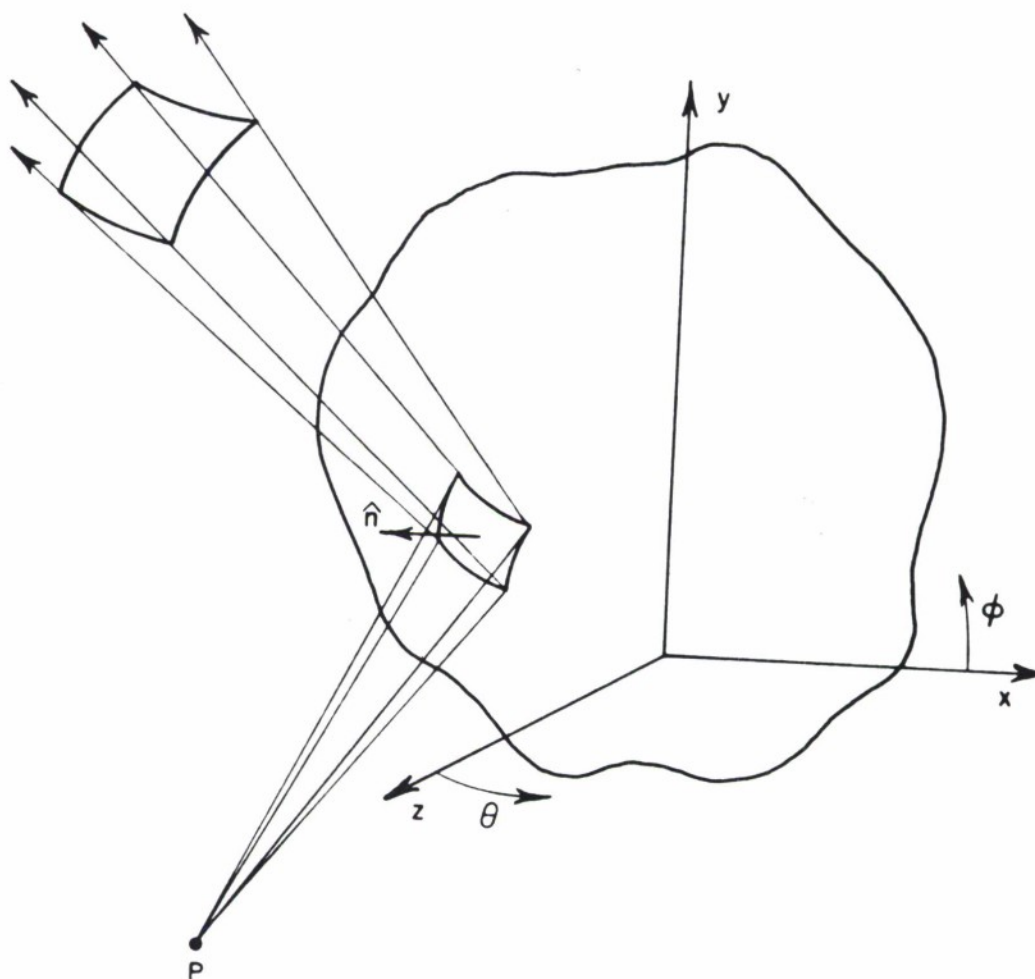


Fig. 6--Reflection by a double-curved surface.

Consider the situation depicted in Fig. 6. A spherical bundle of rays originating at  $P$  is incident upon a three-dimensional surface  $S$  at the reflection point  $Q$ . It is desired to obtain the scattered field through the use of ray optics techniques. Let the coordinate system describing the surface be the spherical system  $(r, \theta, \phi)$ . The rays bounding the incident flux tube can be taken to lie in the  $\theta$  and  $\phi$

planes respectively with no loss in generality. Thus the incremental area of the surface about the reflection point can be written as

$$(11) \quad d\sigma_o = r^2 \sin \theta \, d\theta \, d\phi \quad .$$

We may now separate the problem into two two-dimensional problems.

Referring to Eq. (10) we may determine the caustic distances in terms of the principal radii of curvature  $r^\theta$ ,  $r^\phi$  of the surface as

$$(12) \quad \frac{1}{\rho_1} = \frac{2}{r^\theta \cos \theta_o} + \frac{1}{\ell_o}$$

$$(13) \quad \frac{1}{\rho_2} = \frac{2}{r^\phi \cos \phi_o} + \frac{1}{\ell_o}$$

where  $\theta_o$  and  $\phi_o$  are defined as in Fig. 5 (i. e., they are not polar angles). Thus we may write the reflected (i. e., scattered) field as

$$(14) \quad u(\ell) = A_o e^{j\phi_o} \left[ \frac{\rho_1 \rho_2}{(\rho_1 + \ell)(\rho_2 + \ell)} \right]^{1/2} e^{-jkl} \quad .$$

The case of backscatter (i. e.,  $\theta_o = \phi_o = 0$ ) results in

$$(15) \quad u(\ell) = A_o e^{j\phi_o} \left[ \frac{r^\phi r^\theta \ell_o^2}{(r^\theta \ell_o + \ell)(r^\phi \ell_o + \ell)(2\ell_o + r^\phi)(2\ell_o + r^\theta)} \right]^{1/2} e^{-jkl} \quad .$$

For the case of an incident plane wave ( $\ell_o \rightarrow \infty$ ) the far-zone scattered field ( $\ell \gg 0$ ) is

$$(16) \quad u(l) = \frac{A_0 e^{j\phi}}{2} \sqrt{r_\theta r_\phi} \frac{e^{-jkl}}{l}$$

The spatial attenuation factor appearing in Eq. (15) is seen to be one half the reciprocal of the square root of the Gaussian curvature of the surface at the reflection point. Thus the problem of determining the geometrical optics backscatter from a three-dimensional target reduces to the differential geometry problem of the determination of the Gaussian curvature given in Appendix I.



CHAPTER III  
WEDGE DIFFRACTION

A. Single Diffraction

Consider the case of a perfectly-conducting wedge illuminated by a monochromatic plane wave as illustrated in Fig. 7. According to

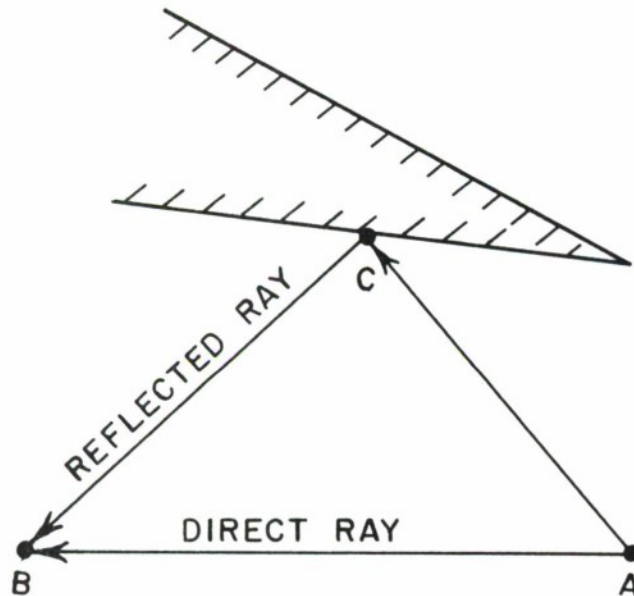


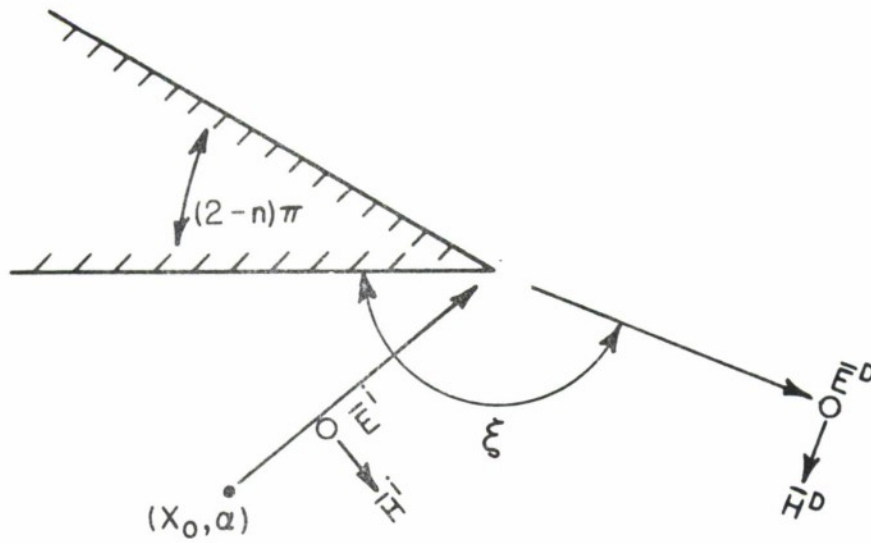
Fig. 7--Geometrical optics rays for cylindrical wave incidence on a wedge

the principles of geometrical optics two classes of rays may exist. These are the direct rays A-B and the reflected rays A-C-B. The behavior of these rays is determined by Fermat's principle which

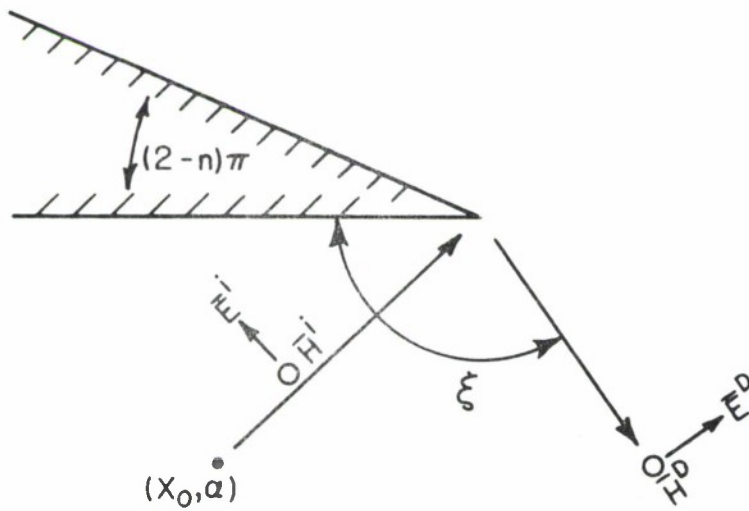
may be stated as follows: "The time elapsed in the passage of light between two fixed points is an extremum with respect to possible paths connecting the points." Or equivalently that the value of the integral between points  $P_1, P_2$  on a path  $s$

$$(17) \quad I = \int_{P_2}^{P_1} n \, ds$$

where  $n$  is the index of refraction of the medium, be an extremum. Keller[ 1] has extended Fermat's principle to edge diffraction in three dimensions through the following assumption: "A singly diffracted ray connecting two points is a curve whose length is stationary among all curves connecting these two points and having one point on the edge." As a consequence of this extended principle, a ray normally incident upon the edge of a wedge generates a family of diffracted rays which lie in a disc having the edge as its axis. Also a ray incident obliquely to the edge of a wedge generates a family of diffracted rays which lie on a cone having the edge as an axis and a half-angle of the cone equal to the angle between the incident ray and the edge. These two cases are shown in Figs. 8 and 9. In addition Keller[ 1] has shown that for diffraction in three dimensions the two-dimensional diffraction coefficients must be modified to take into account the distribution of energy in the cone of diffracted rays.



$$(a) \quad u \Big|_{\text{Boundary}} = 0$$



$$(b) \quad \frac{\partial u}{\partial n} \Big|_{\text{Boundary}} = 0$$

Fig. 8--Diffraction of a cylindrical wave by a wedge.

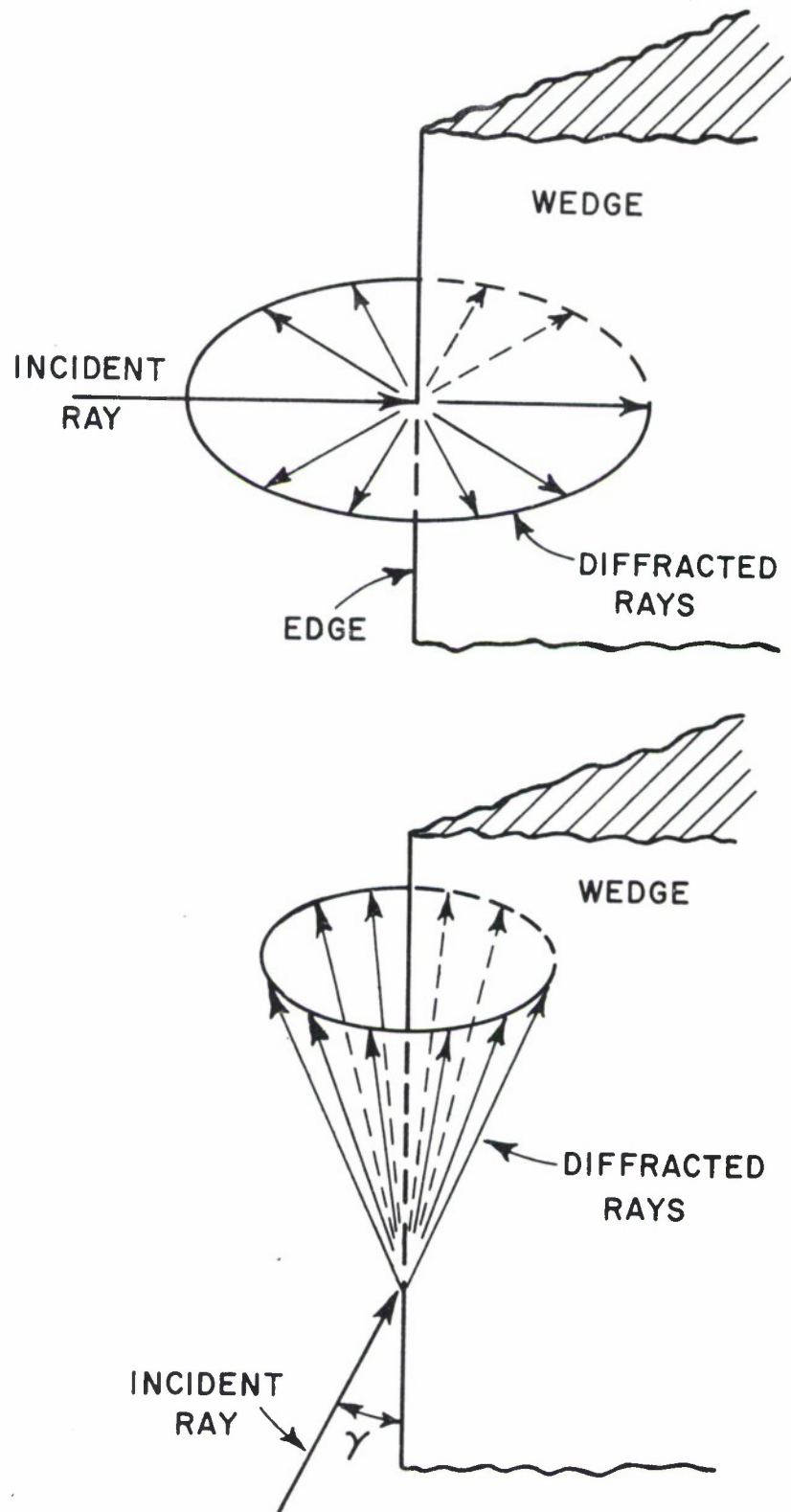


Fig. 9--Three-dimensional picture of the rays diffracted by a wedge.

In the geometrical theory of diffraction the use of ray techniques to describe energy flow is employed in the same manner as in geometrical optics. In fact, the treatment is the same as in geometrical optics, except for diffraction effects which are caused by discontinuities of the structures involved. In conventional geometrical optics, illumination of structural discontinuities causes shadow boundaries about which the field is discontinuous; its unperturbed value is on the illuminated side of the shadow boundary and the null value is on the shadow side. A similar situation exists for the reflected rays for which there is also a shadow boundary. The geometrical theory of diffraction takes into account the diffraction effect of a structural discontinuity by using solutions of canonical problems, and expresses the field more exactly by eliminating the apparent discontinuity of the field at the shadow boundaries introduced by geometrical optics. In particular, the diffraction by a wedge of perfect conductivity is one of the most important canonical problems and is the one employed in this research. The diffracted field introduced by the geometrical theory of diffraction is a cylindrical wave emanating from the edge of the wedge and is described by a diffraction coefficient obtained from the solution to the perfectly conducting wedge problem.

For the two-dimensional case illustrated in Fig. 10, the far-field diffraction for a unit cylindrical wave incident upon a perfectly conducting wedge is given as a sum of geometrical optics ( $v^*$ ) and diffracted ( $v_B$ ) rays as[ 5]

$$(18) \quad u(\xi) = v^*(x_0, \xi - \alpha) \pm v^*(x_0, \xi + \alpha) + v_B(x_0, n, \xi - \alpha) \pm v_B(x_0, n, \xi + \alpha),$$

where the choice of signs is determined by the appropriate boundary condition (- for  $u=0$  and + for the normal derivative of  $u=0$  on the walls) and the variables are defined in Fig. 10. The individual terms are given by[ 5]

$$(19) \quad v^*(r, \phi) = \begin{cases} \exp[jkr \cos \phi], & -\pi + 2\pi nN < \phi < +\pi + 2\pi nN, \\ 0, & \text{otherwise} \end{cases} \quad N = 0, 1, 2, \dots$$

and

$$(20) \quad v_B(r, n, \phi) = \pi^{-\frac{1}{2}} e^{j\frac{\pi}{4}} \left( \frac{1}{n} \sin \frac{\pi}{n} \right) \times \left\{ \frac{2 |\cos(\phi/2)|}{\cos \frac{\pi}{n} - \cos \frac{\phi}{n}} \right\} e^{jkr \cos \phi} \int_0^\infty \frac{e^{-j\tau^2} d\tau}{[kr(1 + \cos \phi)]^{\frac{1}{2}}} + [\text{higher order terms}] .$$

where  $r$  and  $\phi$  are dummy variables. For large values of  $[kr(1 + \cos \phi)]$ ,  $v_B$  can be expressed as

$$(21) \quad v_B(r, n, \phi) = \frac{e^{-j\frac{\pi}{4}} e^{-jkr}}{\sqrt{2\pi kr}} \left\{ \frac{\frac{1}{n} \sin \frac{\pi}{n}}{\cos \frac{\pi}{n} - \cos \frac{\phi}{n}} \right\} \times [1 + ( ) (kr)^{-1} + \dots] .$$

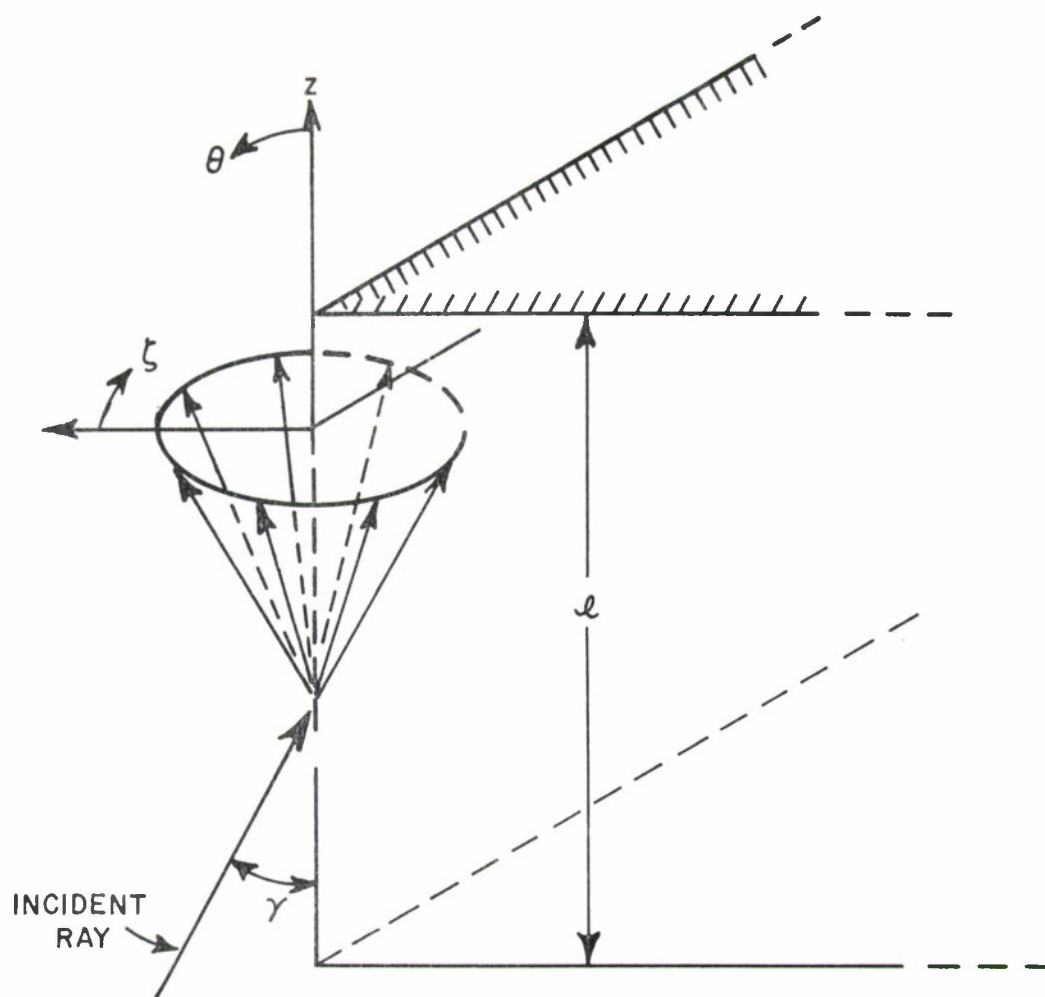


Fig. 10-- Three-dimensional diffraction by a wedge of finite edge length.

Using the first term in the asymptotic expansion given in Eq. (21) we write the diffraction coefficient for plane wave incidence as

$$(22) \quad D(r, n, \phi) = \frac{e^{-j\frac{\pi}{4}} e^{-jkr}}{\sqrt{2\pi kr}} \left\{ \frac{\frac{1}{n} \sin \frac{\pi}{n}}{\cos \frac{\pi}{n} - \cos \frac{\phi}{n}} \right\} .$$

The total diffracted far zone field for plane wave incidence is then

$$(23) \quad u_D(r, n, \phi) = [D(r, n, \phi^-) \pm D(r, n, \phi^+)] u_{\text{incident}} .$$

A detailed discussion of the diffraction coefficient is given in Appendix II.

The diffraction of a spherical wave by an edge has been studied by Oberhettinger[ 13] and also by Nomura[ 14]. Oberhettinger has obtained the diffraction by an infinite wedge for a point source utilizing a Green's function technique. Nomura has obtained the solution for diffraction by an infinite wedge for a dipole source. However the two-dimensional diffraction solution can also be applied to wedge diffraction of a spherically incident field through the use of ray optic techniques. That is, the magnitude of the incident ray is determined using the spatial attenuation factor for a point source rather than that of a line source, and the diffracted field in the plane of the point source and the normal to the wedge is then obtained using Eq. (23). The determination of the diffracted field in other planes requires an extension of the two-dimensional solution to the three-dimensional case. Keller has shown that the extension of Fermat's principle to edge diffraction in three dimensions results in the multiplication of the diffraction coefficient by a factor of  $1/\sin \gamma$  to account for the dispersion of energy in the cone of rays illustrated in Fig. 9.



In addition the source of rays need not be isotropic, but may have a field pattern in the general case. Thus in the application of Eq. (23) to diffraction by a source with a nonuniform pattern, the geometrical optics terms are multiplied by the pattern and the diffraction terms are multiplied by the value of the pattern in the direction of the edge [15]. Thus the far-field form of the diffraction of a source, incident at an angle  $\gamma$  with respect to the edge of a perfectly conducting wedge, is given by

$$\begin{aligned}
 (24) \quad E(\xi) = & \frac{P(\xi)}{\sin \gamma} \{v^*(x_0, \xi - \alpha)\} \\
 & \pm \frac{P(2\pi - \xi)}{\sin \gamma} \{v^*(x_0, \xi + \alpha)\} \\
 & + \frac{P(\xi_0)}{\sin \gamma} \{v_B(x_0, n, \xi - \alpha) \pm v_B(x_0, n, \xi + \alpha)\} \quad ,
 \end{aligned}$$

where  $P(\xi)$  is the pattern of the line source and  $\xi_0 = \pi + \alpha$  is the direction of the edge. The phase reference for Eq. (24) is the edge of the wedge. The pattern of the reflected term is  $P(2\pi - \xi)$ . The factor  $1/\sin \gamma$  expresses the effect of conical diffraction and  $x_0$  is the minimum distance from the source to the edge.

For two-dimensional diffraction the foregoing technique yields diffracted rays which are parallel, having been derived for an infinite edge. This diffraction solution is not valid for a wedge having an edge

of finite length. However it will be assumed that the diffraction pattern in the plane containing the finite edge is the same as the radiation pattern of a line source of finite length. The line source has an excitation determined by the diffraction by an infinite wedge. This assumption takes into account the distribution of energy in three dimensions of the family of parallel diffracted rays due to an edge of finite length. The effects of the finite edge upon the radiation pattern in the plane containing the edge are then calculated by considering a travelling wave on the edge having a phase velocity of  $(k_0 \cos \gamma)$ . Ignoring end effects, the radiation pattern in the plane containing the edge is that of the travelling wave antenna of length  $l$  and phase velocity  $(k_0 \cos \gamma)$ . This pattern can be evaluated using the radiation integral. Thus the total diffraction for a finite wedge shown in Fig. 10 can be approximated as

$$(25) \quad E(\theta, \xi) = E(\xi) \frac{k_0 l}{2} \frac{\sin X_0}{X_0}$$

where  $E(\xi)$  is the excitation obtained using the diffraction coefficient, and

$$X_0 = \frac{k_0 l (\cos \theta - \cos \gamma)}{2} .$$

This technique has been applied successfully in the computation of the radiation pattern of a rectangular waveguide using diffraction techniques[ 16] . The use of the diffraction coefficient in combination

with the radiation integrals allows the determination of the scattered field in three dimensions for a finite wedge.

### B. Diffraction by a Pair of Wedges

The process of diffraction by a pair of interconnected wedges is shown in Fig. 11. It is assumed that an incident plane wave strikes the edge of each wedge of included angles  $\alpha_1$  and  $\alpha_2$ . The incident

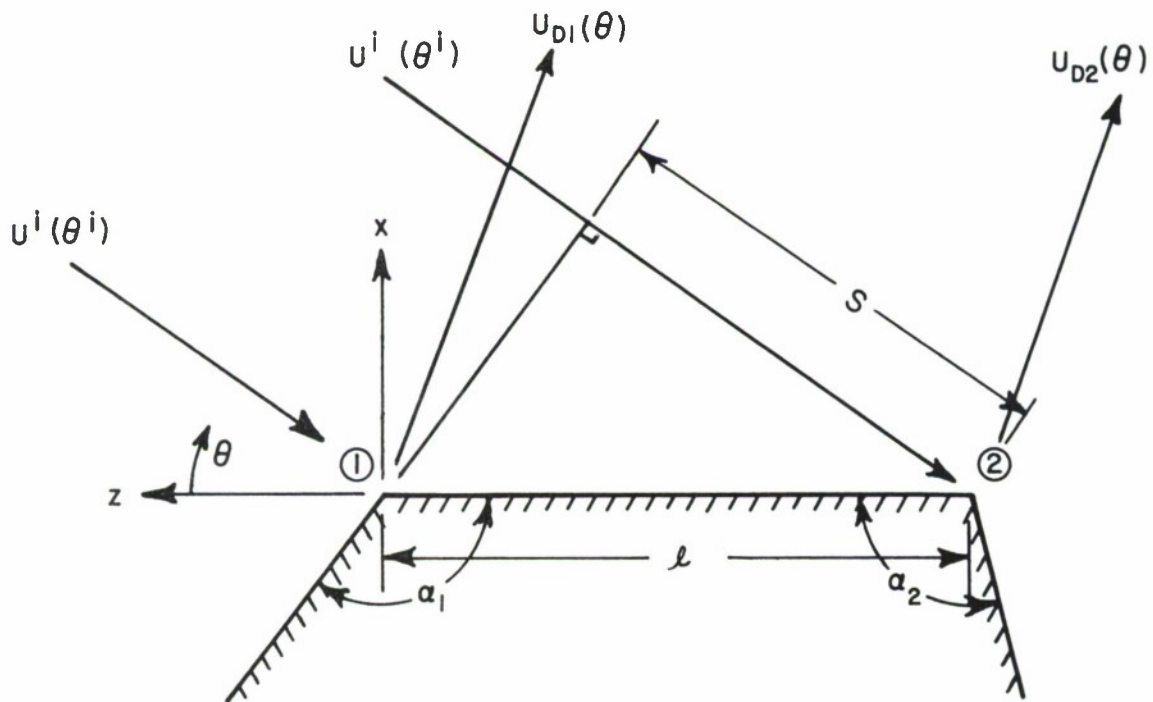


Fig. 11--Single diffraction by a pair of connected wedges.

rays are diffracted giving rise to the singly diffracted rays  $U_{D1}$  and  $U_{D2}$ . These rays may be evaluated using the techniques previously described. In order to calculate higher-order effects an extension of the geometrical theory of diffraction is applied. Namely, diffraction for cylindrical wave incidence is applied to determine the interaction between the wedges.

Since the incident waves are plane waves the plane wave diffraction coefficient is used to calculate the singly diffracted rays. Taking wedge 1 as a phase reference we may write

$$(26) \quad U_{D1}(\theta) = \frac{l}{n_1} \sin \frac{\pi}{n_1} \left[ \frac{l}{\cos \frac{\pi}{n_1} - \cos \frac{\theta^i - \theta}{n_1}} + \frac{l}{\cos \frac{\pi}{n_1} - \cos \frac{2\pi - \theta^i - \theta}{n_1}} \right]$$

and

$$(27) \quad U_{D2}(\theta) = \frac{l}{n_2} \sin \frac{\pi}{n_2} \left[ \frac{l}{\cos \frac{\pi}{n_2} - \cos \frac{\theta - \theta^i}{n_2}} + \frac{l}{\cos \frac{\pi}{n_2} - \cos \frac{\theta + \theta^i}{n_2}} \right] \cdot e^{-jk_0 S} e^{-jk_0 l \cos \theta}$$

where  $(2-n_1)\pi = \alpha_1$ ,  $(2-n_2)\pi = \alpha_2$ ,  $S = l \cos \theta^i$  and the reference for the angles  $\phi^-$ ,  $\phi^+$  is the common surface of the two wedges.

The factor  $e^{-j(kr + \pi/4)} / \sqrt{2\pi kr}$  is omitted as only angular variations are of interest. When the angle of scattering ( $\theta$ ) is equal to the angle of incidence ( $\theta$ ) as in the case of backscatter, Eqs. (26) and (27) become,

$$(28) \quad U_{D1} = \frac{1}{n_1} \sin \frac{\pi}{n_1} \left[ \frac{1}{\cos \frac{\pi}{n_1} - 1} + \frac{1}{\cos \frac{\pi}{n_1} - \cos \frac{2\pi - 2\theta}{n_1}} \right]$$

$$(29) \quad U_{D2} = \frac{1}{n_2} \sin \frac{\pi}{n_2} \left[ \frac{1}{\cos \frac{\pi}{n_2} - 1} + \frac{1}{\cos \frac{\pi}{n_2} - \cos \frac{2\theta}{n_2}} \right]$$

$$\cdot e^{-jkl \cos \theta} \quad e^{-jkl \cos \theta}$$

Figure 12 illustrates the shadow boundary and the reflected waves which exist for plane wave incidence upon the pair of wedges. In the directions of the reflected fields and in the direction of the shadow boundary care must be taken in the evaluation of the total field. In these directions a geometrical optics field exists, and the combination of the terms representing the geometrical optics field and the singly diffracted field to obtain the total field is specified in Appendix II. The behavior of the singly diffracted fields for the case of backscatter when the incident angle  $\theta$  approaches  $\pi/2$  is of interest as it is seen that the expressions for the singly diffracted fields approach infinity as  $\theta$  approaches

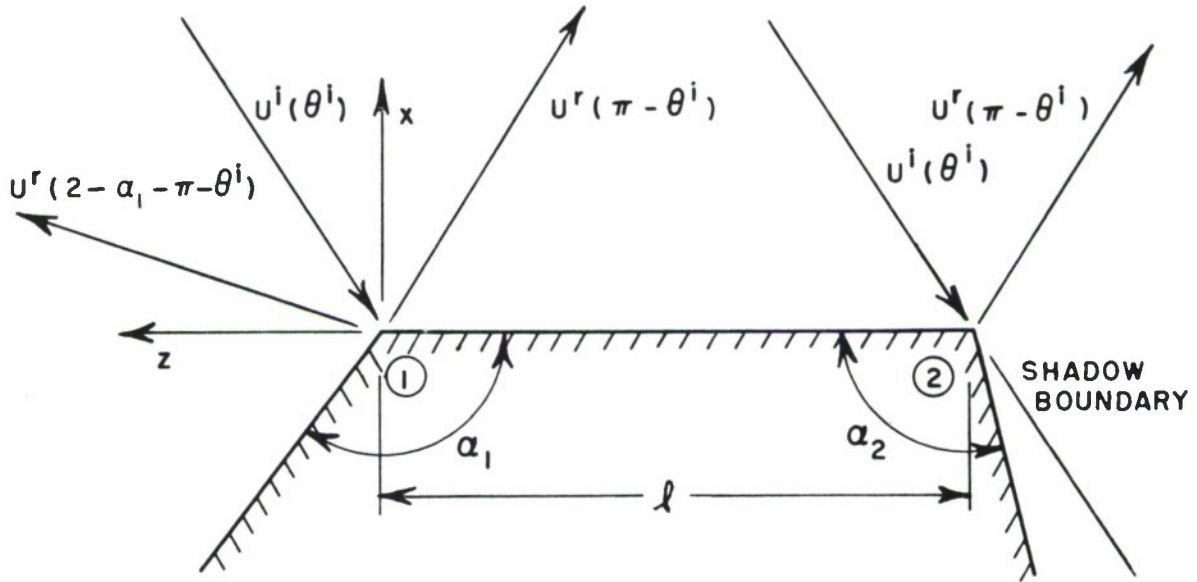


Fig. 12 -- Geometrical optics rays for a pair of connected wedges

$\pi/2$ . If the singly diffracted fields are written in the form of real and imaginary parts, the combination of Eqs. (28) and (29) results in

$$(30) \quad \text{Real}(U_{D1} + U_{D2}) = \cos(kl \cos \theta) \left\{ \frac{1}{n_1} \sin \frac{\pi}{n_1} \left[ \frac{1}{\cos \frac{\pi}{n_1} - 1} \pm \frac{1}{2 \sin\left(\frac{\pi+2\theta}{n_1}\right) \sin\left(\frac{\pi-2\theta}{n_1}\right)} \right] + \frac{1}{n_2} \sin \frac{\pi}{n_2} \left[ \frac{1}{\cos \frac{\pi}{n_2} - 1} \pm \frac{1}{2 \sin\left(\frac{3\pi-2\theta}{n_2}\right) \sin\left(\frac{2\theta-\pi}{n_2}\right)} \right] \right\}$$

$$(31) \quad \text{Imaginary} (U_{D_1} + U_{D_2}) = \sin(kl \cos \theta) \\ \left\{ -\frac{1}{n_1} \sin \frac{\pi}{n_1} \left[ \frac{1}{\cos \frac{\pi}{n_1} - 1} + \frac{1}{2 \sin \left( \frac{\pi+2\theta}{n_1} \right) \sin \left( \frac{\pi-2\theta}{n_1} \right)} \right] \right. \\ \left. + \frac{1}{n_2} \sin \frac{\pi}{n_2} \left[ \frac{1}{\cos \frac{\pi}{n_2} - 1} + \frac{1}{2 \sin \left( \frac{3\pi-2\theta}{n_2} \right) \sin \left( \frac{2\theta-\pi}{n_2} \right)} \right] \right\} .$$

When the real and imaginary parts are placed over least common denominators and the limits taken through application of L'Hospital's rule it is found that the real part diverges while for  $\zeta = \theta - \pi/2$  small the imaginary part becomes

$$(32) \quad \text{Imaginary} (U_{D_1} + U_{D_2}) = \sin(kl \sin \zeta) \\ \left\{ -\frac{1}{n_1} \sin \frac{\pi}{n_1} \left[ \frac{1}{\cos \frac{\pi}{n_1} - 1} + \frac{1}{2 \sin \left( \frac{\zeta+\pi}{n_1} \right) \sin \left( \frac{\zeta}{n_1} \right)} \right] \right. \\ \left. + \frac{1}{n_2} \sin \frac{\pi}{n_2} \left[ \frac{1}{\cos \frac{\pi}{n_2} - 1} + \frac{1}{2 \sin \left( \frac{\pi-\zeta}{n_2} \right) \sin \left( \frac{\zeta}{n_2} \right)} \right] \right\} .$$

Taking the limit as  $\zeta \rightarrow$  small, Eq. (32) becomes

$$(33) \quad \text{Imag} (U_{D_1} + U_{D_2}) = + \left[ \frac{1}{2n_1} \frac{\sin(kl \sin \zeta)}{\sin(\zeta/n_1)} \right. \\ \left. + \frac{1}{2n_2} \frac{\sin(kl \sin \zeta)}{\sin(\zeta/n_2)} \right] \\ = + kl \quad \text{for } \zeta = 0 .$$

Keller[ 1] has examined this problem of determining the scattered field in a geometrical optics region. He presents a solution[ 1] using the "Cross Section Theorem[ 1] " or "Forward Scattering Theorem[ 15] " that states that the forward scattering cross section  $Q$  is

$$( 34) \quad Q = 4\pi /k \operatorname{Im}ag(f(0))$$

where  $f(0)$  is the scattered field amplitude in the forward ( i. e. , geometrical optics) direction. Noting that the geometrical optics scattered fields exists only in the forward and back directions, then  $\operatorname{Im} f(0)$  is the geometrical optics result. Using this theorem Keller[ 1] demonstrates that the cross section obtained using single diffraction may be obtained in this way. He further states that if the geometrical optics terms are included in the evaluation of the scattered field the singularities of the singly diffracted field on the shadow boundaries are cancelled resulting in a finite expression for the scattered field. The behavior of the total field on the shadow boundary is discussed in Appendix II. The proper combination of the diffracted and geometrical optics fields results in continuity of the field across the shadow boundary.

The cross section theorem expressed by Eq. ( 34) yields the geometrical optics cross section if the imaginary part of the singly diffracted field is known. This imaginary part of the field is obtained using the result of Eq. ( 33) and re-introducing the factor  $\frac{e^{-j\frac{\pi}{4}}}{\sqrt{2\pi k}}$  from the diffraction coefficient. The backscattered field in the specular



direction by a body of revolution having the profile shown in Fig. 11, may be obtained using the above results and the spatial attenuation factor. The geometrical optics backscattered field in the specular direction may thus be written as

$$(35) \quad E^s\left(\theta = \frac{\pi}{2}\right) = \frac{k\ell}{\sqrt{2\pi k}} e^{-j\frac{\pi}{4}} \frac{e^{-jkr}}{\sqrt{r}} F(r)$$

where  $F(r)$  is the spatial attenuation factor. An approximate solution for the spatial attenuation factor for a conical generator is presented in Appendix III. In the region close to the specular direction the  $\sin(x)/x$  pattern behavior indicated by Eq. (33) may be used.

### C. Multiply Diffracted Rays

Another class of rays which are of interest are the multiply-diffracted rays. An example of multiple diffraction may be found in the analysis of parallel-plate waveguides by Ryan and Rudduck[ 18] and in coupling between parallel-plate waveguides by Dybdal, Rudduck and Tsai[ 19]. Figure 13 illustrates the doubly-diffracted rays

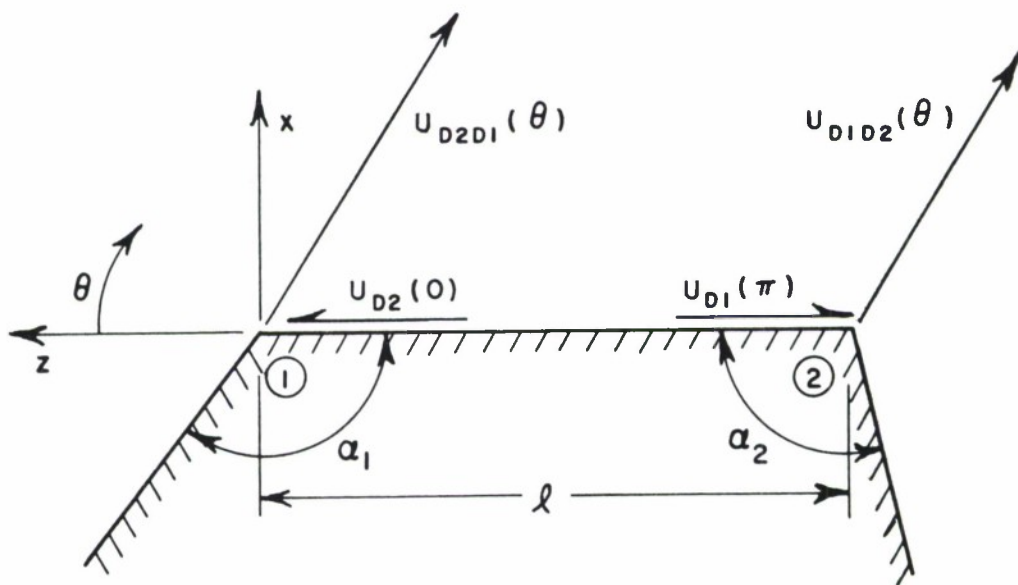


Fig. 13--The multiply diffracted rays for a pair of connected wedges.

$U_{D_2D_1}(\theta)$  and  $U_{D_1D_2}(\theta)$ . These rays arise when a singly diffracted ray is incident upon a wedge and is itself diffracted. In the case depicted in Fig. 13 the doubly diffracted rays may be expressed by assuming that the singly diffracted rays are cylindrical rays emanating from the edge of the wedge. Using the wedge diffraction coefficient for cylindrical fields we may write

$$(36) \quad U_{D_2D_1}(\theta) = U_{D_2}(0) [ v_B(\ell, n_1, \phi_1^m) \mp v_B(\ell, n_1, \phi_1^p) ]$$

and

$$(37) \quad U_{D_1D_2}(\theta) = U_{D_1}(\pi) [ v_B(\ell, n_2, \phi_2^m) \mp v_B(\ell, n_2, \phi_2^p) ]$$

where

$$\phi_1^p = \phi_1^m = \pi - \theta$$

$$\phi_2^p = \phi_1^m = \theta \quad .$$

For spacings between the wedges on the order of two wavelengths or less the doubly diffracted rays are significant as has been demonstrated by Ryan and Rudduck[ 16] , and Dybdal, Rudduck and Tsai[ 19] . It is noted that, just as the singly diffracted rays correct for the discontinuities in the geometrical optics field which arise in the directions of the shadow boundary and reflection boundaries, the doubly diffracted fields correct for the discontinuities in the singly diffracted fields. Thus it is seen in Fig. 13 that the singly diffracted fields  $U_{D_1}(\theta)$  and  $U_{D_2}(\theta)$  have shadow boundaries at  $\theta = \pi$  and 0

respectively. This process continues ad infinitum, that is, the triply-diffracted rays correct discontinuities in the doubly-diffracted rays and so forth. Yu and Rudduck[ 19] have formulated a "Higher-Order Diffraction" technique which allows the effects of all orders of diffraction to be calculated. This self-consistent behavior was first described by Karp and Russek[ 20] . This technique is a self-consistent field technique which generates a system of linear equations. This process can be illustrated using Fig. 13, where it is assumed that the total field diffracted at each wedge can be expressed as the singly diffracted field plus the diffraction field due to all higher orders of diffraction in the form

$$(38) \quad U_{D_1}(\theta) = D_1(\theta) U^i + V_B(\ell, n_1, \phi_1) U_{D_2}(0)$$

and

$$(39) \quad U_{D_2}(\theta) = D_2(\theta) U^i + V_B(\ell, n_2, \phi_2) U_{D_1}(\pi)$$

where

$$(40) \quad \phi_1 = \pi - \theta$$

$$\phi_2 = \theta \quad .$$

In Eqs. (38) and (39) the known quantities are the diffraction coefficients  $D_1(\theta)$ ,  $D_2(\theta)$ ,  $V_B(\ell, n_1, \phi_1)$ ,  $V_B(\ell, n_2, \phi)$ . Setting  $\theta$  equal to  $\pi$  in Eq. (38) and setting  $\theta$  equal to zero in Eq. (39) results in

$$(41) \quad U_{D_1}(\pi) = D_1(\pi) U^i + V_B(\ell, n_1, 0) U_{D_2}(0)$$

$$(42) \quad U_{D_2}(0) = D_2(0) U^i + V_B(\ell, n_2, 0) U_{D_1}(\pi)$$

where

$$(43) \quad D_1(\pi) = \frac{e^{-j(k\ell + \pi/4)}}{\sqrt{2\pi k\ell}} \frac{1}{n_1} \sin \frac{\pi}{n_1} \left\{ \frac{1}{\cos \frac{\pi}{n_1} - \cos \frac{\pi - \theta^i}{n_1}} \right\}$$

$$(44) \quad D_2(\pi) = \frac{e^{-j(k\ell + \pi/4)}}{\sqrt{2\pi k\ell}} \frac{1}{n_2} \sin \frac{\pi}{n_2} \left\{ \frac{1}{\cos \frac{\pi}{n_2} - \cos \frac{\theta^i}{n_2}} \right\}$$

$$\theta^i \neq 0, \pi$$

A set of two equations in the two unknowns  $U_{D_1}(\pi)$ , and  $U_{D_2}(0)$  is determined, thus a solution is obtained for the total diffraction pattern

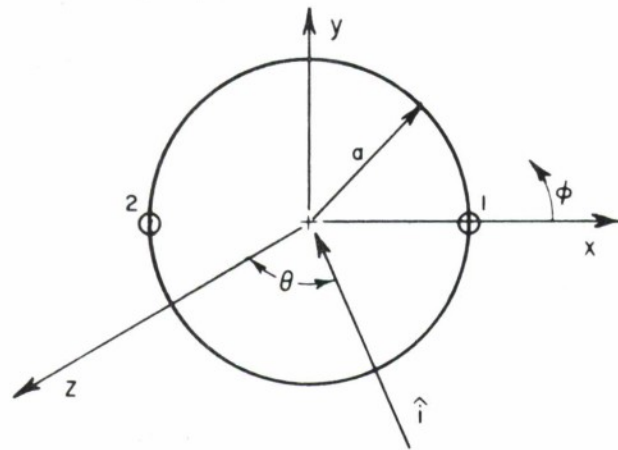
$$(45) \quad U_{\text{tot}}(\theta) = U_{D_1}(\theta) + U_{D_2}(\theta)$$

This form of solution can be extended to the interaction of any number of wedges. In most cases of interest it is not necessary to proceed past the evaluation of the doubly-diffracted fields in order to obtain a satisfactory solution. However the higher order diffraction solution is nearly as simple as the evaluation of the doubly-diffracted rays and is thus the best technique in general.

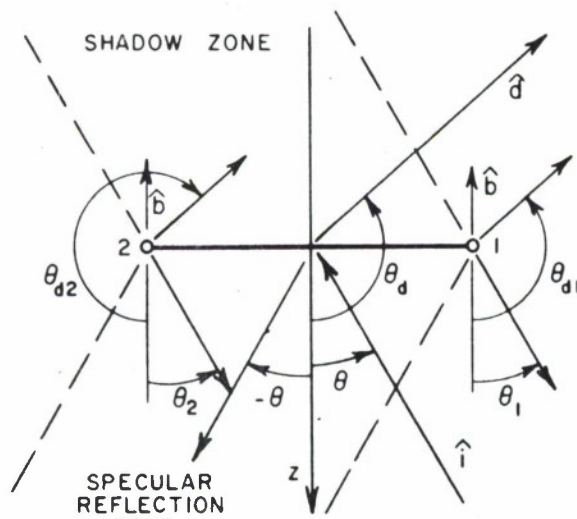
#### D. The Effects of Edge Curvature on Diffracted Rays

In the examples of diffraction above only the case of a straight edge was discussed. In order to apply the wedge diffraction coefficient to more general cases it is necessary to describe the behavior of the incident and diffracted rays for a curved edge. This has been done by DeVore and Kouyoumjian[ 21] and Ufimtzev[ 22] for the circular disk. It is assumed that in the case of the circular disk shown in Fig. 14, the points of diffraction which contribute to the scattered field in the x-z plane are located at  $\phi = 0, \pi$ . It is further assumed that the diffraction coefficient for the infinite edge given previously can be assumed to be valid at points 1 and 2. This assumption is consistent with the property of diffraction being a local phenomenon. The effects of curvature on the behavior of reflected rays has been described previously. This analysis can be extended to diffracted rays using the extension of Fermat's principle. Referring to Fig. 15 we have, after Kouyoumjian[ 23]

$$\begin{aligned}
 (46) \quad \cos \beta &= \hat{i} \cdot \hat{t} & , \quad 0 \leq \beta \leq \pi \\
 -\sin \theta' &= \hat{i} \cdot \hat{n} & , \quad -\frac{\pi}{2} \leq \theta' \leq \frac{3\pi}{2} \\
 \cos \delta &= \hat{d} \cdot \hat{n} & , \quad -\pi \leq \delta \leq \pi
 \end{aligned}$$



(a)



(b)

Fig. 14--Diffraction by a circular disk.

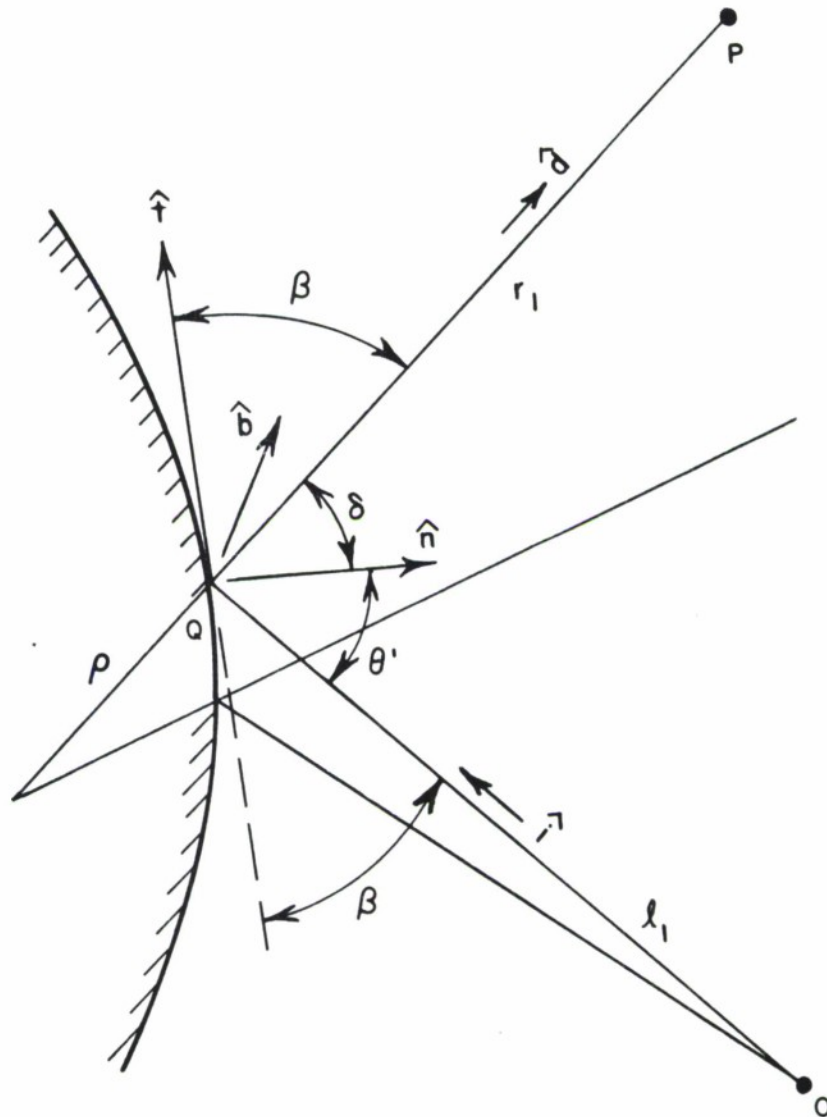


Fig. 15-- Vector relations for diffraction by a curved surface.

where  $\hat{t}$ ,  $\hat{u}$ ,  $\hat{b}$  are the tangent, normal, and binormal vectors of the edge with the tangent and normal vectors in the plane of the screen, and where  $\hat{i}$ ,  $\hat{d}$  are the directions of incidence and diffraction. The half cone angle of the diffracted rays about the positive tangent is  $\beta$ . The distance  $\rho$  between the edge caustic and the second caustic is given by Keller[ 1] as

$$(47) \quad \rho_I = -\rho_Q \sin^2 \beta / (\rho_Q \dot{\beta} \sin \beta + \cos \gamma) \quad .$$



Kouyoumjian[ 23] has given this relation in the form

$$(48) \quad \frac{1}{\rho} = \frac{1}{\ell} - \frac{\hat{n} \cdot (\hat{i} - \hat{d})}{\rho_Q \sin^2 \beta}$$

where  $\rho_Q$  is the radius of curvature of the edge at Q.

In the case of the circular disk shown in Fig. 14, the caustic distances  $\rho_1$ ,  $\rho_2$ , can be obtained from Eq. (48). For an incident plane wave  $\ell_1$  becomes infinite, and for backscatter  $\beta = \pi/2$ .

Thus

$$(49) \quad \frac{1}{\rho_2} = \frac{\sin \theta + \sin \theta_d}{a}, \quad \frac{1}{\rho_2} = - \frac{\sin \theta + \sin \theta_d}{a} .$$

The negative value of  $\rho_2$  means that the caustic is between the edge and the field point. Thus the scattered rays pass through the caustic and a phase jump of  $\pi/2$  is expected to occur at the caustic. This is automatically accounted for by the negative value of  $\rho_2$ .

Equation (48) in combination with ray optics thus allow the determination of the effects of edge curvature upon the diffracted rays. Assuming that the edge diffraction coefficient may be applied at each point along the edge the diffracted fields of a curved edge may be calculated.

### E. Correction for Axial Caustics

In the case of diffraction by a circular aperture or circular disk for an axially incident plane wave each point on the edge contributes to the scattered field on the axis. Thus an infinity of diffracted rays converge on the axis creating a caustic. This effect is also present for the case of diffraction by a slope discontinuity on a body of revolution. In the case of the circular aperture the axis is also the direction of forward scatter and for the case of the circular disk, the axis is the direction of specular reflection. The forward scatter theorem[ 19] allows the determination of the fields in the geometrical optics regions if the diffracted field can be obtained. Keller[ 1] has derived a "caustic correction factor" using an asymptotic solution of the scalar wave equation. By comparison of this solution with the divergent result calculated using the diffraction coefficient and ray optics, he has obtained a correction factor which, when multiplied by the diffraction solution yields the correct solution. This correction factor for a caustic on the z-axis is

$$(50) \quad \text{Corr} = \frac{1}{2} (2\pi k\rho \sin \theta)^{1/2} \sec \left[ k\rho \sin \theta - \left( n + \frac{1}{2} \right) \frac{\pi}{2} \right] J_n(k\rho \sin \theta)$$

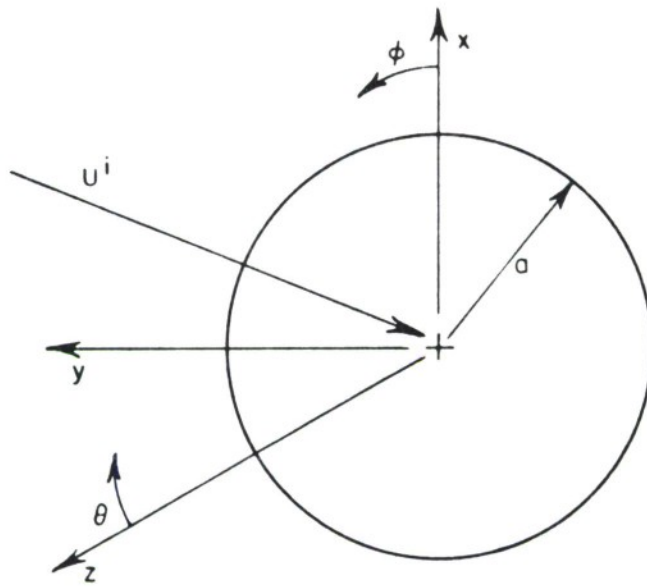
where  $\rho = r \sin \theta$ . If the solution is desired on the caustic ( $\rho = 0$ ), the diffraction solution is first multiplied by the correction factor and the limit as  $\rho$  tends to zero is taken.

Another procedure for obtaining the field on the axis in the geometrical optics region of the circular aperture or disk is to use the equivalent physical optics fields over the aperture (or on the disk) and evaluate the radiation integral for these fields. The case of interest for backscatter is that of backscatter by a circular disk of radius  $a$ , which results in the well-known formula

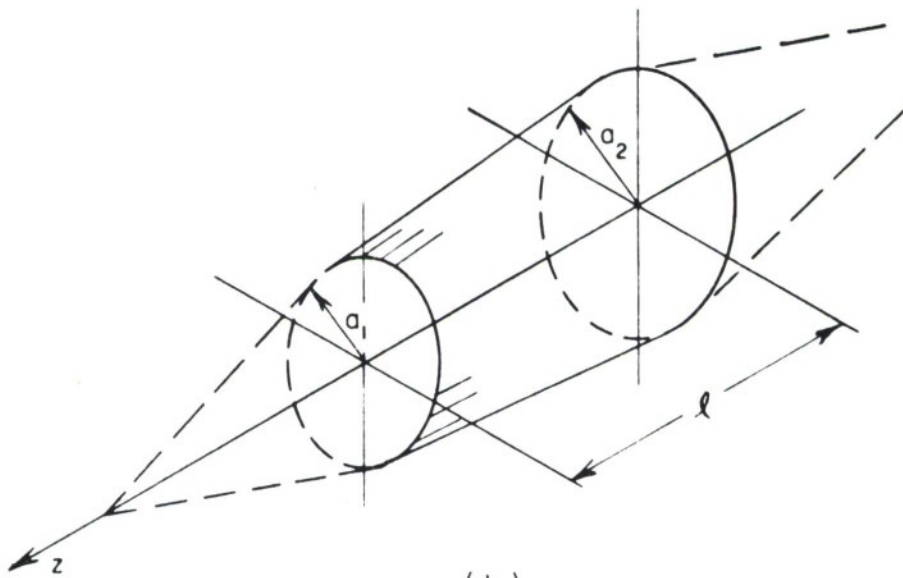
$$(51) \quad E^s = \frac{ka^2}{2} \left[ \frac{2J_1(2ka \sin \theta)}{(2ka \sin \theta)} \right] \cos \theta \quad .$$

The case of axial backscatter by a slope discontinuity on a body of revolution can be treated using a combination of diffraction theory and the radiation integral. The diffraction coefficients are used to specify the diffraction at each point on the "ring" and the radiation integral is used to sum these contributions. In order to obtain the individual contributions at each point the incident wave is decomposed into tangential electric and magnetic fields in the x-y plane at the edge of the ring shown in Fig. 16a. Taking the plane of incidence to be the x-z plane we have for the  $\left\{ \begin{matrix} E \\ H \end{matrix} \right\}$  incidence plane

$$(52) \quad E_{\phi'} = \left\{ \begin{matrix} - \cos \theta \sin \phi' \\ + \cos \phi' \end{matrix} \right\} e^{jka \sin \theta \cos \phi'} E_i$$



(a)



(b)

Fig. 16--Coordinates for the ring source

$$(53) \quad H_{\phi'} = \begin{Bmatrix} -\cos \phi' \\ -\cos \theta \sin \phi' \end{Bmatrix} e^{jka \sin \theta \cos \phi'} H^i \begin{Bmatrix} \text{E plane} \\ \text{H plane} \end{Bmatrix}$$

Applying the diffraction coefficient to these tangential components of the incident field we obtain for the scattered fields at the edge of the ring

$$(54) \quad E_{\phi'}^s = \begin{Bmatrix} -\cos \theta \sin \phi' \\ \cos \phi' \end{Bmatrix} [v_B(r, n, \psi^-) - v_B(r, n, \psi^+)] E^i \cdot e^{jka \sin \theta \cos \phi'}$$

$$(55) \quad H_{\phi'}^s = \begin{Bmatrix} -\cos \phi' \\ -\cos \theta \sin \phi' \end{Bmatrix} [v_B(r, n, \psi^-) + v_B(r, n, \psi^+)] H^i \cdot e^{jka \sin \theta \cos \phi'}$$

where  $\psi^+ = \pi + 2s \cos^{-1} (-\hat{v}_i \cdot \hat{n})$

$$\psi^- = 0$$

$$\hat{v}_i = \text{incident unit vector}$$

$$\hat{n} = \text{unit normal to the surface}$$

$$s = \begin{cases} +1 & \text{if } -\hat{v}_i \times \hat{n} \text{ is } -\hat{y} \text{ directed} \\ -1 & \text{if } -\hat{v}_i \times \hat{n} \text{ is } +\hat{y} \text{ directed} \end{cases}$$

The scattered fields obtained using the diffraction coefficients can be related to equivalent electric and magnetic currents at the edge of the ring using the asymptotic form of the diffraction coefficients and the

far fields of electric and magnetic current filaments[24]. For z-directed filamentary currents we have

$$(56) \quad E_z = -Z_0 k I^e \frac{e^{-j\frac{\pi}{4}}}{2\sqrt{2\pi k\rho}} e^{-jk\rho}$$

$$(57) \quad H_z = -Y_0 k I^m \frac{e^{-j\frac{\pi}{4}}}{2\sqrt{2\pi k\rho}} e^{-jk\rho}$$

where  $Z_0$  and  $Y_0$  are the impedance and admittance of free space respectively. Equating Eqs. (56) and (54), (57) and (55), and using the asymptotic form of the diffraction coefficients given in Eq. (22) results in

$$(58) \quad I^e = -\frac{2}{Z_k} [G(n, \psi^-) - G(n, \psi^+)] \begin{Bmatrix} -\cos \theta \sin \phi' \\ \cos \phi' \end{Bmatrix} e^{jka \sin \theta \cos \phi'} E^i$$

$$(59) \quad I^m = -\frac{2}{Y_k} [G(n, \psi^-) + G(n, \psi^+)] \begin{Bmatrix} -\cos \phi' \\ -\cos \theta \sin \phi' \end{Bmatrix} e^{jka \sin \theta \cos \phi'} H^i$$

$$\text{where} \quad D(r, n, \psi) = \frac{e^{-j\frac{\pi}{4}} e^{-jkr}}{\sqrt{2\pi kr}} G(n, \psi) \quad .$$

These equivalent currents on the edge of the ring apply to the diffracted fields only and do not include geometrical optics terms.

Richmond[25] has presented the radiation integrals for an electric current loop of radius  $a$  as

$$(60) \quad E_{\theta} = - \frac{j\omega\mu a \cos \theta}{4\pi r_0} e^{-jkr_0} \int_0^{2\pi} I^e(\phi') \sin(\phi-\phi') e^{jka \cos(\phi-\phi') \sin \theta} d\phi'$$

$$(61) \quad E_{\phi} = - \frac{j\omega\mu a}{4\pi r_0} e^{-jkr_0} \int_0^{2\pi} I^e(\phi') \cos(\phi-\phi') e^{jka \cos(\phi-\phi') \sin \theta} d\phi' .$$

We may apply the Duality Theorem to obtain the radiated fields in terms of the magnetic current ( $I^m$ ) rather than in terms of the electric current ( $I^e$ ), with the result

$$(62) \quad H_{\theta} = - \frac{j\omega\epsilon a \cos \theta}{4\pi r_0} e^{-jkr_0} \int_0^{2\pi} I^m(\phi') \sin(\phi-\phi') e^{jka \cos(\phi-\phi') \sin \theta} d\phi'$$

$$= -Y_0 E_{\phi}$$

$$(63) \quad H_{\phi} = - \frac{j\omega\epsilon a}{4\pi r_0} e^{-jkr_0} \int_0^{2\pi} I^m(\phi') \cos(\phi-\phi') e^{jka \cos(\phi-\phi') \sin \theta} d\phi'$$

$$= Y_0 E_{\theta} .$$

In the case of backscatter close to the z-axis  $\theta = \theta^i$  with  $\theta$  small, and we take  $\psi^+ = \pi - 2 \cos^{-1}(\hat{z} \cdot \hat{n})$  (i. e.,  $\theta = 0$ ) in the diffraction coefficients. Substituting the edge currents given by Eqs. (58) and (59) into the radiation integrals we determine the backscattered fields. After some manipulation we obtain for the E-plane,

$$(64) \quad E_{\theta}^s = -jaE^i \frac{e^{-jkr}}{r} \left\{ -\cos^2 \theta [G(n, \psi^-) - G(n, \psi^+)] \frac{J_1(u)}{u} + [G(n, \psi^-) + G(n, \psi^+)] \left[ \frac{J_1(u)}{u} - J_2(u) \right] \right\}$$

and for the H-plane,

$$(65) \quad H_{\phi}^s = -jaE^i \frac{e^{-jkr}}{r} \left\{ +\cos^2 \theta [G(n, \psi^-) + G(n, \psi^+)] \frac{J_1(u)}{u} - [G(n, \psi^-) - G(n, \psi^+)] \left[ \frac{J_1(u)}{u} - J_2(u) \right] \right\}$$

where  $u = 2ka \sin \theta$ .

For backscatter on the z-axis (i. e., on the Caustic) we have

$$(66) \quad E_{\theta}^s = -jaE^i G(n, \psi^+) \frac{e^{-jkr}}{r} .$$

Thus, in the case of backscatter Eqs. (51) and (66) allow the computation of the axial scattered field due to a "ring" slope discontinuity. A similar integration could be performed for non-circular slope discontinuities.



If the z-axis is a geometrical optics region we must apply the cross section theorem[ 1] in order to obtain the axial scattered field, and thus determine the equivalent currents on the ring. In order to do this we combine the integrals of Eqs. ( 60) and ( 63) to obtain for the E-plane,

$$(67) \quad E_{\theta}^s = -\frac{ja}{2\pi r} e^{-jkr} \int_0^{2\pi} \left\{ \cos^2 \theta \sin \phi' \sin(\phi - \phi') \right. \\ \cdot \left[ \frac{1}{\cos \frac{\pi}{n} - 1} - \frac{1}{\cos \frac{\pi}{n} - \cos \frac{\pi + 2\zeta}{n}} \right] e^{jka \sin \theta \cos \phi'} \\ + \cos \phi' \cos(\phi - \phi') \left[ \frac{1}{\cos \frac{\pi}{n} - 1} + \frac{1}{\cos \frac{\pi}{n} - \cos \frac{\pi + 2\zeta}{n}} \right] \\ \left. e^{jka \sin \theta \cos \phi'} e^{jka \sin \theta \cos(\phi - \phi')} d\phi' \right\}$$

where  $\zeta = \sin^{-1}(\sin \theta \cos \phi')$  .

Expressing the diffracted fields in terms of real and imaginary parts and applying the cross section theorem[ 1] results in

$$(68) \quad E_{\theta}^s = -\frac{ja}{2\pi r} e^{-jkr_0} \int_0^{2\pi} \left\{ -\cos^2 \theta \sin^2 \phi' \left[ \frac{1}{\cos \frac{\pi}{n} - 1} - \frac{1}{\cos \frac{\pi}{n} - \cos \frac{\pi + 2\zeta}{n}} \right] \right. \\ + \cos^2 \phi' \left[ \frac{1}{\cos \frac{\pi}{n} - 1} + \frac{1}{\cos \frac{\pi}{n} - \cos \frac{\pi + 2\zeta}{n}} \right] \left. \right\} \sin(2ka \sin \theta \cos \phi') \\ d\phi' .$$

Taking the limit as  $\theta \rightarrow 0$ , and performing the integration results in

$$(69) \quad E_{\theta}^s = \frac{-jka^2}{2} \frac{e^{-jkr_0}}{r_0} \quad .$$

Which agrees with the physical optics on-axis result for a disk given by Eq. (51). The physical optics solution is accurate within 3 dB for  $a/\lambda > 0.5$  [23].

The scattered field predicted for a ring, as given by Eq. (66), may be in error if higher-order diffraction terms are significant. However these terms can be evaluated and their contribution computed in the form of Eq. (66).

A particular case of interest is where several "rings" contribute to the near-on-axis field. Such a case is illustrated by a cylinder, or by a conically capped cylinder. For the case of the cylinder the specular return from the flat end would be dominant, and the contribution of the rear "ring" can be neglected. In the case of the conically capped cylinder, the contribution from the cylinder end can be significant with respect to the contribution from the "ring" formed by the cone-cylinder junction. In such a case the total field is the sum of the individual contributions of the "rings". In evaluating the contribution from each ring the integration limits must define the illuminated region. Thus in the case of the rear "ring" of a cylinder these limits would be  $\pm \frac{\pi}{2}$ . For "rings" of

radius  $a$  separated by a length  $\ell$  as illustrated by Fig. 16 b the scattered field is then

$$(70) \quad E_{\theta}^s = E_{\theta,1}^s + \frac{1}{2} e^{-j2k\ell \cos \theta} E_{\theta,2}^s$$

where the subscripts 1 and 2 refer to the front and rear rings respectively and  $E_{\theta,i}^s$  is defined by Eq. (64), and the phase reference is at the front "ring".

If the on-axis field is desired, the limit of Eq. (70) as  $\theta \rightarrow 0$  may be taken. Equivalently, the incident field specified by diffraction along the shadow boundary (i. e.,  $\frac{1}{2} E^i$ ) may be used and the integration limits extended to  $0-2\pi$ . In the second case it is necessary to evaluate the scattered field at a small angular distance from the axis in order to avoid higher order diffraction from the front "ring".

If the radii of the rings differ, as for a conical frustrum, the contribution of the second ring must be evaluated using an integration over the illuminated portion of the ring.

## CHAPTER IV CREEPING WAVE ANALYSIS OF BODIES OF REVOLUTION

### A. The Creeping Wave Concept

The concept of creeping waves was introduced by Franz and Depperman[ 26, 27] for the interpretation of the scalar solution for diffraction by a circular cylinder or a sphere. Senior and Goodrich[28 ] have obtained a representation similar to that of Franz and Depperman through the application of the Watson transformation to the Mie series solution for the sphere. Kouyoumjian[ 29] has presented a creeping wave solution for the sphere which includes all higher-order modes.

A general illustration of the creeping wave format is shown in Fig. 17. An incident plane wave is diffracted at a point of tangency (designated A) on the target. A portion of the diffracted energy is trapped at this point, resulting in a wave which propagates on the surface of the target, shedding energy by radiation as it progresses. Finally, this wave reradiates at B in the scattering direction of interest. This "creeping wave" can thus be described by diffraction coefficients at the points of diffraction and

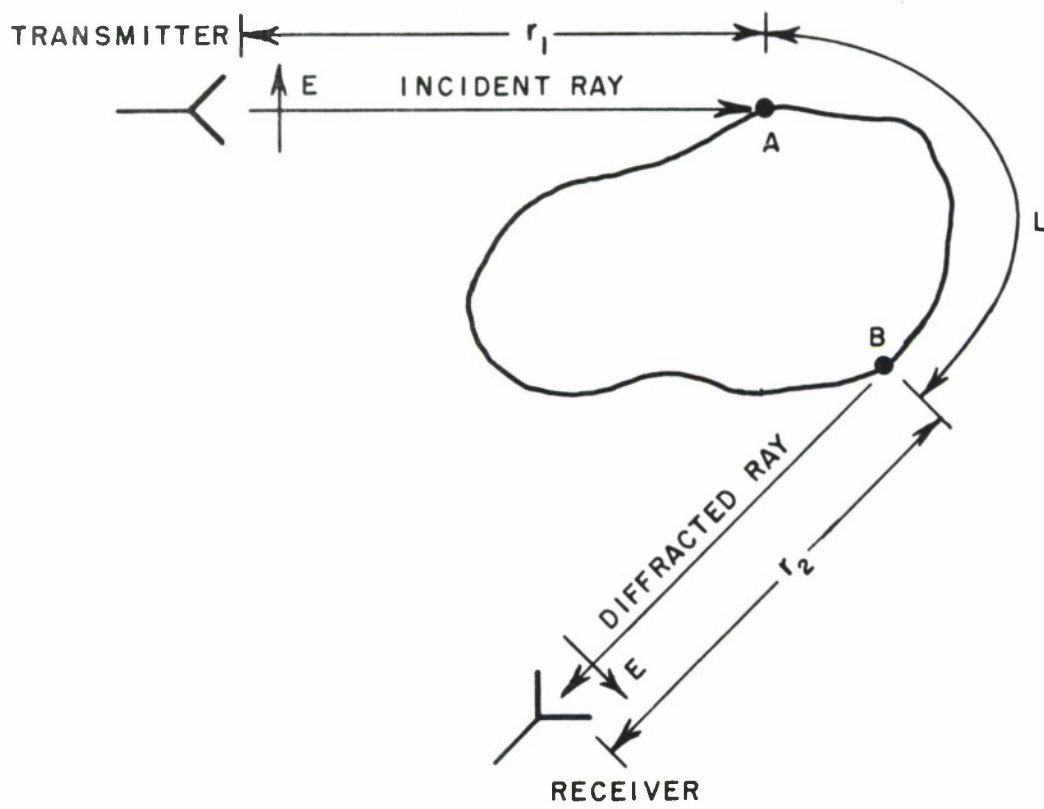


Fig. 17--General concept of the scattered field due to creeping waves.

reradiation, by an attenuation factor to account for radiation losses, and by a description of the ray path geometry on the target traversed by the creeping wave. Thus we write, a general form for the creeping wave scattered field as

$$(71) \quad E_{cw}^s = D_A D_B G(s) e^{-\int_A^B \gamma(s) ds}$$

where  $E_{cw}^s$  is the creeping-wave scattered field

$D_A$  is the diffraction coefficient at A

$D_B$  is the diffraction coefficient at B

$\gamma(s)$  is the creeping-wave propagation factor

$s$  is the arc length along the path

$G(s)$  is the convergence factor for the surface rays.

The primary task is the determination of these diffraction, attenuation and ray path factors for a general body. However this does not appear feasible. Thus it is necessary to evaluate these factors for canonical targets whose exact solutions are available, i. e., the cylinder and sphere. In order to obtain a more general solution for these factors it is necessary to utilize experimental data to obtain an empirical solution for more general targets such as the prolate spheroid. It is the purpose of this chapter to examine both the exact and empirical solutions for the sphere in order to

formulate a solution for the more general target. It will be demonstrated that a rather simple approach yields accurate results for a large class of targets.

The form of the simplified creeping wave analysis desired is such that the convergence factor expressed in Eq. (71) may be taken equal to unity, i. e. , no convergence or divergence of rays need be considered. In addition, it is desired to evaluate the creeping wave contribution due to all creeping waves by evaluation of Eq. (71) for a single equivalent creeping wave. The simplified analysis thus uses a single equivalent non-divergent (or non-convergent) creeping wave to construct the approximate solution for the scattered field. In order to demonstrate the validity of the simplified creeping wave solution it is necessary to identify the major creeping wave contributors in existing creeping wave solutions. Consequently the surface fields of a target, for which the exact surface fields are known, has been examined. In particular, the solution of interest is that for the sphere.

## B. The Creeping Wave Solution for Scattering by a Sphere

The analysis of the scattering by a sphere has been one of the most important problems in electromagnetic theory. The classical solution of Mie using separation of variables and series techniques is the basic starting point for casting the exact solution into the asymptotic form on which the creeping wave format is based. The analysis of Senior and Goodrich[ 27] is an illustration of this adaption. A recent paper by Hong[ 30] gives a derivation which is more closely related to the geometrical properties of the ray paths, deriving the attenuation and diffraction coefficients based upon the properties of the ray paths from the exact solution. Hong's analysis yields the higher-order correction terms for the cylinder and sphere but is not applicable to more general bodies. Hong restricts the ratio of radii of curvatures in the propagation and orthogonal directions to be less than or equal to unity. This restriction limits his analysis to the cylinder and sphere. Keller and Levy[ 31, 32] have also treated this problem. Kinber[ 33] has developed a general technique using a "semi-geodetic" ray coordinate system which applies to bodies of revolution and has used this technique to develop a creeping wave analysis of the sphere[ 34]. Moreland, Peters, and Kilcoyne[ 34]



have adopted a different approach which is empirical in nature and utilizes a simplified ray path geometry. These solutions and their adaption to more general targets will be discussed briefly.

The analyses of Kouyoumjian[29] and Hong[30] are based upon the concept that the incident energy is diffracted at the shadow boundary, and a portion of this energy becomes attached to the surface of the sphere. This trapped (or creeping) wave traverses the sphere on a geodesic (a great circle route) specified by the direction of the incident ray shedding energy tangentially as it progresses, finally contributing to the backscattered field as depicted in Fig. 18. The great circle paths are assumed to intersect the back point of the sphere, forming a caustic at that point. A consequence of this ray path picture is that in the directions of axial scatter a line caustic is formed. In the analysis of Keller this requires the evaluation of a "caustic correction factor" for axially scattered fields. Also this picture does not account for the magnitude of the field in the minor creeping wave plane as noted by Kazarinoff and Senior[36]. In each of these analyses the results for the echo area of the sphere are in good agreement with the exact solution. The diffraction and attenuation coefficients derived by Keller and Levy[31,32] are carried out to first order while the forms given by Hong[30] and

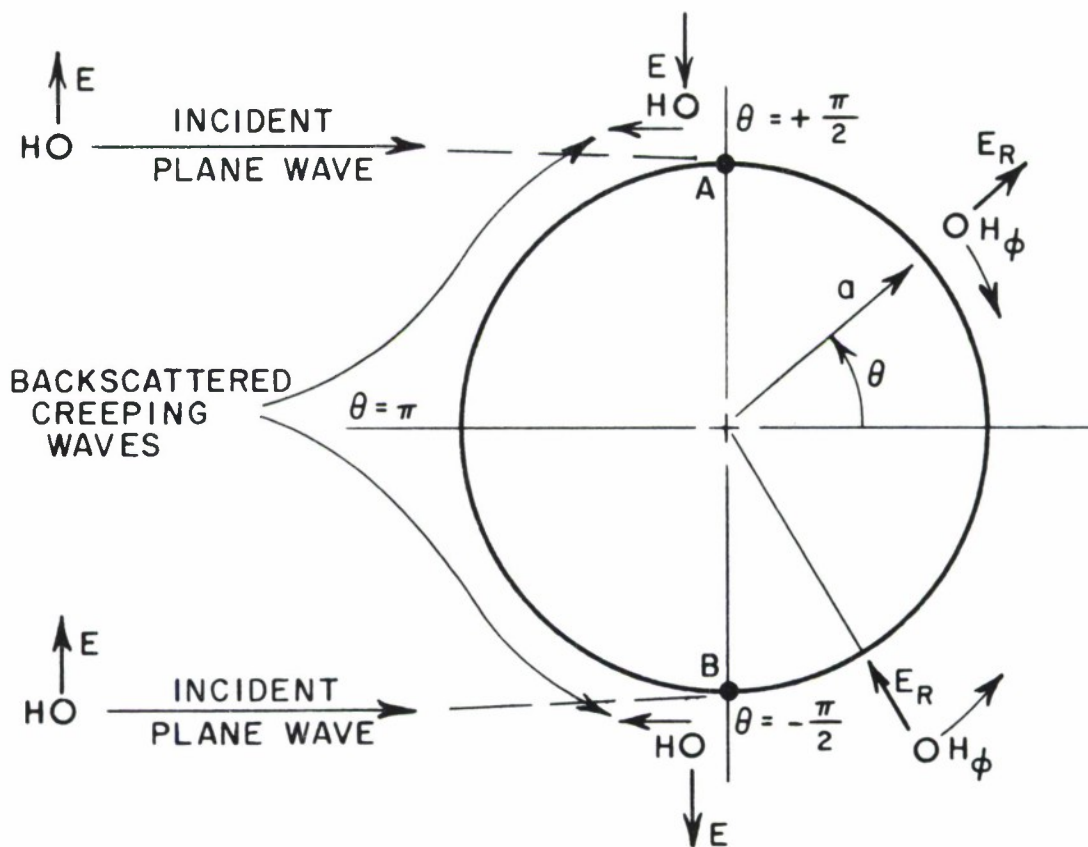


Fig. 18--Creeping waves on the sphere.

Voltmer[ 37] incorporate higher-order correction terms. A comparison of the results of Keller and Levy[ 31, 32] and Voltmer[ 37] is given in Table I which has been prepared by Voltmer[ 37] .

An approach to the general formulation of the creeping wave paths on bodies of revolution has been developed by Kinber[ 33] . Kinber has shown that the wave equation may be expanded in a set of "ray coordinates" in which the solution can be written in a form whose magnitude is dependent upon the cross section of the ray tube

TABLE I  
 DIFFRACTION AND ATTENUATION COEFFICIENTS  
 FOR THE CYLINDER AND SPHERE

BODY TYPE	SQUARE OF DIFFRACTION COEFFICIENT $D_{\nu m}^2 = (\text{Column A}) * (\text{Column B})$	ATTENUATION CONSTANT $\alpha_m = \frac{[q_m]}{a} e^{-j\frac{\pi}{6} \left(\frac{Ka}{2}\right)^{1/6}} + \text{corr.}$	BOUNDARY CONDITION AND ZEROS
	A. Keller's result	Correction terms	
Soft cylinder	B. Correction coefficient $1 + \frac{1}{30} q_m e^{-j\frac{\pi}{3} \left(\frac{Ka}{2}\right)^{-2/3}}$ + ...		$A_1(-q_m) = 0$ $[q_m] = q_m$
Soft sphere	$\frac{\pi^{-1/2} 2^{-5/6} a^{1/6} e^{-j\frac{\pi}{2}}}{K^{1/6} [A_1(-q_m)]^2}$ $1 + \left(\frac{1}{30} + \frac{1}{4}\right) q_m e^{-j\frac{\pi}{3} \left(\frac{Ka}{2}\right)^{-2/3}}$ + ...	$\frac{1}{60} \frac{q_m^2}{a} e^{-j\frac{\pi}{6} \left(\frac{Ka}{2}\right)^{-1/6}} + \dots$	$q_0 = 2.33811$ $q_1 = 4.08795$
"Soft" EM sphere			
Hard cylinder	$1 + \left(\frac{1}{30} - \frac{1}{10q_m^3}\right) \bar{q}_m e^{-j\frac{\pi}{3} \left(\frac{Ka}{2}\right)^{-2/3}}$ + ...	$\left(\frac{1}{60} + \frac{1}{10\bar{q}_m^3}\right) \frac{\bar{q}_m^2}{a} e^{-j\frac{\pi}{6} \left(\frac{Ka}{2}\right)^{-1/6}}$ + ...	$A_1(-\bar{q}_m) = 0$ $[q_m] = \bar{q}_m$
Hard sphere	$\frac{\pi^{-1/2} 2^{-5/6} a^{1/6} e^{-j\frac{\pi}{2}}}{K^{1/6} \bar{q}_m [A_1(-\bar{q}_m)]^2}$ $1 + \left(\frac{1}{30} + \frac{1}{4} - \frac{7}{20\bar{q}_m^3}\right) \bar{q}_m e^{-j\frac{\pi}{3} \left(\frac{Ka}{2}\right)^{-2/3}}$ $\cdot \left(\frac{Ka}{2}\right)^{-2/3} + \dots$	$\frac{1}{a} \left[ \frac{\bar{q}_m}{1400} + \frac{9}{200} + \frac{49}{800\bar{q}_m} \right] \left(\frac{Ka}{2}\right)^{-1}$ $\left(\frac{1}{60} - \frac{3}{20\bar{q}_m^3}\right) \frac{\bar{q}_m^2}{a} e^{-j\frac{\pi}{6} \left(\frac{Ka}{2}\right)^{-1/6}}$ + ...	$\bar{q}_0 = 1.01879$ $\bar{q}_1 = 3.24820$
"Hard" EM sphere			



Here it is seen that the ray path does not intersect the back point but is instead tangent to a cone whose cone angle can be written as

$$(73) \quad \beta_o = \sin^{-1} (m/ka)$$

for a source field having an  $e^{im\phi}$  azimuth dependence. The cone angle is dependent upon the mode order ( $m$ ). The analysis of Kinber for an arbitrary incident field requires a summation of modes. As the ray coordinates used for each mode differ the task of constructing the surface field at a given point on the sphere is formidable. For the case of plane wave incidence of the form

$$(74) \quad \begin{pmatrix} H_\phi \\ E_\phi \end{pmatrix} = - \begin{pmatrix} \cos \phi' \\ \sin \phi' \end{pmatrix} K^2 p \frac{e^{ik(\xi' - \eta')}}{(\xi' - \eta')}$$

the analysis for the scattered field is simplified resulting in a solution for the scattered field of the form

$$(75) \quad \begin{pmatrix} H_\zeta \\ E_\zeta \end{pmatrix} = \begin{pmatrix} p \\ m \end{pmatrix} e^{i\phi'} \frac{C_o \sqrt{a} \cos \delta}{2\sqrt{\pi M h (\xi - \eta)}} e^{i \left[ k(\xi + \xi') - \frac{2}{3} Y^{3/2} - \frac{\pi}{4} \right]} \cdot V_1 \left[ Z, Y', \begin{pmatrix} 0 \\ \infty \end{pmatrix} \right]$$

where  $p, m$  are electric or magnetic dipole moments respectively

$h$  is the distance to the observation point

$Y = kh/M, Y' = kh'/M$

$$\begin{aligned}
M &= (ka/2)^{1/3} \\
V_1 &= i \sqrt{2\pi} \sum_n \frac{e^{it_n z}}{t_n - g^2} \frac{W_1(t_n - Y')}{W_1^2(t_s)} \\
C_0 &= k^2 e^{i\frac{\pi}{4}} \sqrt{2\pi \sin \delta} / \sqrt{M} \\
W_1(t - Y) &= i\sqrt{\pi M} H_\nu^{(1)}(kr)
\end{aligned}$$

This solution is similar to that of Kouyoumjian[ 29] and Hong[ 30] , the primary difference being in the ray path geometry used. A complete discussion of this solution is given by Kinber[ 34] .

To date the above solutions have not been applied to the task of determining the surface fields on the sphere. Kazirinoff and Senior[ 36] have attempted to apply creeping wave theory to calculate the major and minor axis surface fields. While the agreement in the major axis is good, the minor axis fields have not been satisfactorially calculated.

The empirical approach adopted by Moreland, Peters, and Kilcoyne[ 35] utilizes the known E-plane field to determine appropriate attenuation and diffraction coefficients. This approach is of interest in that it lends itself to extension to more general targets. It proceeds by assuming that the surface field shown in Fig. 18 in the shadow region of the sphere can be represented as the sum of two creeping waves as

$$(76) \quad H_{\phi} = H_0 \left[ e^{-(jk_0 + \alpha_s) a(\pi/2 - \theta)} + e^{-(jk_0 + \alpha_s) a(\pi/2 + \theta)} \right] ;$$

and the radial electric field may be written as

$$(77) \quad E_r = E_0 \left[ e^{-(jk_0 + \alpha_s) a(\pi/2 - \theta)} - e^{-(jk_0 + \alpha_s) a(\pi/2 + \theta)} \right] .$$

Now  $H_0$  and  $E_0$  are chosen to match the exact solution as closely as possible for some value of  $k_0 a$ . A value of  $k_0 a = 10$  was chosen.

Then, assuming  $\alpha_s$  to be modified by a constant from the value of that given by Keller and Levy[ 32] for the cylinder, one obtains

$$(78) \quad \alpha_s = 0.84 a^{-\frac{2}{3}} \lambda^{-\frac{1}{3}} e^{j\frac{\pi}{6}}$$

in order to fit the curves of Fig. 20.

It is seen that fields of the form given in Eqs. (76) and (77) are a reasonable approximation to the exact fields. The back-scattered fields due to the creeping wave may be written as

$$(79) \quad E_{cw}^s = 2E_i D_s^2 e^{-j2k_0 a} e^{-(jk_0 + \alpha_s) \pi a} \frac{e^{-jk_0 R}}{R} ,$$

where  $R$  is the observation distance from the center of the sphere.

The magnitude and phase of the creeping wave obtained using Eq.

(79) can be compared to the magnitude and phase of the exact

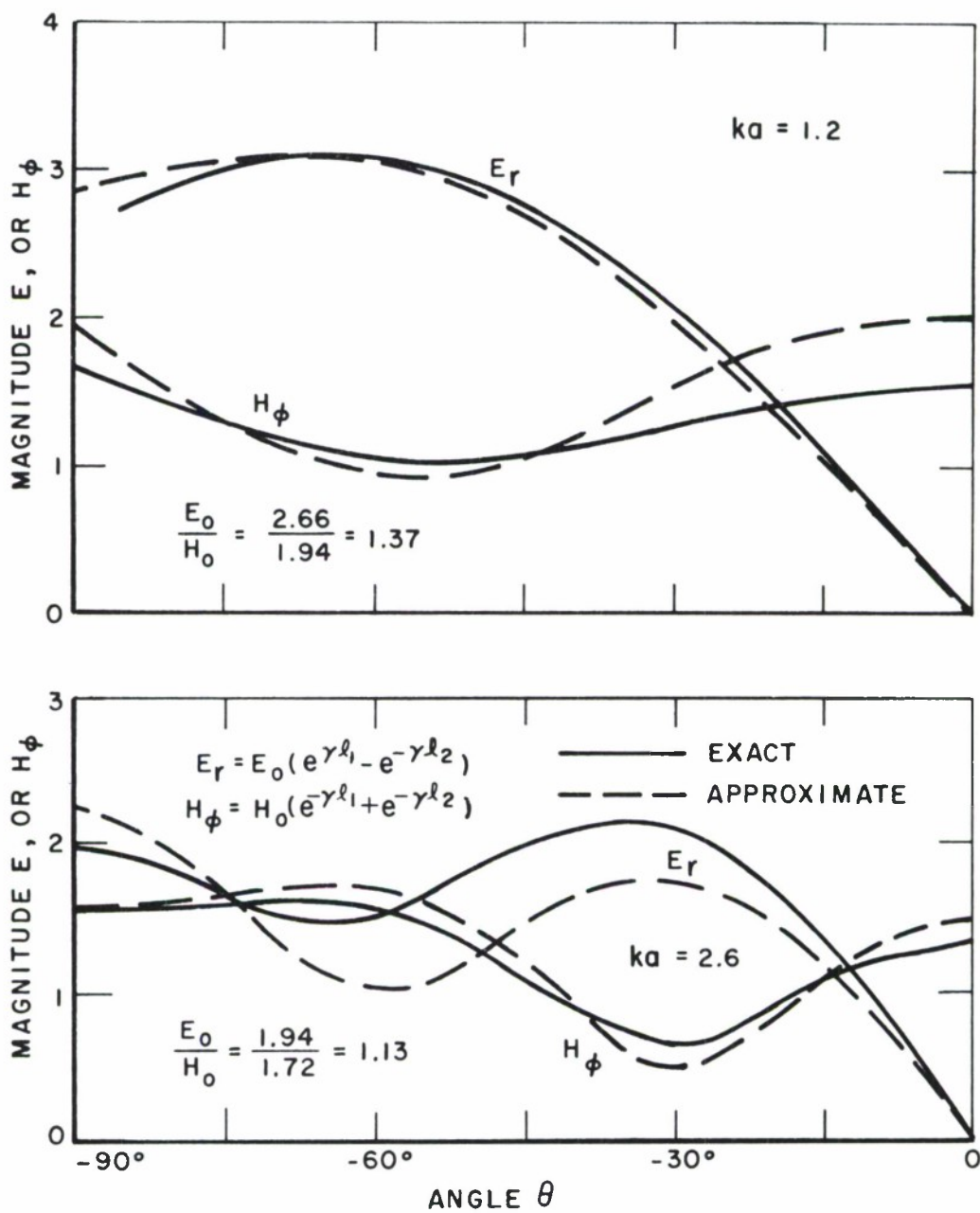


Fig. 20--Normalized fields on the surface of a conducting sphere.



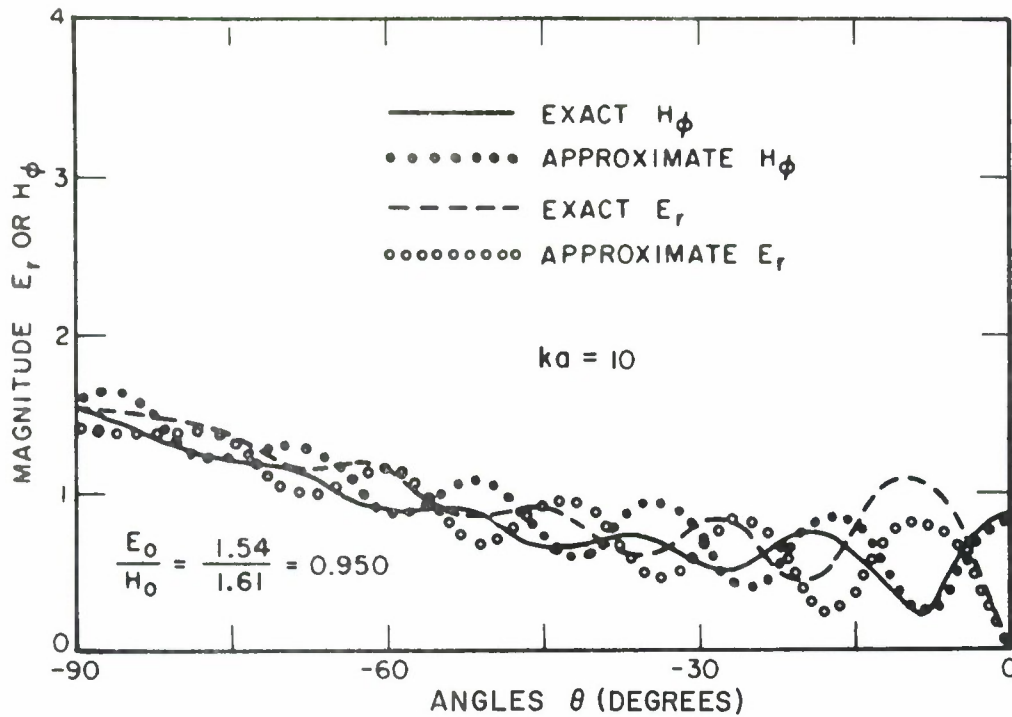


Fig. 20--continued.

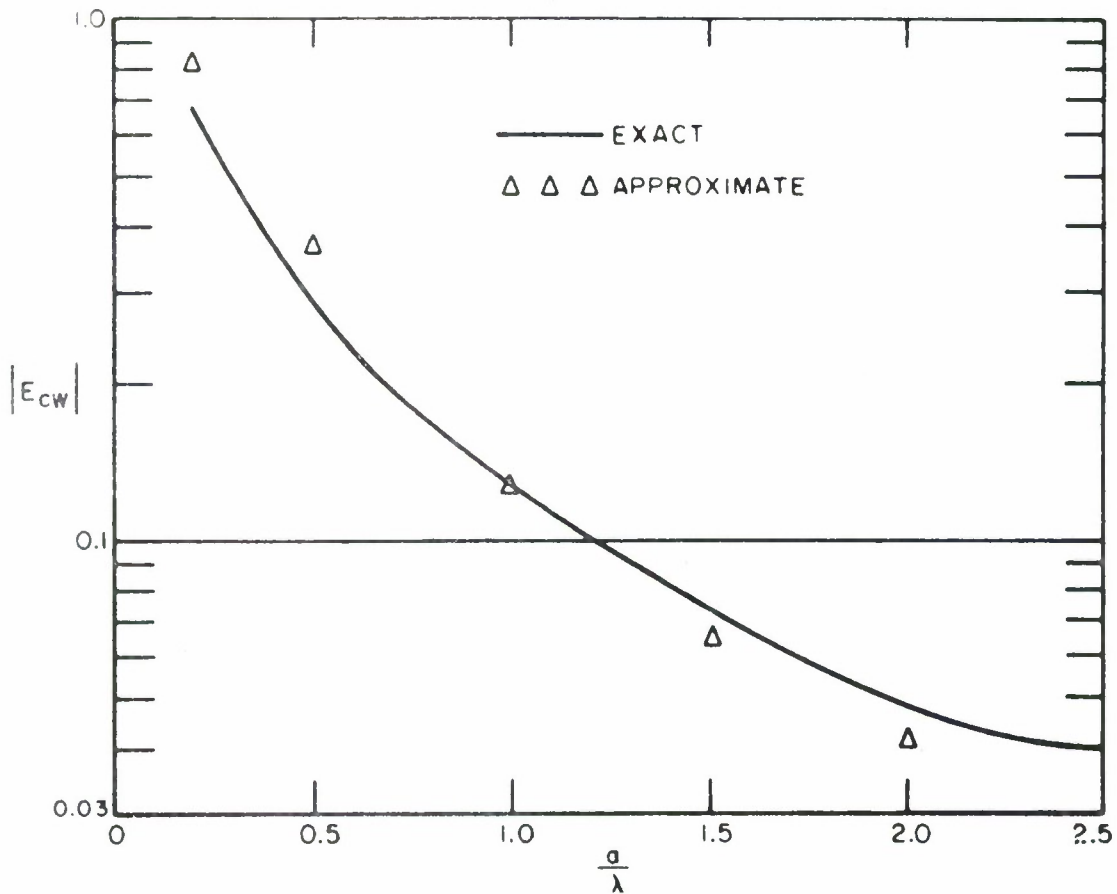


Fig. 21--Absolute relative magnitude of backscattered fields due to creeping waves.

creeping-wave fields obtained by subtracting the specular point contribution of the physical optics term from the exact scattered fields; i. e. ,

$$(80) \quad E_{cw}^{\text{exact}} = E^{\text{exact}}(k_0 a) + \left(1 - \frac{1}{j2k_0 a}\right) \frac{a}{2}$$

where the factor  $e^{-jk_0 R}/R$  has been suppressed. The value of  $D_s^2$  is adjusted by a constant to agree with the exact backscattered fields for a radius of  $1.0\lambda$ . The form of  $D_s^2$  is also modified by a factor of  $\lambda^{\frac{1}{2}}$  in order that Eq. (79) be dimensionally correct, resulting in

$$(81) \quad D_s^2 = 0.27 \rho^{\frac{1}{3}} \lambda^{\frac{2}{3}} e^{-j\pi/12} .$$

The magnitudes of the exact and approximate creeping-wave components as a function of radius are compared in Fig. 21 and their phases are compared in Fig. 22. The agreement is good for a wide range of  $k_0 a$  values.

Moreland, Peters, and Kilcoyne[ 35] have also applied this form of solution to the problem of bistatic scattering in the E-plane with excellent results.

The analysis of Moreland et. al. [ 35] is a simplified creeping wave analysis. It uses a single non-convergent (and non-divergent) ray path together with approximate diffraction and attenuation coefficients to construct an approximate solution for the scattered field

due to creeping waves propagating in each direction along the ray path. The path chosen is the path traversed by the "major" ray (i. e. the path corresponding to the E-plane of the sphere). This analysis suggests that an approximate picture of scattering by a sphere can be constructed by neglecting the creeping waves which have a radial magnetic field (i. e. the "minor" creeping waves) and by considering only the creeping waves which have a radial electric field (i. e. the "major" creeping waves).

The analyses outlined above do not allow the determination of the fields in the minor axis because of the ray geometry which has been assumed. The analysis of Kinber [34] may allow such a calculation but this has not yet been performed.

A new approach to the determination of the ray paths and the surface fields on the sphere is considered here. It will be assumed that all the modes may be lumped into a single traveling wave or that only a single mode is dominant. In order to determine the path followed by such a creeping wave the results of the exact Mie series solution are used to compute the real part of the Poynting vector at the shadow boundary, i. e. ,

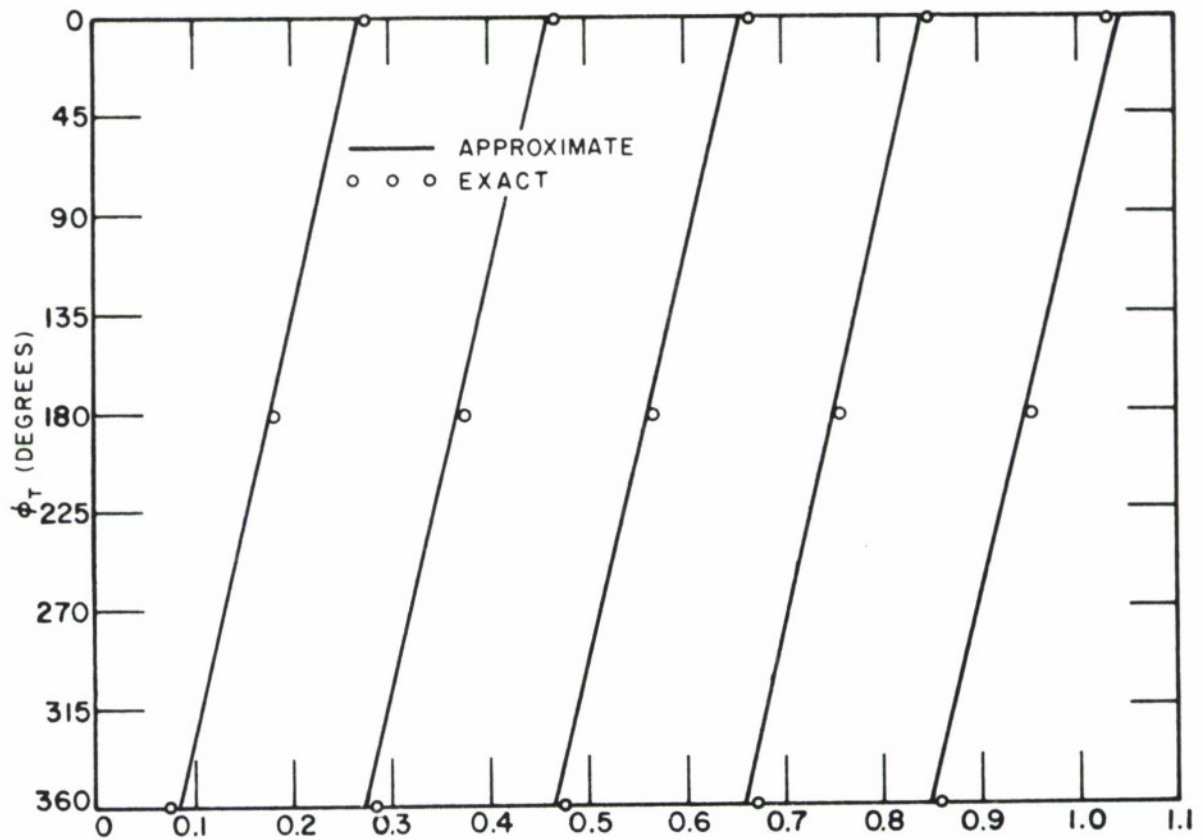


Fig. 22--Phase of backscattered fields due to creeping waves.

$$(82) \quad \bar{S} = \hat{\theta}(-E_r H_\phi^*) \Big|_{\theta=\pi/2} + \hat{\phi}(E_r H_\theta^*) \Big|_{\theta=\pi/2} \cdot$$

It is assumed that a creeping wave originating at a point on the shadow boundary  $(\pi/2, \phi)$  propagates in the direction of  $\text{Real}(\bar{S})$  at that point and thereafter follows a great circle route around the sphere.

The result of such an assumption is shown in Fig. 23 where it is seen that the ray paths do not intersect the back point of the sphere,

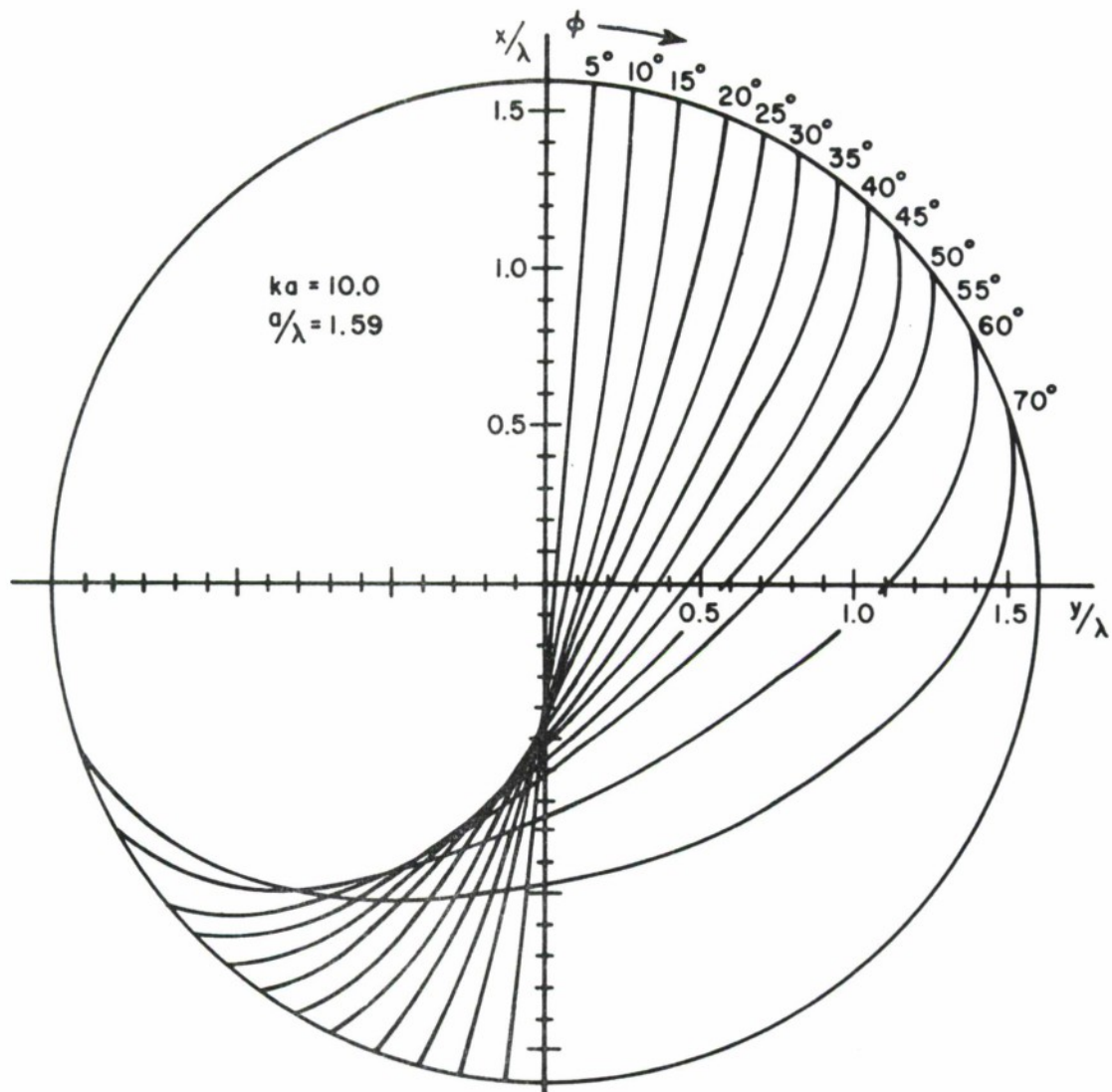


Fig. 23--Ray paths on the sphere determined using the Poynting Vector.

and indeed miss the back point by varying amounts. In addition to the ray paths the creeping wave fields have been calculated along the ray path in the form

$$(83) \quad H_{CW} = (H_0 \cos \phi)_{\pi/2}^{\phi} \cdot e^{-(jk_0 + \alpha_s)\ell} \cdot F(\ell)$$

where the factor  $\cos \phi$  accounts for the tangential component of the incident magnetic field at the shadow boundary and where the exact  $\alpha_s$  is used and  $\ell$  is measured along the great circle specified by the Poynting vector. The calculations were performed using a computer program. For the case of the  $ka = 10$  sphere the intersections of the ray paths in the  $\phi = 0^\circ, 90^\circ$  planes have been plotted in Figs. 24 and 25. In addition the angles at which the ray paths cross the axes are plotted in Figs. 26 and 27. As seen from Fig. 23 the H-plane magnetic field can be written as

$$(84) \quad H_\theta = H_0 \cos \phi F(\ell) e^{-(jk_0 + \alpha_s)\ell} \sin \delta$$

where  $\delta$  is the angle between the ray and the H-plane and where the attenuation constant  $\alpha_s$  is the attenuation constant for the "hard" sphere given in Table I. Using the intersection and angle data from Figs. 25 and 27 it is possible to determine  $F(\ell)$ ,  $\ell$ , and  $\delta$  for each ray which intersects the minor axis, and thus compute the magnetic field in the H-plane. The results of such a calculation

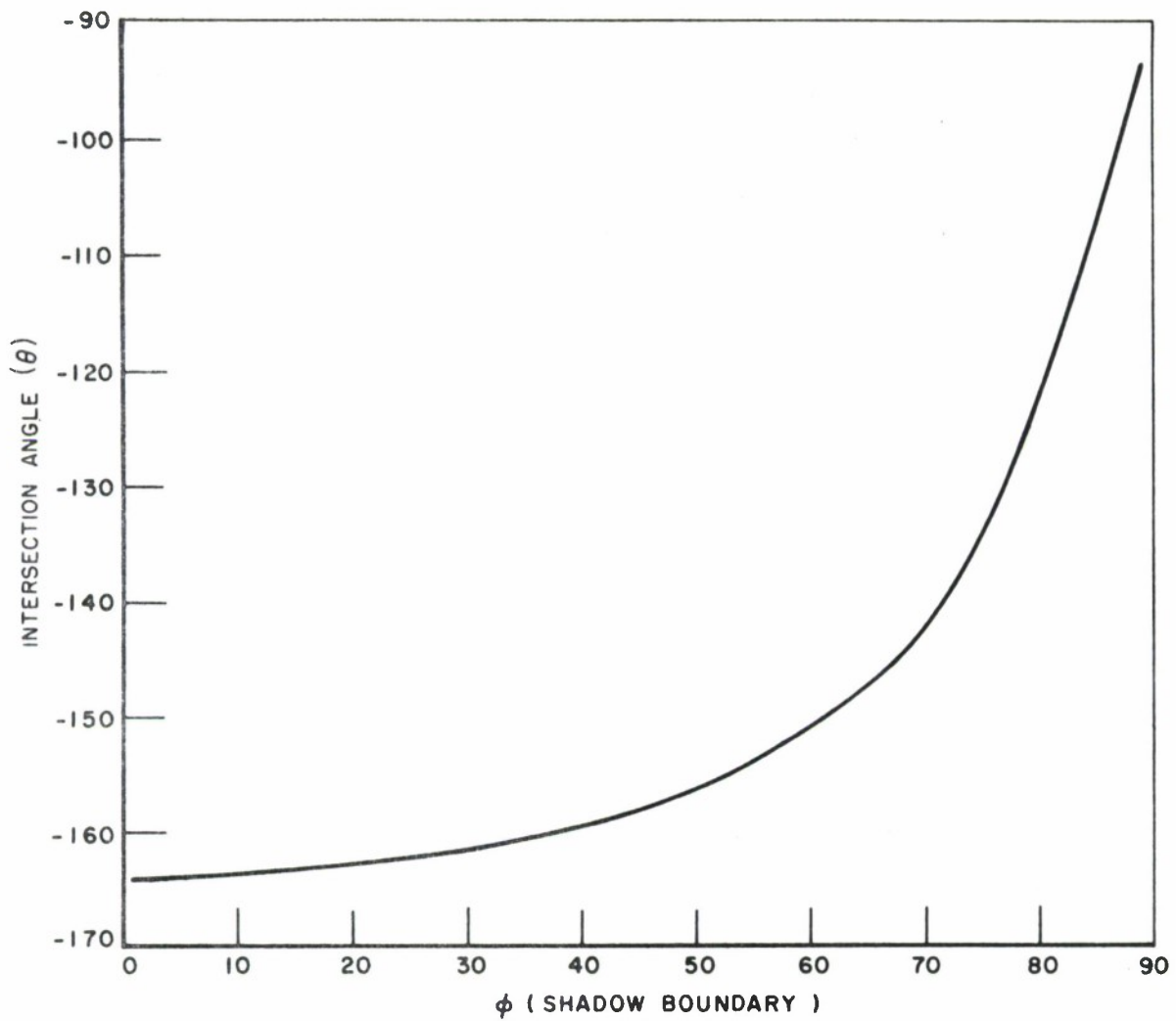


Fig. 24--Intersection of the ray paths and the  $\phi = 0^\circ$  plane (i. e., the E-Plane).

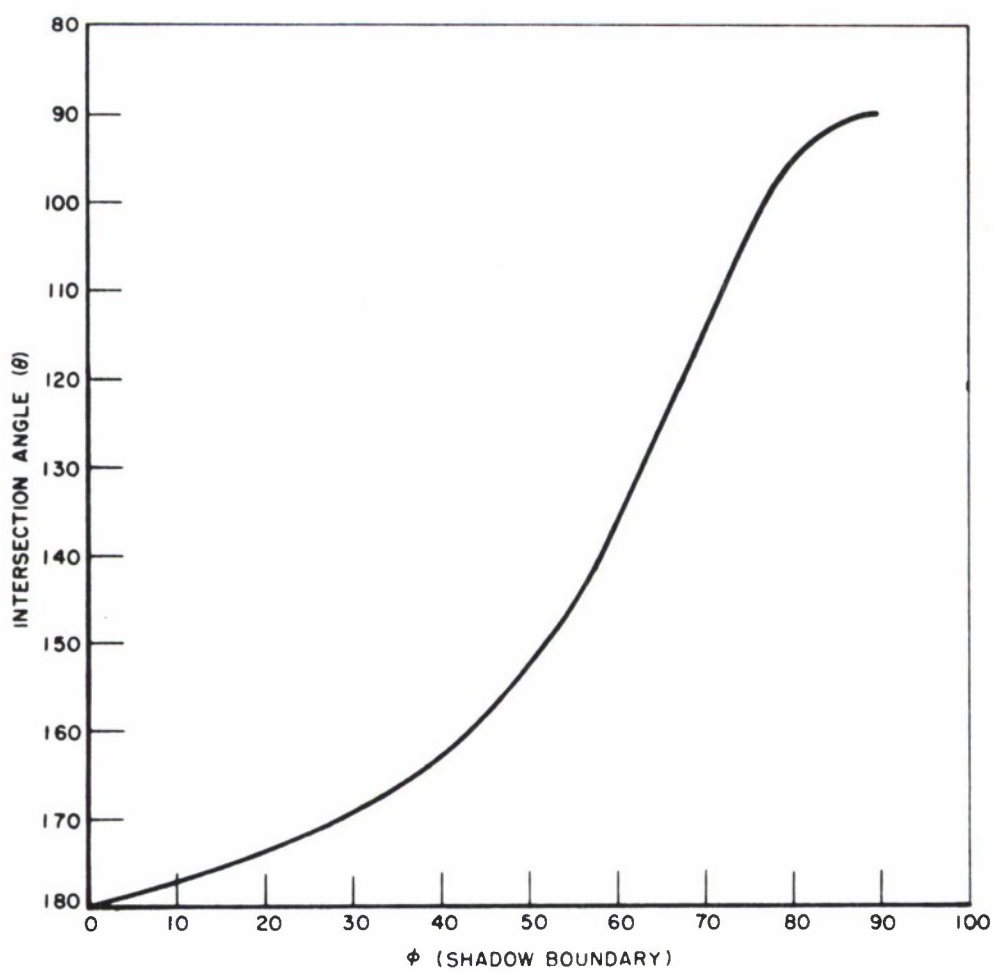


Fig. 25--Intersection of the ray paths and the  $\phi = 90^\circ$  plane (i. e., the H-plane).



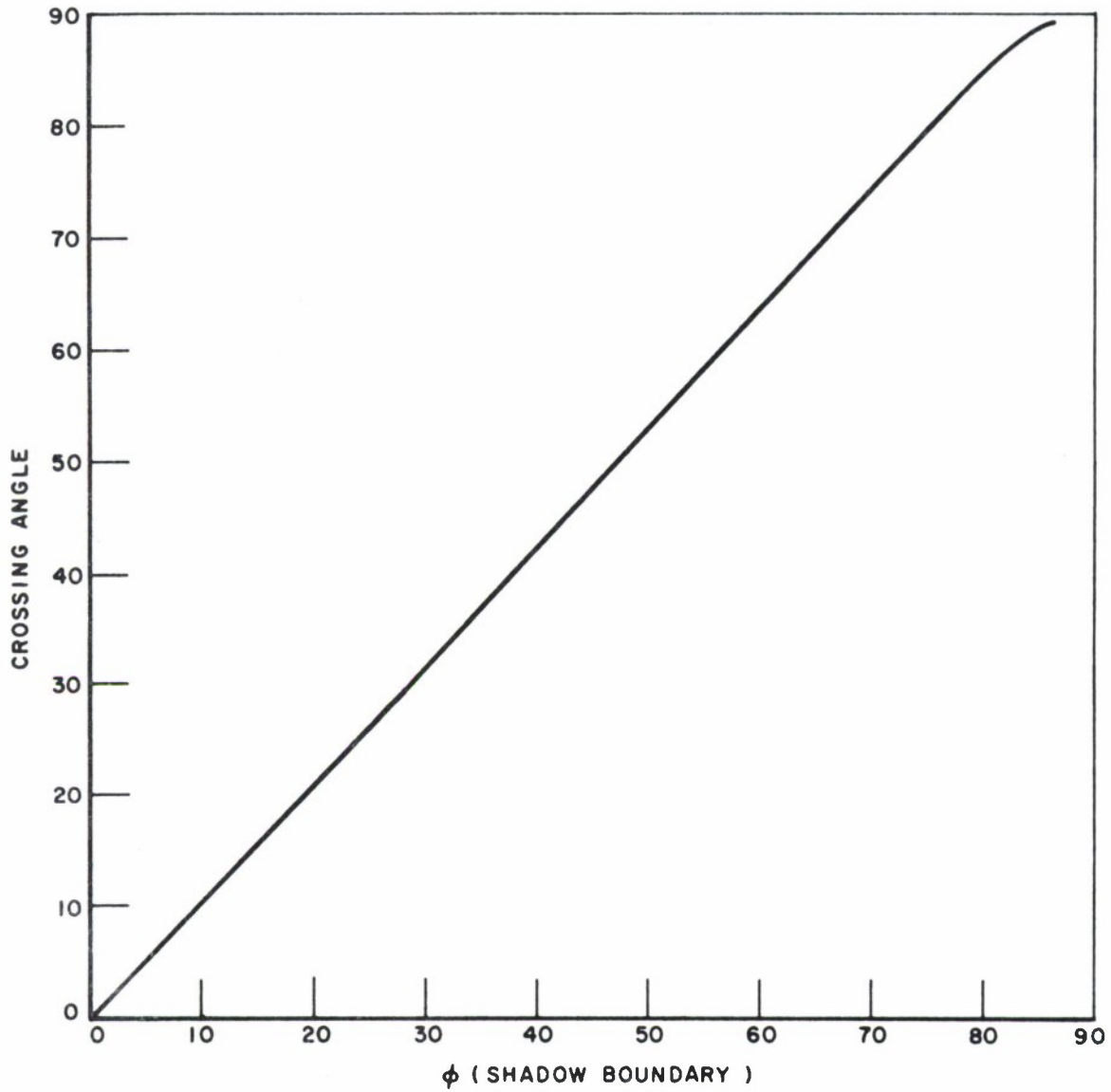


Fig. 26--Angle between the ray path and the  $\phi = 0^\circ$  plane.

boundary, the contribution of the "minor" creeping wave (i. e., the rays corresponding to the "soft" sphere) may be important, even though the attenuation of this wave is large, as can be seen from Table L. Using the attenuation and diffraction coefficients of Table I, and assuming no convergence or divergence of the minor creeping wave about the  $\phi = 90^\circ$  plane the minor creeping wave may be calculated. The results of this calculation are also shown in Fig. 28. Close to the shadow boundary the minor creeping wave field is seen to be a reasonable approximation to the exact field. Thus both the major and minor creeping wave contributions are needed to predict the minor axis field. A more accurate solution for the effect of the major creeping wave near the shadow boundary is needed in order to demonstrate the continuity of these solutions in the  $\phi = 90^\circ$  plane.

In the calculation of the major axis field ( $\phi = 0^\circ$  plane) it suffices to know the intersection of the closest ray, as indicated in Fig. 24. This is because the rays removed from the major axis have little effect on the field in the major axis due to polarization, flux tube width, and crossing angle effects. The calculated major axis field is shown in Fig. 29. It is seen to be in good agreement with the exact solution. The calculated field is normalized to the exact field at  $\theta = \frac{\pi}{2}$ ,  $\phi = 0$ . A disadvantage of the Poynting

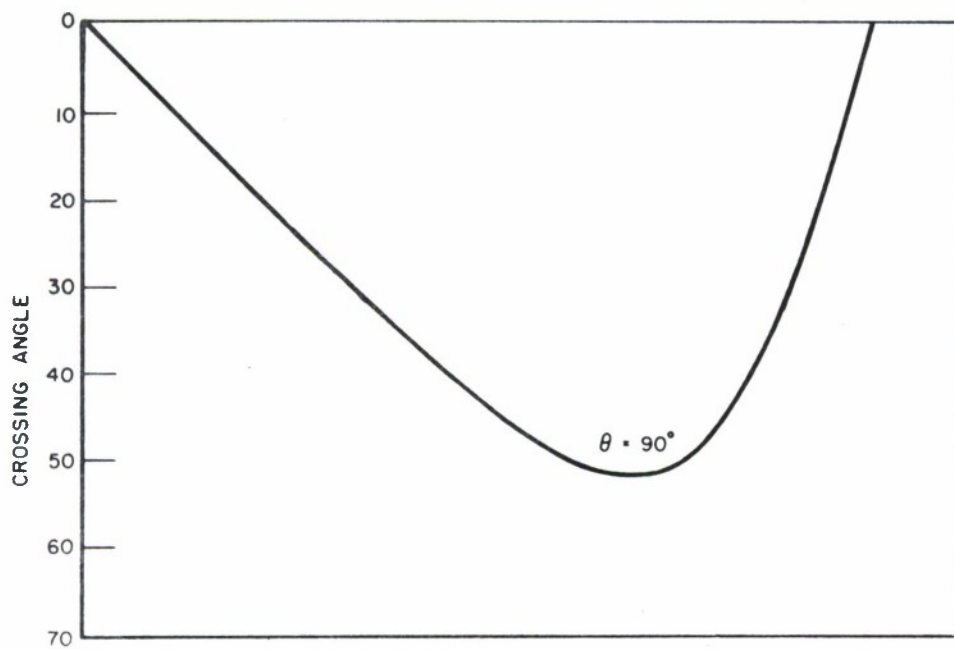


Fig. 27--Angle between the ray path and the  $\phi = 90^\circ$  plane.

for a  $ka = 10$  sphere are presented in Fig. 28, where the field is normalized to the exact field at  $\theta = \frac{\pi}{2}$ ,  $\phi = 0$ . It is seen that close to the back point the calculated field is in good agreement with the exact solution. The agreement deteriorates as one approaches the shadow boundary. This is expected as the attenuation coefficient for the "hard" sphere derived by Voltmer[ 37] is most accurate for the deep shadow region. The region close to the shadow boundary has been examined by Foch[ 38]. Also, close to the shadow

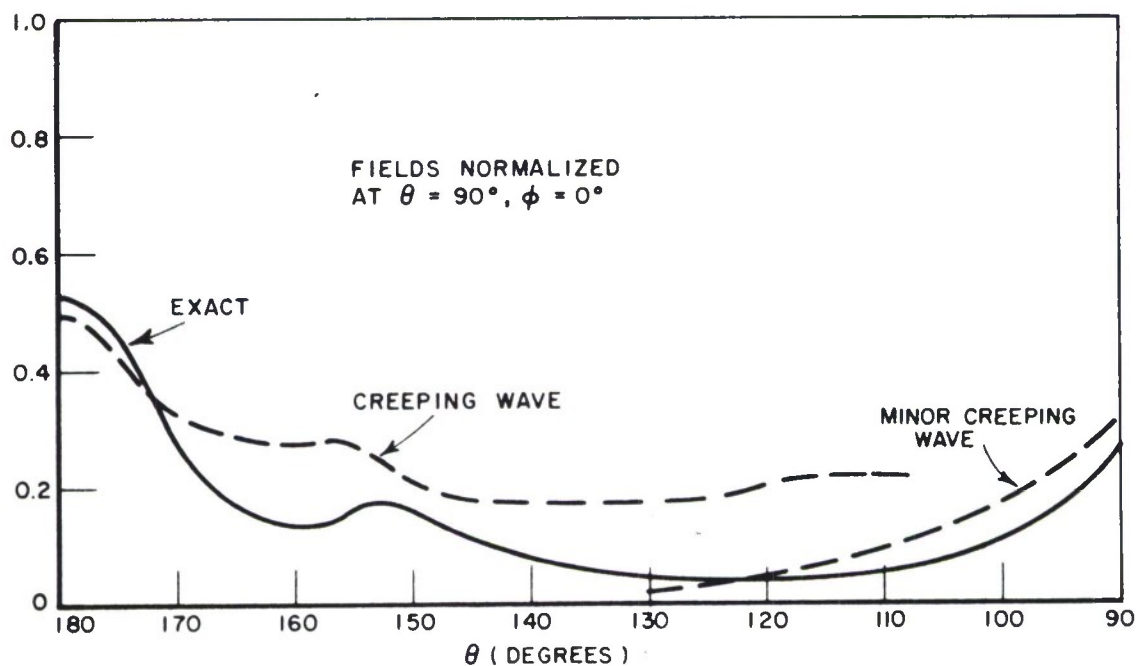


Fig. 28--H-plane surface fields on the sphere.

boundary, the contribution of the "minor" creeping wave (i. e., the rays corresponding to the "soft" sphere) may be important, even though the attenuation of this wave is large, as can be seen from Table I. Using the attenuation and diffraction coefficients of Table I, and assuming no convergence or divergence of the minor creeping wave about the  $\phi = 90^\circ$  plane the field of the minor creeping wave may be calculated. The results of this calculation are also shown in Fig. 28. Close to the shadow boundary the minor creeping wave field is seen to be a reasonable approximation to the exact field. Thus both the major and minor creeping wave contributions are needed to predict the H-plane field. A more accurate solution for the effect of the major creeping wave near the shadow boundary is needed in order to demonstrate the continuity of these solutions in the  $\phi = 90^\circ$  plane.

In the calculation of the major axis field ( $\phi = 0^\circ$  plane) it suffices to know the intersection of the closest ray, as indicated in Fig. 24. This is because the rays removed from the major axis have little effect on the field in the major axis due to polarization, flux tube width, and crossing angle effects. The calculated E-plane field is shown in Fig. 29. It is seen to be in good agreement with the exact solution. The calculated field normalized to the exact field at  $\theta = \frac{\pi}{2}$ ,  $\phi = 0$ . A disadvantage of the Poynting

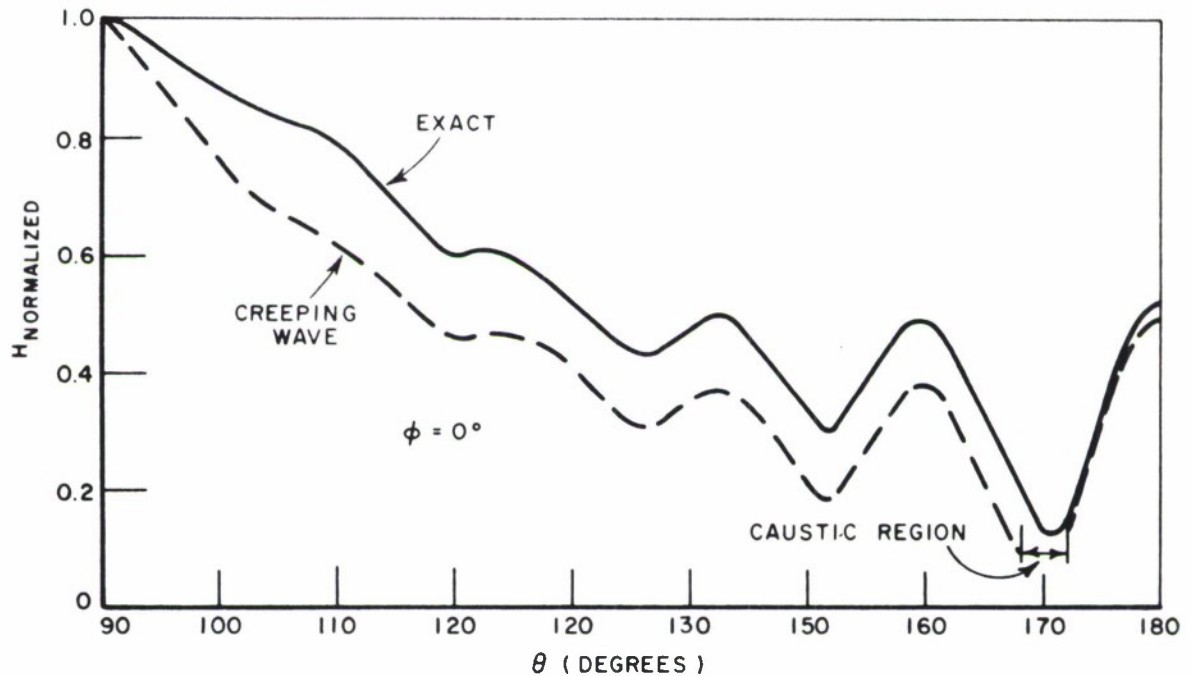


Fig. 29--E-plane surface fields on the sphere.

vector approach to determining the ray paths is that the exact solution at the shadow boundary must be known. Thus it is not possible to extend this technique to targets for which the exact solution is not available. Also the ray paths must be recalculated for each sphere radius of interest. These calculations have been performed for values of  $k_0 a = 4.0$  and  $10.0$ . Over this range of  $k_0 a$  values the

ray paths do not differ substantially, as may be seen from Table II where some major and minor axis intersections are compared.

It is noted that the attenuation coefficient developed by Moreland, et al. [ 35] for the sphere does not yield the correct major axis fields when the effect of the convergence of the flux tube to form a caustic is considered. This is reasonable as the solution of Moreland, et al. [ 35] includes the effects of the caustic and integration of the shadow boundary contributions in the determination of the empirical attenuation and diffraction coefficients. However good results are obtained for the backscattered fields using their solution. The fact that their approximate solution gives reasonable results is not surprising if one considers the ray path picture of Kinber[ 34] and that of the Poynting vector method. It is seen that in the E-plane the major axis creeping wave is the dominant contributor, and the rays which skew about the back point are negligible as regards backscatter since there are no tangent lines from the skewed creeping wave paths in the direction of the source. These creeping waves would contribute to the bistatic radar cross section in planes removed from the E-plane. Thus, because of the ray path geometry, a simple traveling wave picture suffices to describe the E-plane.

TABLE II  
 MAJOR AND MINOR AXIS INTERSECTIONS  
 FOR A SPHERE ( $ka = 4.0, 10.0$ )

$\phi$ shadow boundary	Major Axis Intersection ( $^{\circ}$ )		Minor Axis Intersection ( $^{\circ}$ )	
	$ka = 4.0$	$ka = 10.0$	$ka = 4.0$	$ka = 10.0$
0 $^{\circ}$	—	—	180.00	180.00
10 $^{\circ}$	161.69	163.96	176.60	177.26
20 $^{\circ}$	160.63	163.76	172.73	173.93
30 $^{\circ}$	158.99	162.53	167.47	169.68
40 $^{\circ}$	156.22	159.73	159.64	163.01
50 $^{\circ}$	152.53	156.53	147.95	151.49
60 $^{\circ}$	146.10	151.11	130.56	136.11
70 $^{\circ}$	135.37	141.22	110.14	114.24
80 $^{\circ}$	117.23	122.24	95.07	96.43
90 $^{\circ}$	90.00	90.00	90.00	90.00



The Poynting vector analysis suggests that a "simplified ray path geometry" based upon the component of the electric field normal to the surface may be used for more general targets. In such a geometry only the electric field component normal to the surface (i. e. , the "major creeping wave") is considered. If the family of rays is considered, thus determining the spatial attenuation factor  $F(\ell)$  the exact diffraction and attenuation coefficients of Keller and Levy[ 27, 28] or Voltmer[ 32] are used to compute the creeping wave fields. If only the ray corresponding to the point at which the incident E-vector is normal to the surface is used and a single nondivergent (or nonconvergent) path is used, the approximate diffraction and attenuation coefficients of Moreland, et al. are used.

A simplified ray path geometry, using the approximate forms of the attenuation and diffraction coefficients has the advantage of being easy to apply to the case of parallel polarization backscatter for complicated targets as the geodesic path is simply the profile of the target. In the case of perpendicular polarization the geodesic path is more difficult to determine. A numerical method for finding a geodesic path is presented in Appendix IV. Several examples of a simplified analysis will now be considered for the prolate spheroid, the ogive, and the spherically capped ogive.

### C. The Prolate Spheroid

The prolate spheroid represents a body for which an exact closed form solution is not available except on the axis of rotation. The creeping wave solution for the prolate spheroid proposed here is similar to that of the sphere. That is, it is assumed that the incident plane wave is diffracted at the shadow boundary causing the excitation of creeping waves which propagate around the spheroid and contribute to the scattered field. The scattering due to the illuminated portions of the spheroid will be computed using geometrical optics.

In order to find the ray path geometries for the prolate spheroid for an arbitrary angle of incidence, the geodesic corresponding to the point of attachment and the tangent direction at that point must be calculated. As seen from the sphere analyses of Kinber[ 34] and by the Poynting vector method the determination of the tangent direction of the creeping wave at the shadow boundary is not an easy task in general.

The prolate spheroid has previously been studied by Moffatt[39] using time domain analysis. Moffatt's approach is similar to the creeping-wave approach in that he approximates the impulse response through the use of a "physical optics" contribution in the form of an impulse at time  $t = 0$ , which decays and joins into a creeping wave

return at time  $t = T_0$  (where  $T_0$  corresponds to the time required for the creeping wave to propagate around the spheroid). The form of the impulse response postulated by Moffatt is shown in Fig. 30.

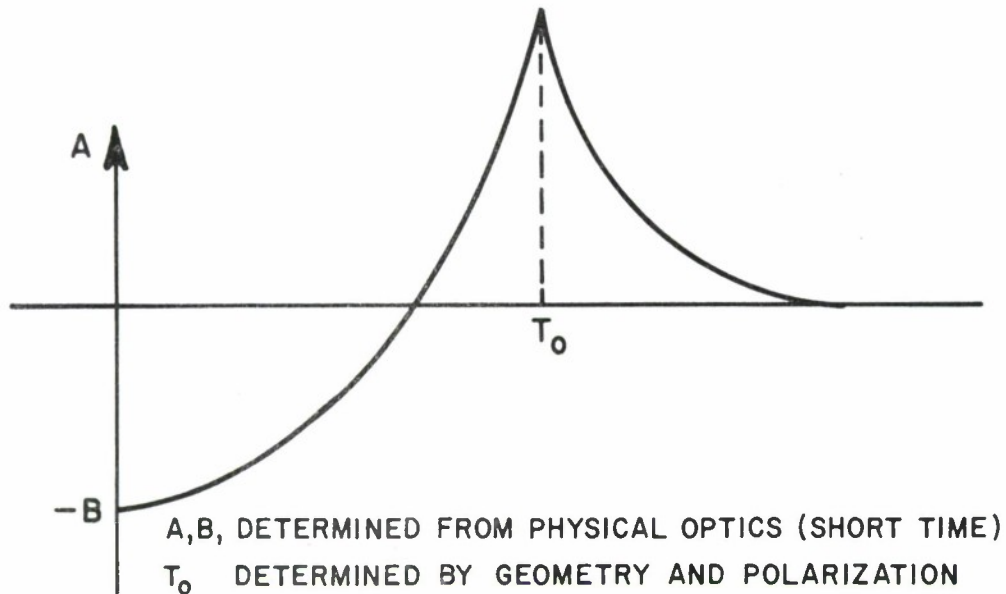


Fig. 30--Impulse response of the prolate spheroid.

Moffatt's determination of the transit time  $T_0$  of the creeping wave was carried out by finding the path length of the ellipse defined by the intersection of the plane defined by the incidence vector and the incident E vector with the prolate spheroid. The initial point of intersection is the point at which the surface normal and the E-vector are collinear. This form of analysis, which resulted in excellent

agreement suggests that the simplified ray path geometry used by Moreland, Peters, and Kilcoyne[ 35] for the sphere can be applied to the prolate spheroid.

Following this line of reasoning we write, for the case of parallel polarization for the prolate spheroid that

$$(85) \quad E_{cw}^s = 2 D_A D_B E^i e^{-\int_A^B (jk_0 + \alpha(\rho)) ds} .$$

In the case of the prolate spheroid the creeping wave paths are elliptical, thus the total attenuation must be expressed as an integral which is dependent upon the radius of curvature along the path. Also the radius of curvature at the points of attachment and reradiation (A, B) must be computed in order to determine the diffraction coefficient.

It was found that the product of the diffraction coefficients at the points of attachment and reradiation could be related to the diffraction coefficient of the sphere with the sphere radius replaced by  $\sqrt{\rho_A \rho_B}$ . The square of the diffraction coefficient is thus

$$(86) \quad D_s^2 = 0.27 (\rho_A \rho_B)^{\frac{1}{6}} \lambda^{\frac{2}{3}} e^{-j\pi/12}$$

where  $\rho_A$  and  $\rho_B$  are the radii of curvature in the propagation direction at points A and B respectively. The specific solution for the prolate spheroid has been presented by Ryan[ 40] and Peters and Ryan[ 41] in previous papers. This case is automatically formulated by the

computer program for the second degree surface of revolution. This program compute the geometrical optics contribution, the points of attachment and reradiation and performs the integration over the path for the case of parallel polarization.

The investigation of the prolate spheroid carried out previously indicated that the magnitude of the attenuation factor required for accurate results in the case of the prolate spheroid differs from that of the sphere. Computations were performed using different magnitudes and the results are shown in Fig. 31. It was concluded that the form of the approximate attenuation coefficient appropriate to the 2:1 prolate spheroid for parallel polarization was

$$(87) \quad \alpha = 0.55 \rho^{-\frac{2}{3}} \lambda^{-\frac{1}{3}} e^{j\frac{\pi}{6}}$$

where  $\rho$  is the radius of curvature in the propagation direction.

Previous work by Peters[42] had been devoted to the determination of the effects of the ratio of the orthogonal radii of curvature on the attenuation and diffraction coefficients. Using the case of the ogive he was able to determine that the diffraction coefficient was the same as given in Eq. (86) but that the attenuation coefficient was modified to

$$(88) \quad \alpha_{og} = 0.20 \rho^{-\frac{2}{3}} \lambda^{-\frac{1}{3}} e^{j\frac{\pi}{6}}$$

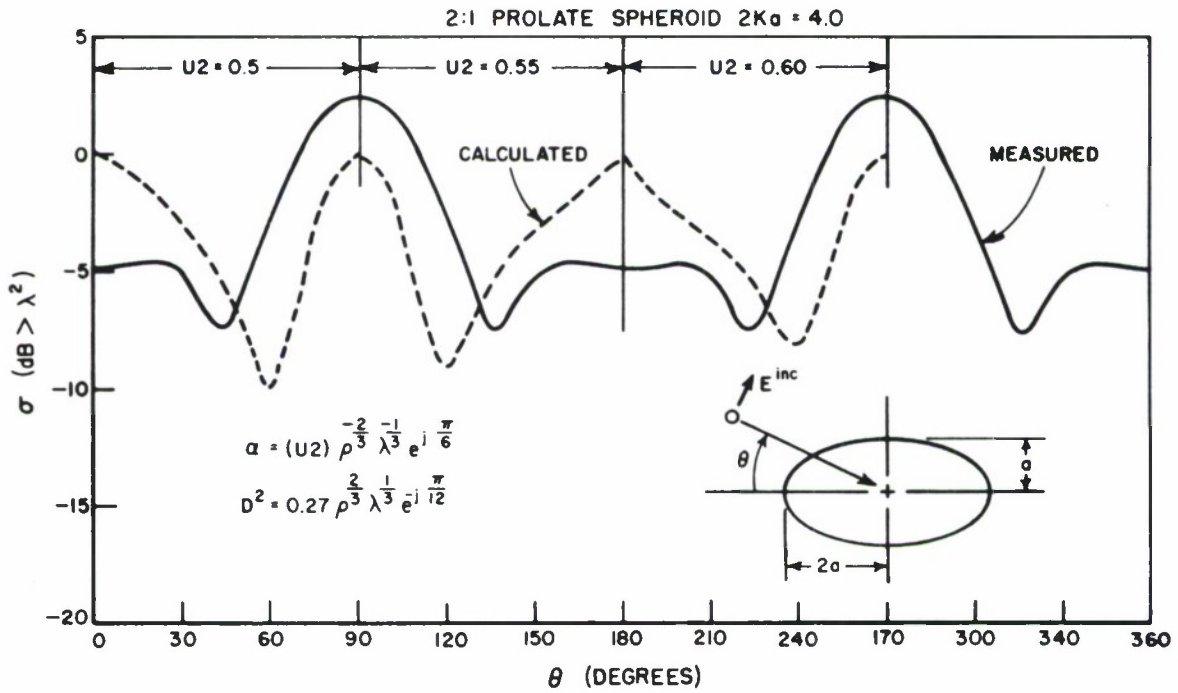


Fig. 31(a)--Backscatter patterns of the prolate spheroid for a range of magnitudes of the attenuation coefficient.

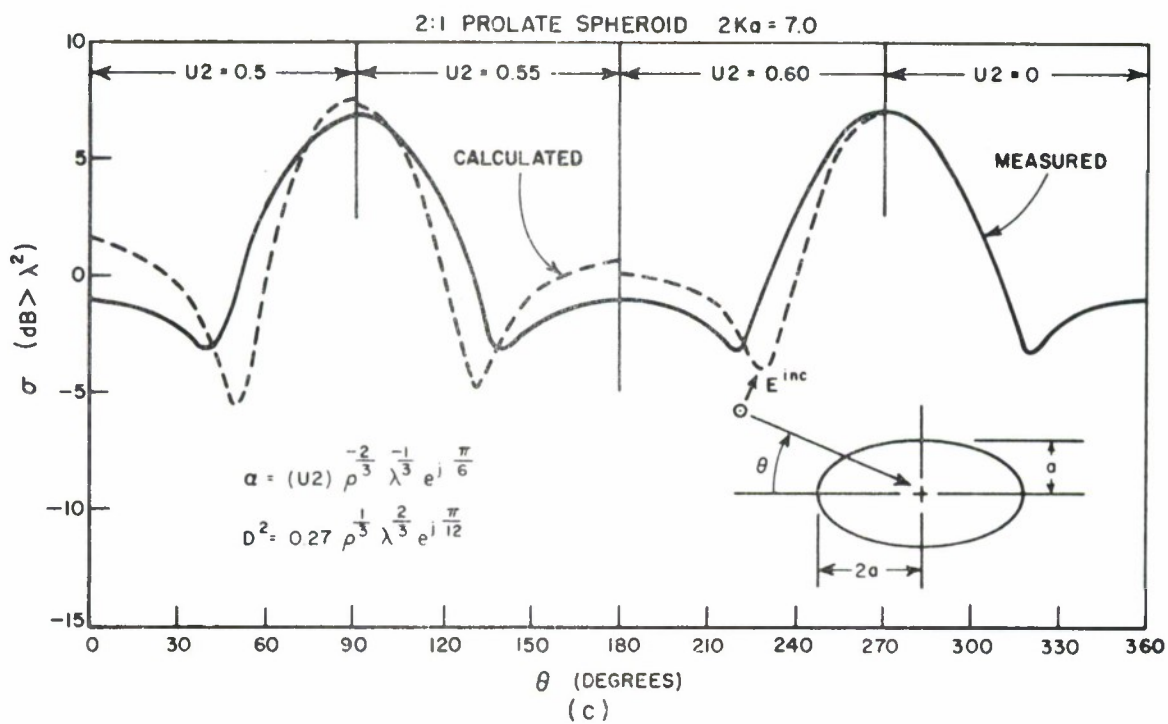
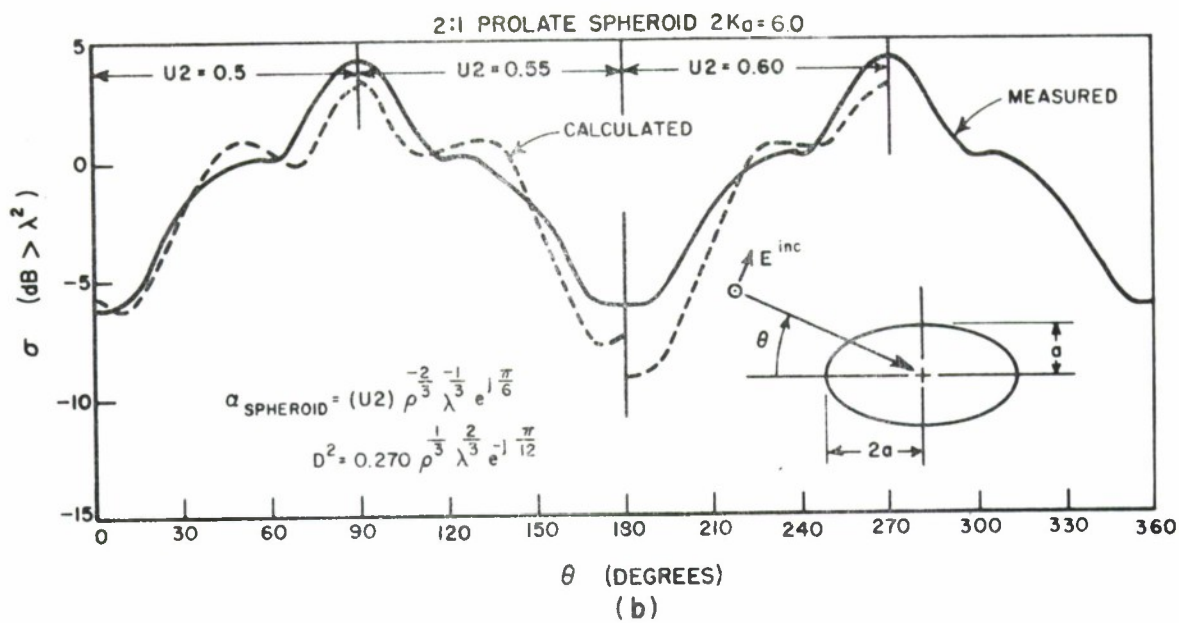


Fig. 31(b, c)--Backscatter patterns of the prolate spheroid for a range of magnitudes of the attenuation coefficient.

It is seen that the attenuation coefficient for the 2:1 prolate spheroid examined lies between the values for the sphere and ogive. Figure 29 illustrates the magnitudes of the approximate attenuation factor for the single path simplified ray geometry as a function of the orthogonal radii of curvature for bodies which have been examined to date. It is seen that the points may be fitted by the smooth curve shown in Fig. 32 of the form

$$(89) \quad \alpha = \left[ 1.48 e^{-0.84(\rho_P/\rho_O)} + 0.20 \right] \rho_P^{-2/3} \lambda^{-1/3} e^{j\frac{\pi}{6}} \quad .$$

where  $\rho_P$  and  $\rho_O$  are the radii of curvature in the propagation and orthogonal directions respectively.

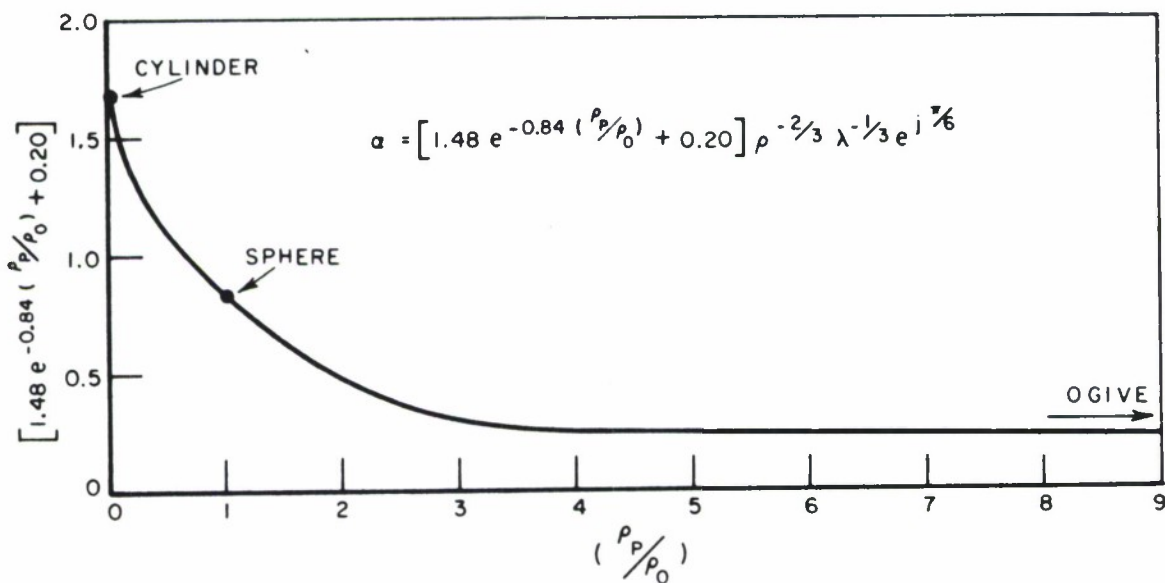


Fig. 32--The variation of the magnitude of the approximate attenuation coefficients as a function of the two orthogonal radii of curvature.



This form has been used to compute the scattered fields of the prolate spheroid for parallel polarization and is in agreement with the best fit obtained in Fig. 31 using Eq. (87). In addition the echo area as a function of wavelength was calculated for parallel and perpendicular polarization for  $\theta = 90^\circ$ . These results are shown in Figs. 33 and 34 and are seen to be in excellent agreement with the experimental data of Moffatt. [39]

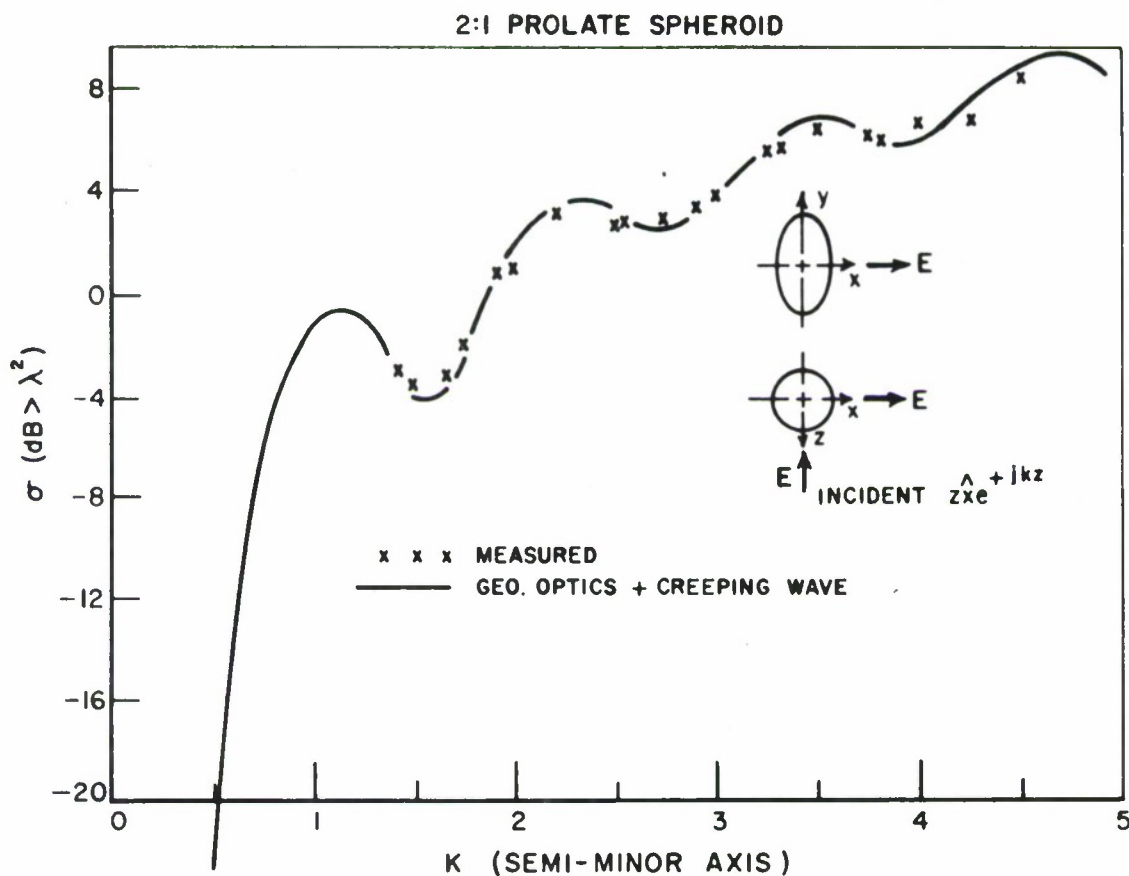


Fig. 33--Echo area of the prolate spheroid as a function of  $k_0 a$  for perpendicular polarization and  $\theta = 90^\circ$ .

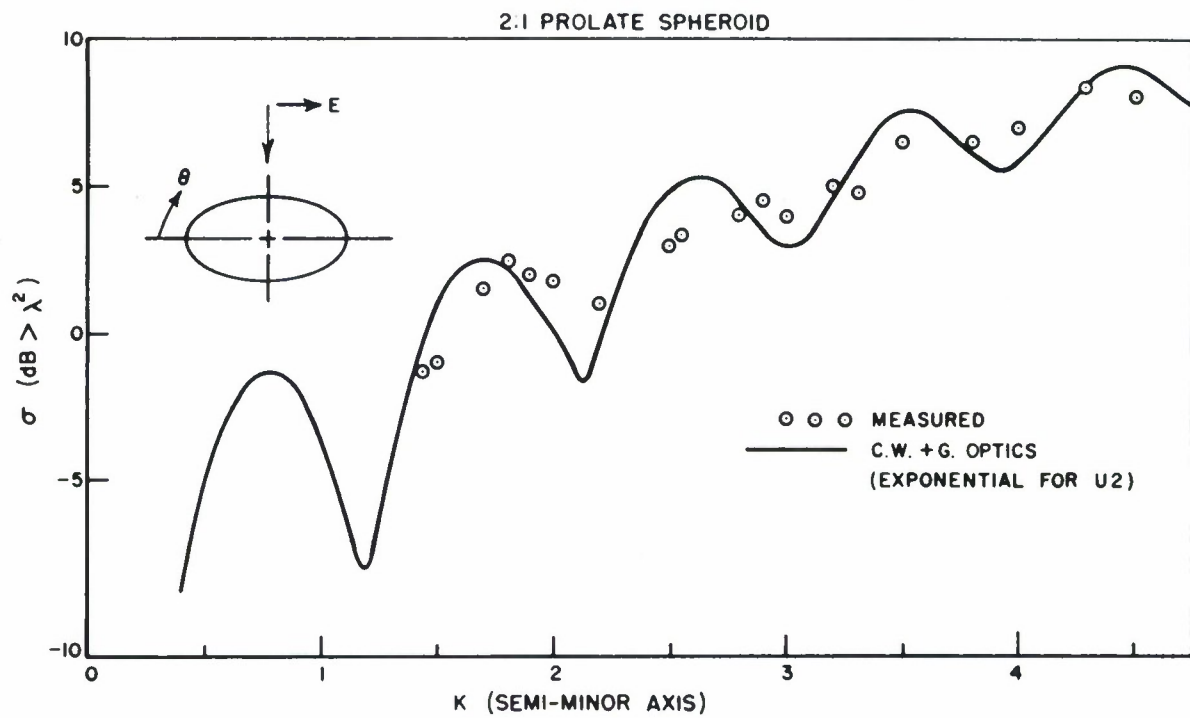


Fig. 34--Echo area of the prolate spheroid as a function of  $k_0 a$  for parallel polarization and  $\theta = 90^\circ$ .

The form of the attenuation coefficient given by Eq. (89) yields good results when used in conjunction with a simplified ray path geometry which utilizes a single ray path defined by the "major" creeping wave. The results of Moffatt[39] indicate that this form of the ray path geometry is also applicable to the case of perpendicular polarization. Due to the difficulties of computing the ray paths for the general body for perpendicular polarization, computations have not yet been made for this case. This will be a future goal in the extension of the creeping wave analysis.

#### D. The Ogive

The ogive has been treated by Peters[43] using a traveling wave antenna approach. In the near-nose-on region this solution has been the only satisfactory solution to date. The form of this traveling wave solution suggests that a creeping wave solution for the ogive can be found providing that the effects of the tip in the shadow region can be determined. Since no diffraction coefficient for a cone tip is available an analytical expression for the reflection and transmission coefficients at the ogive tip is not available. However, experimental measurements have been performed for a range of tip angles to determine reflection coefficients. Using these measurements Peters [42] has determined the ogive attenuation factor previously cited.

Figure 35 shows the ogive and the coordinate system. As in the case of the prolate spheroid, incident energy is trapped at points A and B where the incident vector is normal to the surface. These creeping waves travel along the ogive until they encounter the tip.

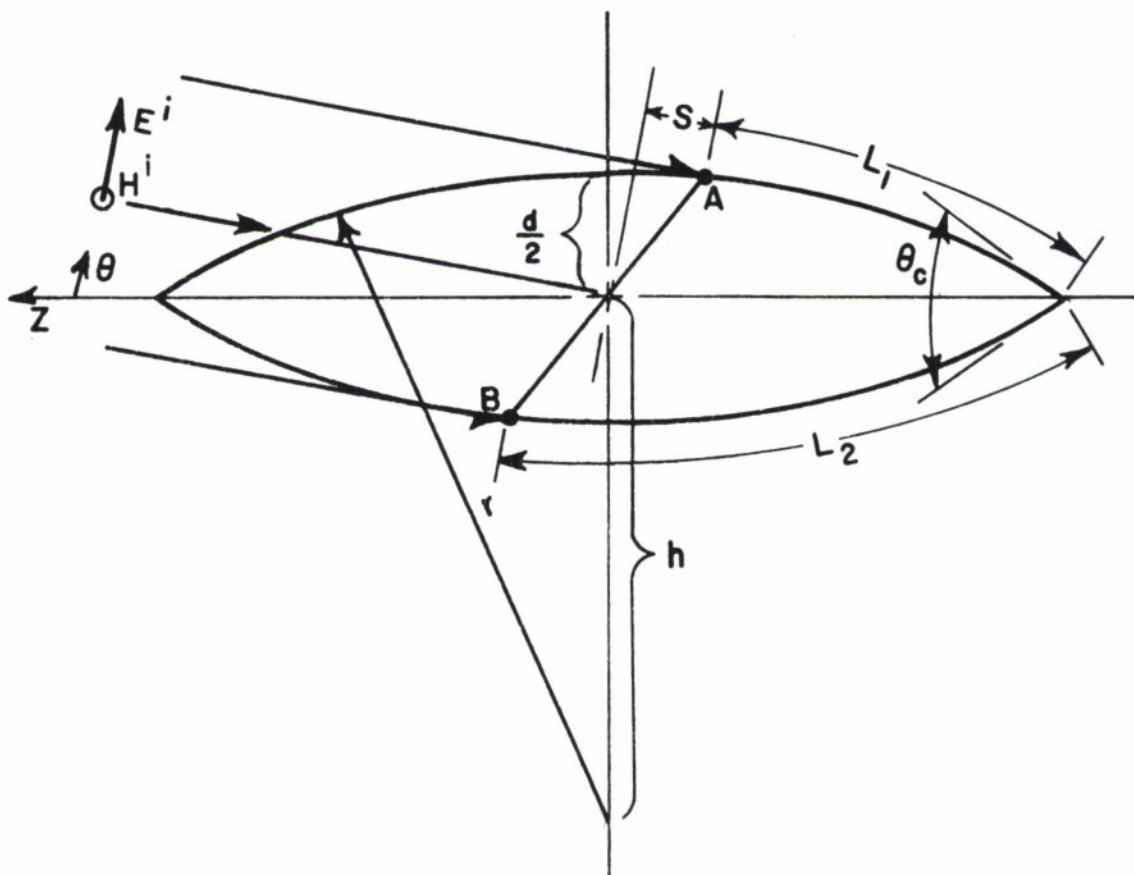


Fig. 35--Coordinate system for the ogive.

At the tip, part of the creeping-wave energy is diffracted as creeping waves on all geodesics containing the tip and the remainder is radiated from the tip. The previous treatment[ 35] assumed that the creeping-wave fields on all of the geodesics have equal magnitudes. This is only approximately correct. Small differences in the magnitude of diffracted rays for different geodesics will yield the on-axis creeping-wave field which can be observed in the measurements reported by Blore[ 44] . Off-axis the creeping wave return is a result of the creeping waves which propagate on the ogive in the plane defined by the incidence direction and the incident E-field. In this plane the effect of the tip can be characterized by reflection and transmission coefficients at the tip.

Referring to Fig. 35, the backscattered fields attributed to the creeping-wave fields may be written as

$$\begin{aligned}
 (90) \quad E_{cw}^s &= E^i \cdot D^2 \{ R_t [ e^{-(jk_o + \alpha_{og}) 2L_1} e^{-2k_o S} \\
 &+ e^{-(jk_o + \alpha_{og}) \cdot 2L_2} e^{j2k_o S} ] \\
 &+ 2T_t [ e^{-(jk_o + \alpha_{og}) (L_1 + L_2)} ] \} \frac{e^{-jkR}}{\sqrt{2\pi R}}
 \end{aligned}$$

where  $D^2$  is the diffraction coefficient given in Eq. (86)  
 $R_t$  is the tip reflection coefficient  
 $T_t$  is the tip transmission coefficient  
 $\alpha_{og}$  is the ogive attenuation coefficient  
 $L_1, L_2$  are shown in Fig. 35, and  
 $S$  refers the phase to the center of the ogive.

For the spherical ogive  $R_t = -T_t = \Gamma$  approximately, and values of  $\Gamma$  have been obtained experimentally. Bistatic radar cross section measurements of the ogive have shown that the energy incident on the tip is scattered by the tip along each geodesic on the ogive, i. e., these tip-scattered fields show no  $\phi$  dependence. This agrees with the results of the equivalent antenna approach, for which no  $\phi$  variation of the field was assumed. Thus a factor of  $1/\sqrt{2\pi}$  is introduced to account for the lack of  $\phi$  dependence of the tip-scattered fields.

The radar cross section of the ogive calculated using Eq. (90) with  $\Gamma = 0.54$  is compared with the experimental results and with the echo area calculated by the equivalent antenna approach in Fig. 36. In this figure the equivalent antenna solution has been corrected for radiation loss using the ogive attenuation factor as described by Peters[ 42] .

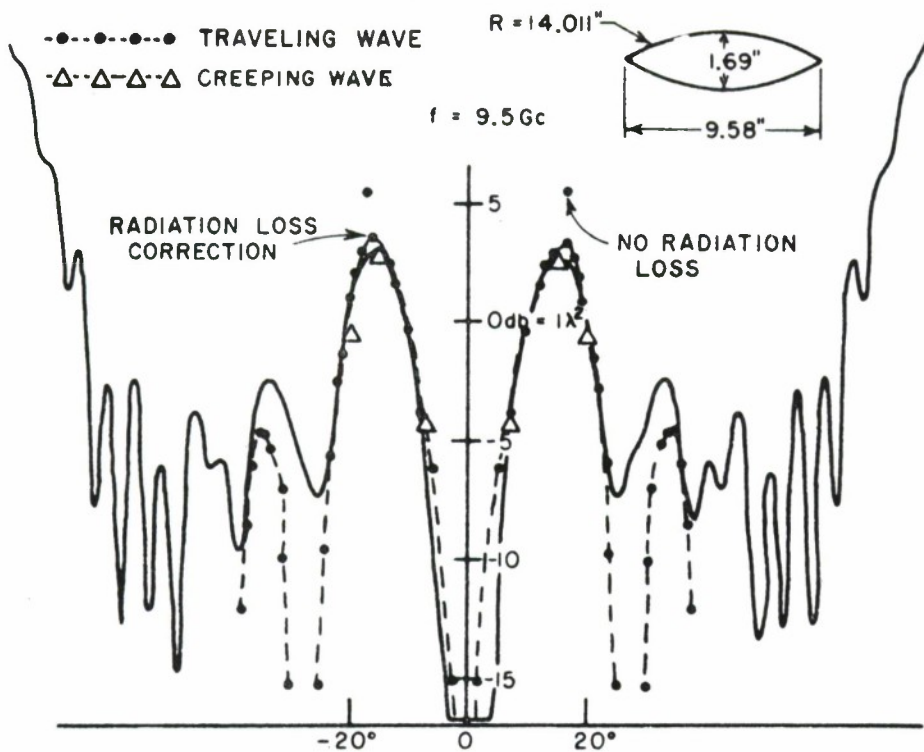


Fig. 36--Backscattered field patterns for the ogive.

Moreland, et al. have applied creeping-wave theory to analysis of a spherically capped ogive as shown in Fig. 37. This body represents another target having a discontinuity in the shadow zone. They have expressed the scattered field as [35]

$$(91) \quad E_s = E_i D^2 e^{-2\gamma_{og} r\theta_0} \left\{ \Gamma \left[ e^{-j2k_0 \ell} + 2\gamma_{og} r\theta + e^{-2\gamma_{og} r\theta} \right] \right. \\ \left. + 2T_{os} T_{so} \left[ e^{-(jk_0 \ell + \gamma_s r_s 2\theta_1 + j\pi)} \right] \right\} \frac{1}{\sqrt{2\pi R}} e^{-jkR}$$

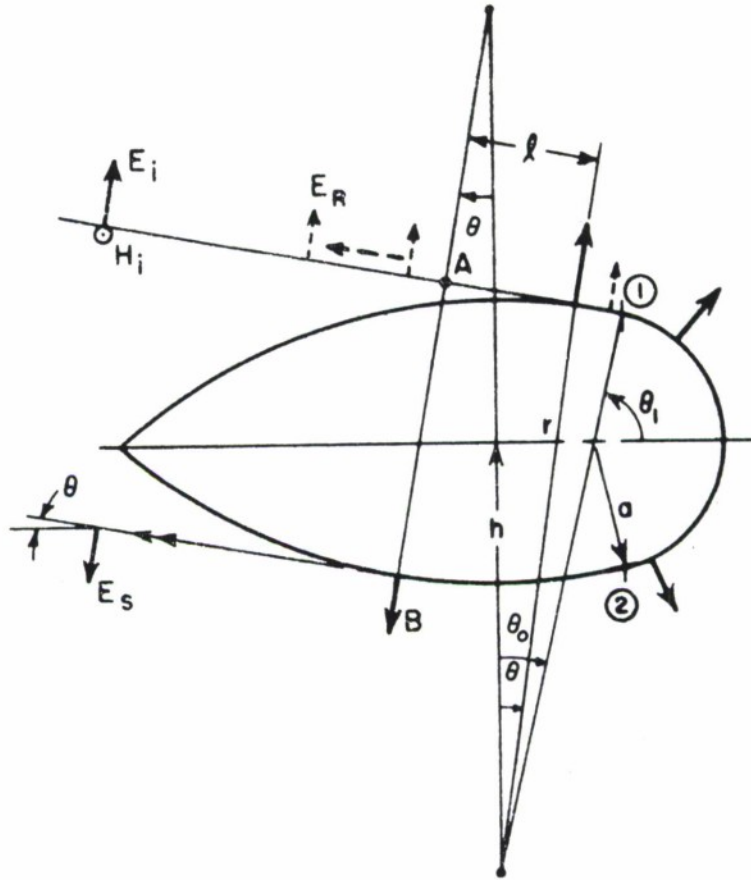


Fig. 37--The spherically capped ogive.

where  $\gamma_{og} = jk_0 + \alpha_{og}$ ,  
 $r$  = radius of curvature of the ogive  
 $r_s$  = radius of the spherical cap,  
 $\theta_0, \theta_1$  = angles shown in Fig. 37,  
 $\alpha_{og}$  = attenuation coefficient of ogive,  
 $D^2$  = diffraction coefficient, given in Eq. (86)  
 $\gamma_s = jk_0 + \alpha_s$ , and  
 $\alpha_s$  = attenuation coefficient of the sphere.



The reflection coefficient,  $\Gamma$ , and the transmission coefficients,  $T_{Os}$  and  $T_{sO}$ , arise because of the change of surface impedance at the junction of the ogive and sphere. The surface impedance of the ogive is taken to be  $Z_o$ , the impedance of free space, and the surface impedance of the sphere is taken to be the ratio of  $E_o$  to  $H_o$  for the fields of the major creeping waves postulated in Eqs. (76) and (77) for the sphere. Referring to Fig. 20 we see that this ratio is dependent upon the sphere radius and can be determined from the exact fields of the sphere for a given radius. Thus  $\Gamma$  and  $T_{Os}$  can be written as

$$(92) \quad \Gamma = \frac{Z_s - Z_o}{Z_s + Z_o}$$

and

$$(93) \quad T_{Os} = \frac{2Z_s}{Z_s + Z_o}$$

It is necessary to make  $\Gamma$  the negative of Eq. (92) in order to obtain agreement with the shape of the experimental curves. This sign appears since the discontinuity acts as a line scatterer or a caustic.

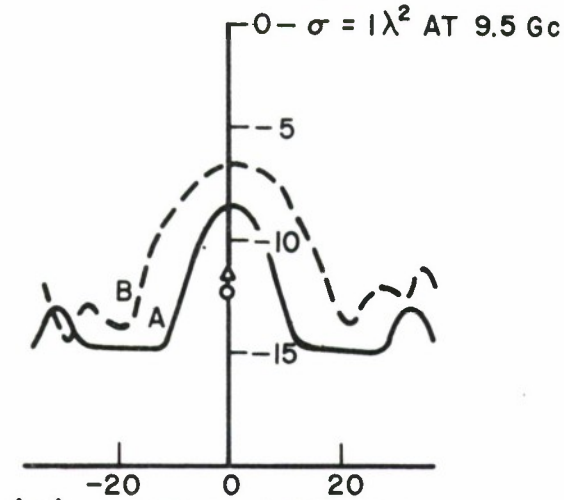
The ray passing through it undergoes a phase shift of  $\pi/2$  radians and the transmitted ray passes through two such discontinuities. In addition, the factor  $1/\sqrt{2\pi}$  proposed by Moreland, et al. is retained to account for the rotational symmetry of the caustic which causes diffracted rays to propagate along the spherical cap in directions

other than that of the plane of incidence, thus decreasing the backscattered field. Combining all the terms the total expression for the backscattered field is

$$(94) \quad E_s = E_i D^2 e^{-2\gamma_{og} r \theta_o} \{ \Gamma [ e^{-j2k_o \ell} + 2\gamma_{og} r \theta} + e^{-2\gamma_{og} r \theta} ] \\ + 2 T_{os} T_{so} [ e^{-j(k_o \ell + \gamma_s r_s 2\theta_1 + j2\pi)} ] \} \frac{1}{\sqrt{2\pi R}} \frac{e^{-jkR}}{R} .$$

The results of the computation for the spherically capped ogive are presented in Fig. 38 and compared with experimental measurement. It is seen that in the near nose-on region the results are in good agreement with measurement. This form of creeping-wave analysis, coupled with the traveling wave picture and physical optics, allows prediction of the backscattered field of the ogive over a wide range of incidence directions and  $k_o a$  values. It should be noted that the impedance of the creeping wave is obtained by a best fit of the fields at the surface of the sphere in the entire shadow region. This would include the fields close to the point at the rear. It has been noted that this is a region of poor fit, regardless of the approximation used, because there are fields present here which are not included in the simple creeping-wave picture. This creeping wave picture, as noted previously, does not include a caustic at the point at the

A - CAP RADIUS = 0.807",  $\theta_0 = 4^\circ$  { — MEAS.  
 ▲ APPROX.  
 B - CAP RADIUS = 0.695",  $\theta_0 = 8^\circ$  { - - MEAS.  
 ○ APPROX.



C - CAP RADIUS = 0.509",  $\theta_0 = 12^\circ$  { — MEAS.  
 ▲ APPROX.  
 D - CAP RADIUS = 0.254",  $\theta_0 = 16^\circ$  { — MEAS.  
 ○ APPROX.

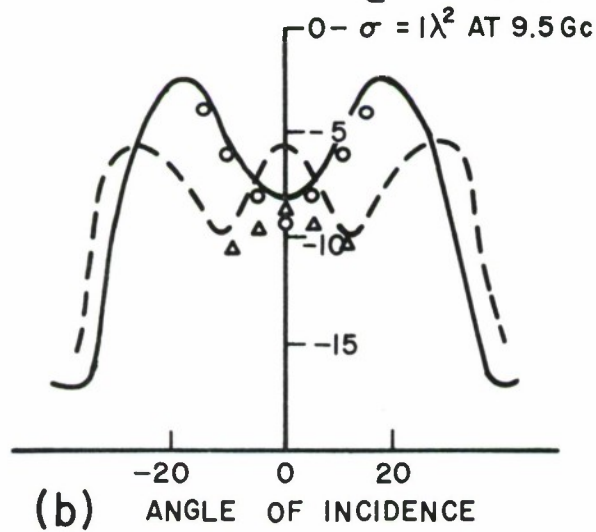


Fig. 38--Backscattered field patterns of the spherically capped ogive.

rear. Further improvement in these results would be anticipated if the fields were more closely matched by two creeping waves at a distance removed from the rear point and if multiple interactions are included.

It is seen that the effects of discontinuities in the shadow zone must be carefully accounted for. Future work in this area devoted to the determination of the reflection and transmission coefficients of tips and wedge discontinuities would provide a more accurate solution for the effects of shadow zone discontinuities.

In summary the attenuation and diffraction coefficients corresponding to the simplified single ray geometry are presented in Table III.

TABLE III  
ATTENUATION AND DIFFRACTION COEFFICIENTS FOR THE  
SIMPLIFIED SINGLE RAY PATH GEOMETRY

TARGET	$D^2$	$\infty$
Cylinder	$0.81 \rho^{\frac{1}{3}} \lambda^{\frac{1}{6}} e^{-j\pi/12}$	$[1.48 e^{-0.84(\rho_P/\rho_O)} + 0.20] \rho_P^{-\frac{2}{3}} \lambda^{-\frac{1}{3}} e^{j\pi/6}$
Finite closed body	$0.27(\rho_A \rho_B)^{\frac{1}{6}} \lambda^{\frac{2}{3}} e^{-j\pi/12}$	
Edge type target	$0.09(\rho_A \rho_B)^{\frac{1}{6}} \lambda^{\frac{2}{3}} e^{-j\pi/12}$	$0.20 \rho_P^{-\frac{2}{3}} \lambda^{-\frac{1}{3}} e^{j\pi/6}$

where  $\rho_A, \rho_B$  are radii of curvature at points of attachment and reradiation  
 $\rho_P$  is the radius of curvature in the propagation direction  
 $\rho_O$  is the radius of curvature in the direction orthogonal to propagation.

### E. The Extension of Creeping-Wave Analysis to Disks

The simplified ray path geometry suggests the examination of radar targets where only one possible creeping-wave path exists. Such a class of targets are disks, for incident plane waves in and polarized in the plane of the disk. A new solution for this class of targets may be obtained by assuming that a creeping-wave field can exist on the edge of the disk in such a case and that the functional forms of the diffraction and attenuation coefficients which have been used for volumetric shapes apply. Thus we write for one component of the creeping-wave field

$$(95) \quad E^{CW} = E^i D_d^2 e^{-\alpha_d l} e^{-jk l} e^{-jkR/R}$$

where  $E^{CW}$  is the scattered creeping-wave field

$E^i$  is the incident field

$\alpha_d$  is the complex attenuation coefficient

$l$  is the path length traversed on the edge

$D_d^2$  is the product of the diffraction coefficients

at the points of attachment and reradiation.

For elongated targets such as ogives the radius of curvature in the direction of propagation ( $\rho$ ) of the creeping wave is much greater than the orthogonal radius of curvature ( $\rho_0$ ) for the case of near-nose-on backscatter where the creeping wave contribution is dominant. If the circular disk is considered to be a limiting case of an oblate spheroid as the ratio of minor to major axes becomes small, it is seen that the ratio ( $\rho/\rho_0$ ) is large as in the case of the ogive. Thus it is reasonable to apply the ogive attenuation coefficient to the disk. Thus for the disk we take

$$(96) \quad \alpha = 0.20 e^{-j\pi/6} \rho^{-\frac{2}{3}} \lambda^{-\frac{1}{3}}$$

where  $\rho$  is the radius of curvature in the direction of propagation.

In order to obtain the diffraction coefficient it is assumed that the functional form is

$$(97) \quad D_d^2 = A \rho^{\frac{2}{3}} \lambda^{\frac{1}{3}} e^{-j\pi/12}$$

We now write the scattered field of the ogival disk as

$$(98) \quad E^{cw} = \gamma D_d^2 E^i \left( e^{-2(+jk_0 + \alpha)l_1} + e^{-2(+jk_0 + \alpha)l_2} - 2 e^{-(jk_0 + \alpha)(l_1 + l_2)} \right)$$

where  $\gamma$  is the measured voltage reflection coefficient of the tip (+0.73 for the ogive treated) and

$l_1$  and  $l_2$  are shown in Fig. 39.

Now, adjusting the constant A to agree with data as shown in Fig. 39 we find that  $A = 0.1$  approximately. We now apply the above attenuation and diffraction coefficients to the cases of circular and elliptical disks. However, we first need to obtain an expression for the diffracted field at the specular point for these targets.

For a disk the diffracted field at the specular point can be written using Eq. (6) as

$$(99) \quad E^{sp} = E^i D_w \sqrt{d/(d+R)}$$

where  $E^{sp}$  is the specularly diffracted field

$D_w$  is the wedge diffraction coefficient

$d$  is the distance from the specular point to the caustic of the diffracted rays in the plane of the disk and

$R$  is measured from the specular point.

In the case of the circular disk shown in Fig. 40 we have  $d = a/2$ . For a disk the wedge diffraction coefficient becomes

$$(100) \quad D_w = -e^{-j(kR + \pi/4)} / \sqrt{2\pi kR} \quad .$$



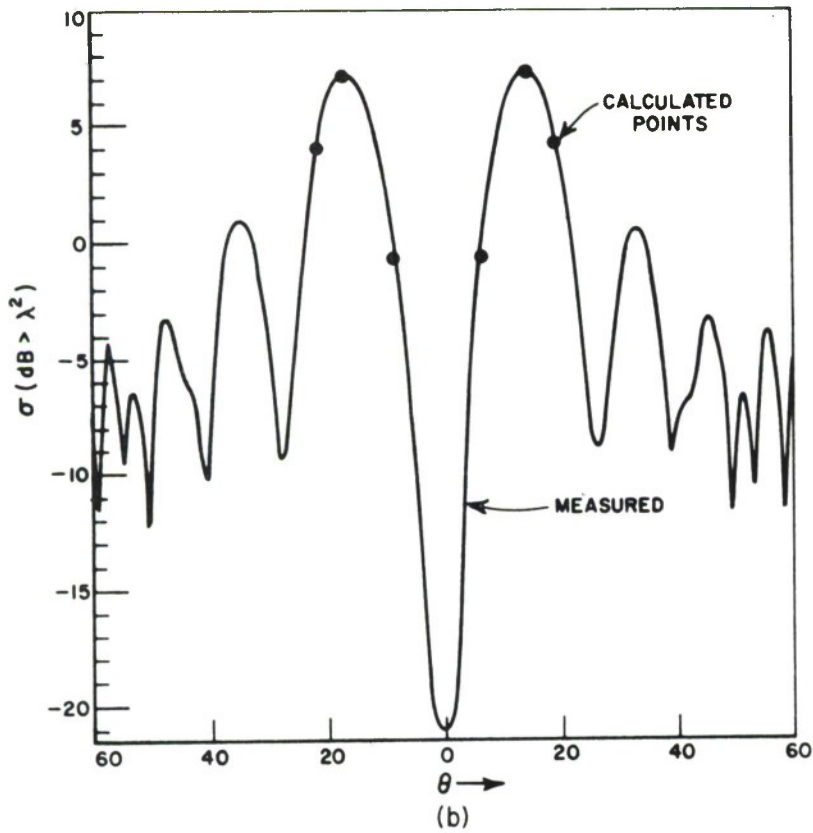
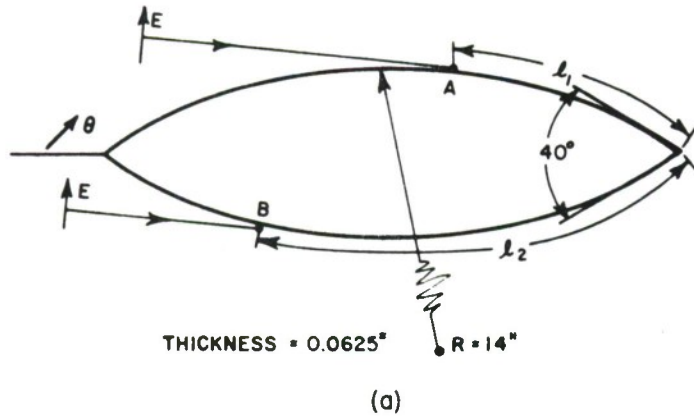


Fig. 39--Backscattered field pattern of the ogival disk.

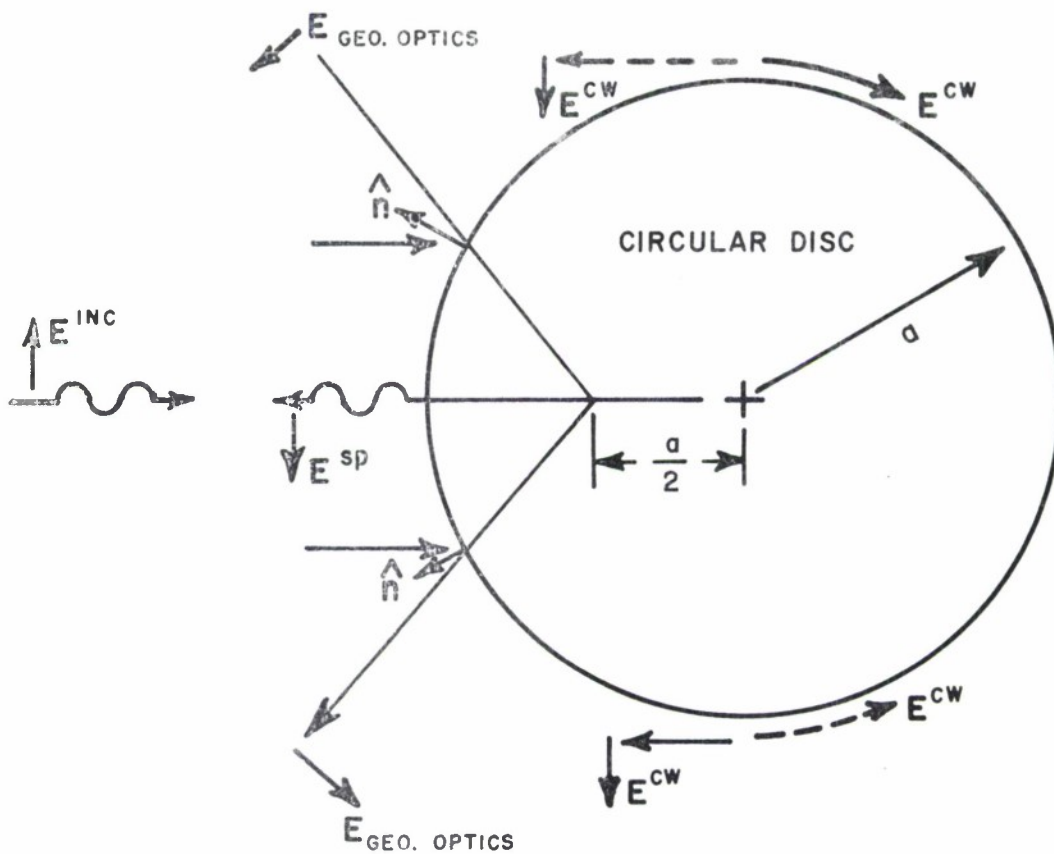


Fig. 40--Scattering by a circular disk edge-on.

Combining Eqs. (99) and (100) and taking the phase reference at the specular point we may write for the circular disk

$$(101) \quad E^{sp} = -\frac{1}{2} E^i \sqrt{a/\pi k} e^{-j\frac{\pi}{4}} e^{-jkR/R} \quad .$$

A similar expression can be derived for the elliptical disk. For the circular and elliptical disks we now write the total scattered field as

$$(102) \quad E_{tot}^{tot} = E_{tot}^{cw} + E^{sp} \quad .$$

The radar cross section for the circular disk and results for a 2:1 elliptical disk obtained using this approach are presented in Figs. 41 and 42. In some cases the measured data is presented as a line representing the maximum and minimum echo as read from the measured pattern. For the elliptical disk it is seen that good results are obtained for  $1.5 < ka < 5$ , while the results for the circular disk are good for  $ka > 1$ .

Thus empirical attenuation and diffraction coefficients are obtained which yield results in good agreement with measurements for ogival, circular, and elliptical disks. The agreement between theory and experiment demonstrates that the concept of the creeping wave may be applied to disks, for waves incident in, and polarized in, the plane of the disk.

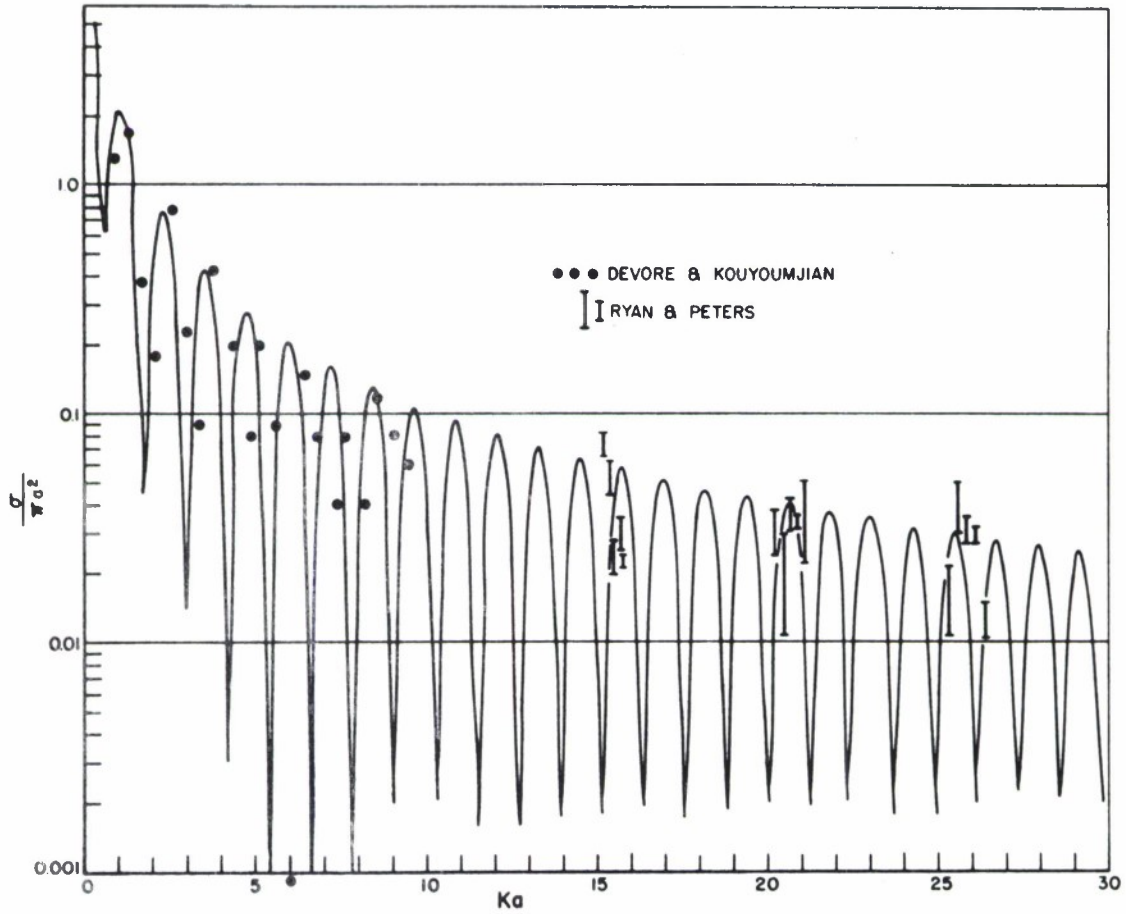
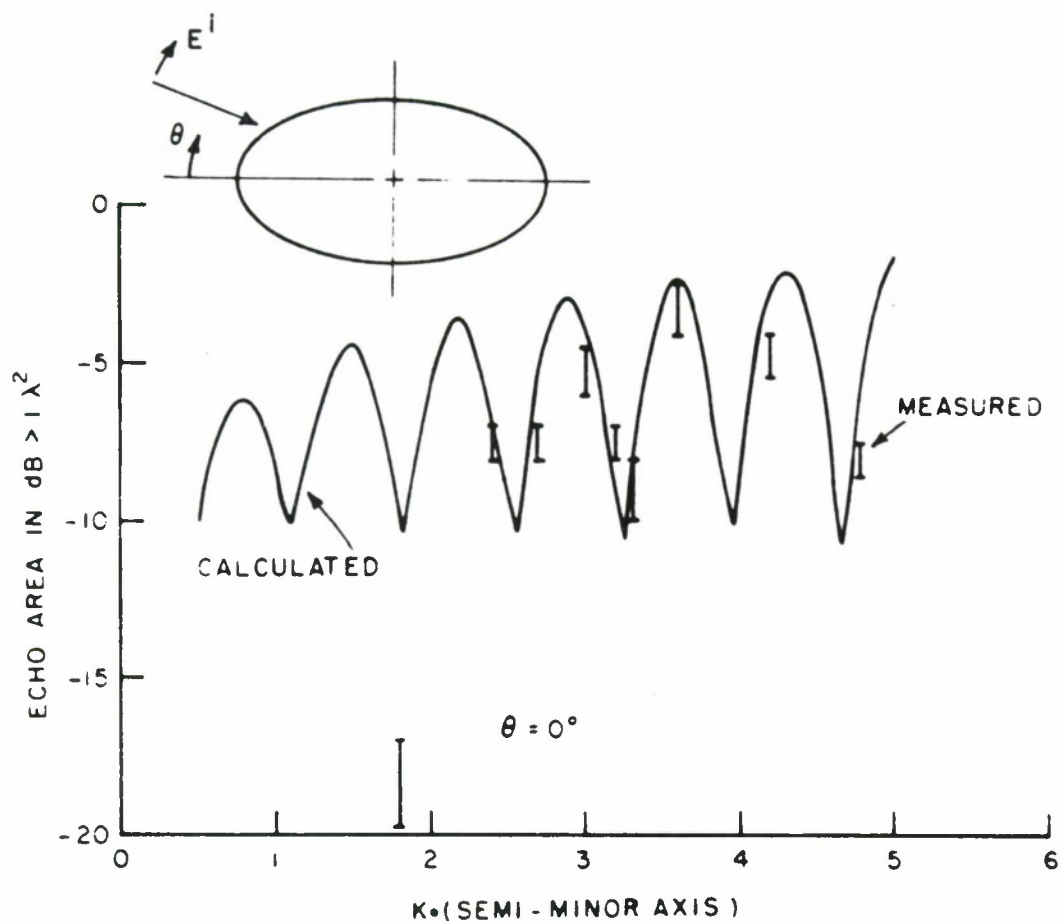
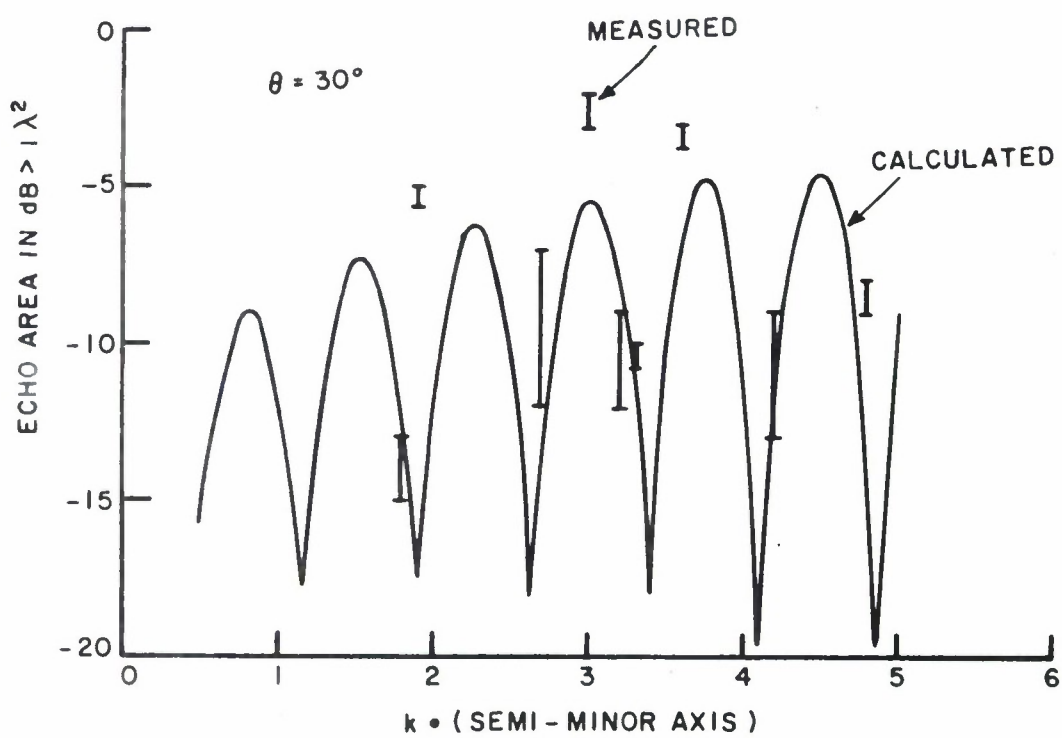


Fig. 41--Radar Cross section of a circular disk edge-on.



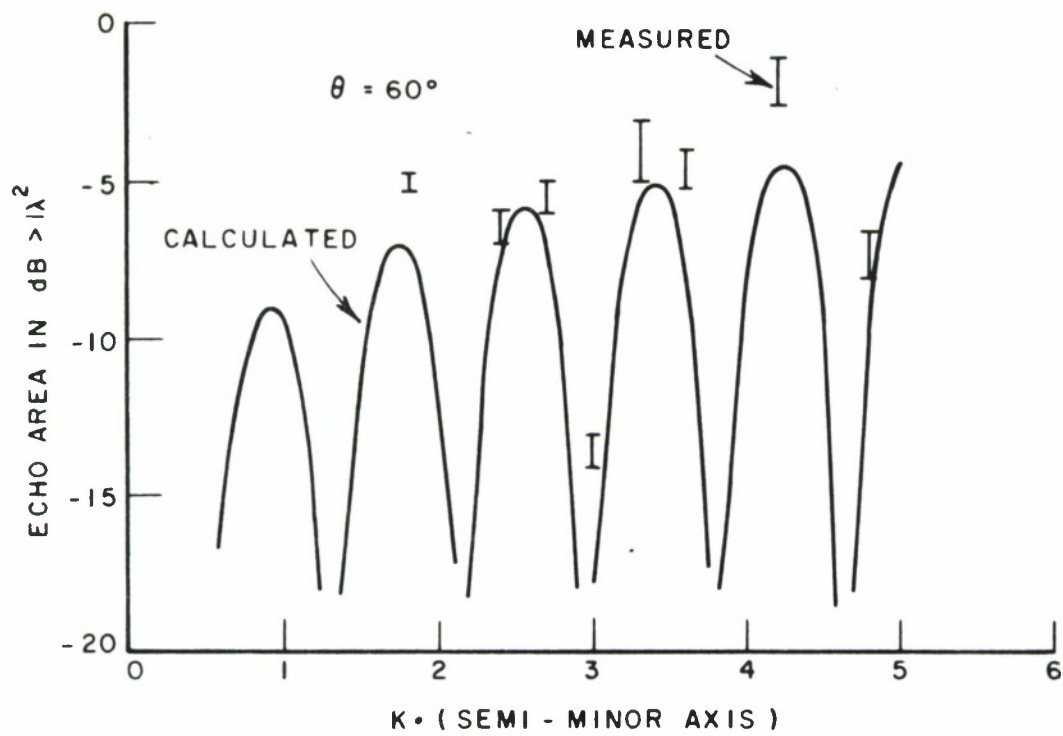
a.

Fig. 42(a)--Radar cross section of a 2:1 elliptical disk edge-on



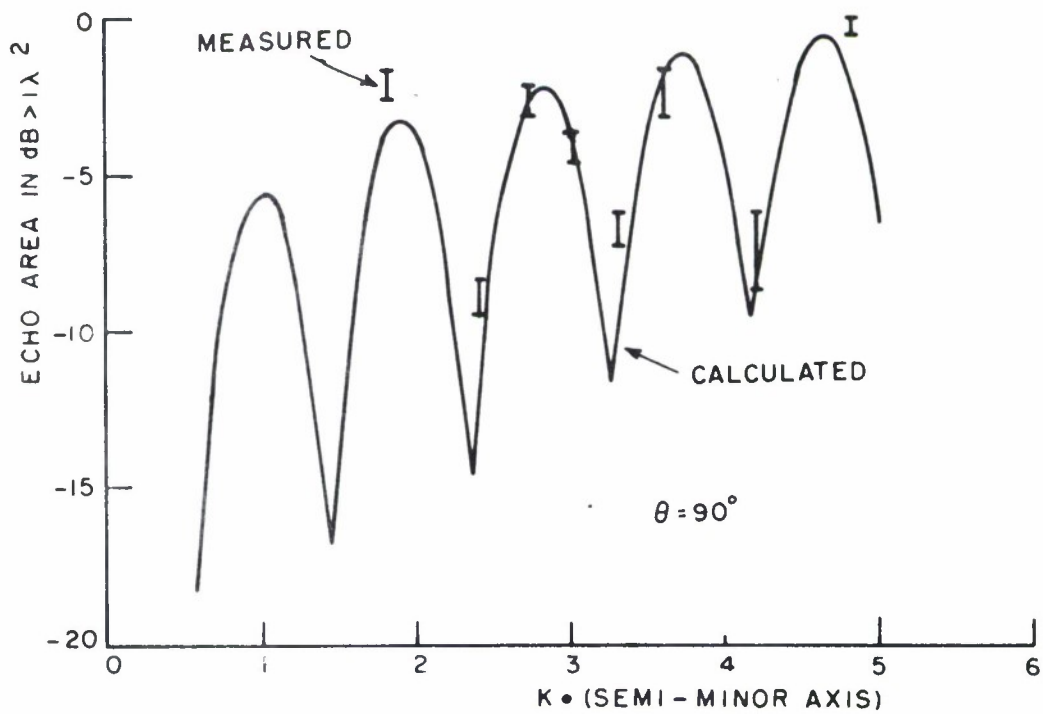
b.

Fig. 42(b)--Radar cross section of a 2:1 elliptical disk edge-on.



c.

Fig. 42(c)--Radar cross section of a 2:1 elliptical disk edge-on.



d.

Fig. 42(d)--Radar cross section of a 2:1 elliptical disk edge-on.



## CHAPTER V COMPUTER PROGRAM RESULTS

The theory discussed in the preceding text has been applied to the determination of the radar cross section of targets of revolution through the development of two computer programs. These programs are discussed in Appendix V. The programs have been tested for horizontal polarization backscatter for circular cylinders, cones, double cones, conically capped cylinders, prolate spheroids, a prolate spheroid-sphere combination and a prolate spheroid-oblate spheroid combination. The targets are shown in Fig. 43, and the corresponding patterns are shown in Figs. 44 to 49. The agreement between the measured and calculated echo area patterns is an indication of the accuracy of the various techniques used in the computer program. The solution corresponding to each region of the pattern is identified in Figs. 44 to 49. The results for each of the targets will be discussed individually in the following paragraphs.

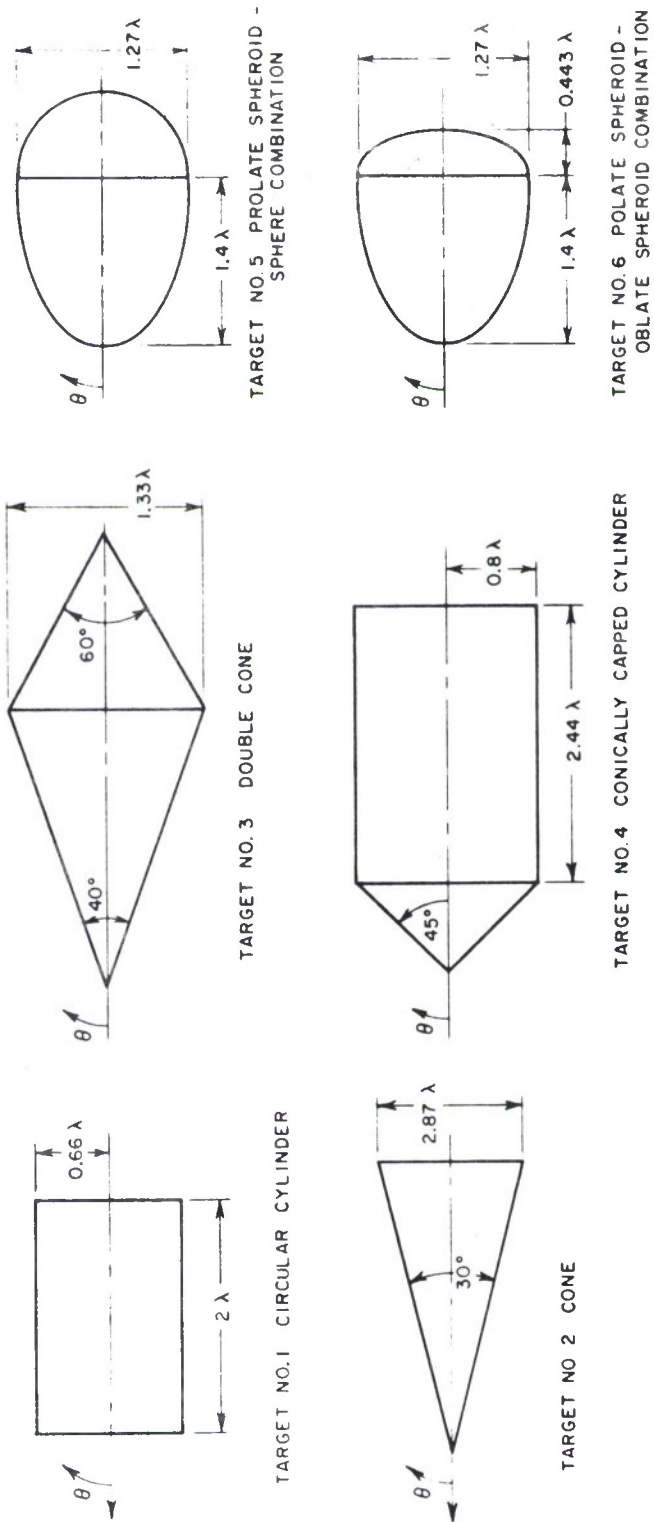


Fig. 43--Test targets for the geometrical optics and creeping wave sections of the computer program.

### A. Circular Cylinder

The measured and calculated patterns for the circular cylinder are presented in Fig. 44. As indicated in the figure, the solution for the axial caustic, the single diffraction solution, and the solution for the specular direction have been used to calculate the echo area pattern. For the region close to the axial caustic (i. e.,  $\theta$  close to  $0^\circ$  or  $180^\circ$ ) the agreement is excellent. The magnitude of the echo area on axis is within 1 dB of measurement. In addition the location of the first null of the calculated and measured patterns is the same, although the depths of the measured and calculated nulls do not agree. For the region close to the specular direction (i. e.,  $\theta$  close to  $90^\circ$ ) the agreement is excellent, being within 1 dB at the specular direction. Again the position of the first null of the calculated and measured patterns agrees. The depths of the measured and calculated nulls are also in reasonable agreement, having an error of approximately 5 dB. The remainder of the pattern is calculated using the single diffraction solution. This region shows a slight null shift between the calculated and measured patterns. The magnitudes of the calculated and measured peaks are within 3 dB. The accuracy obtained for the circular cylinder is within  $\pm 1$  dB of the accuracy obtained by Ufimtsev[ 22] and is the same as the accuracy obtained by Bechtel and Ross[ 45] using

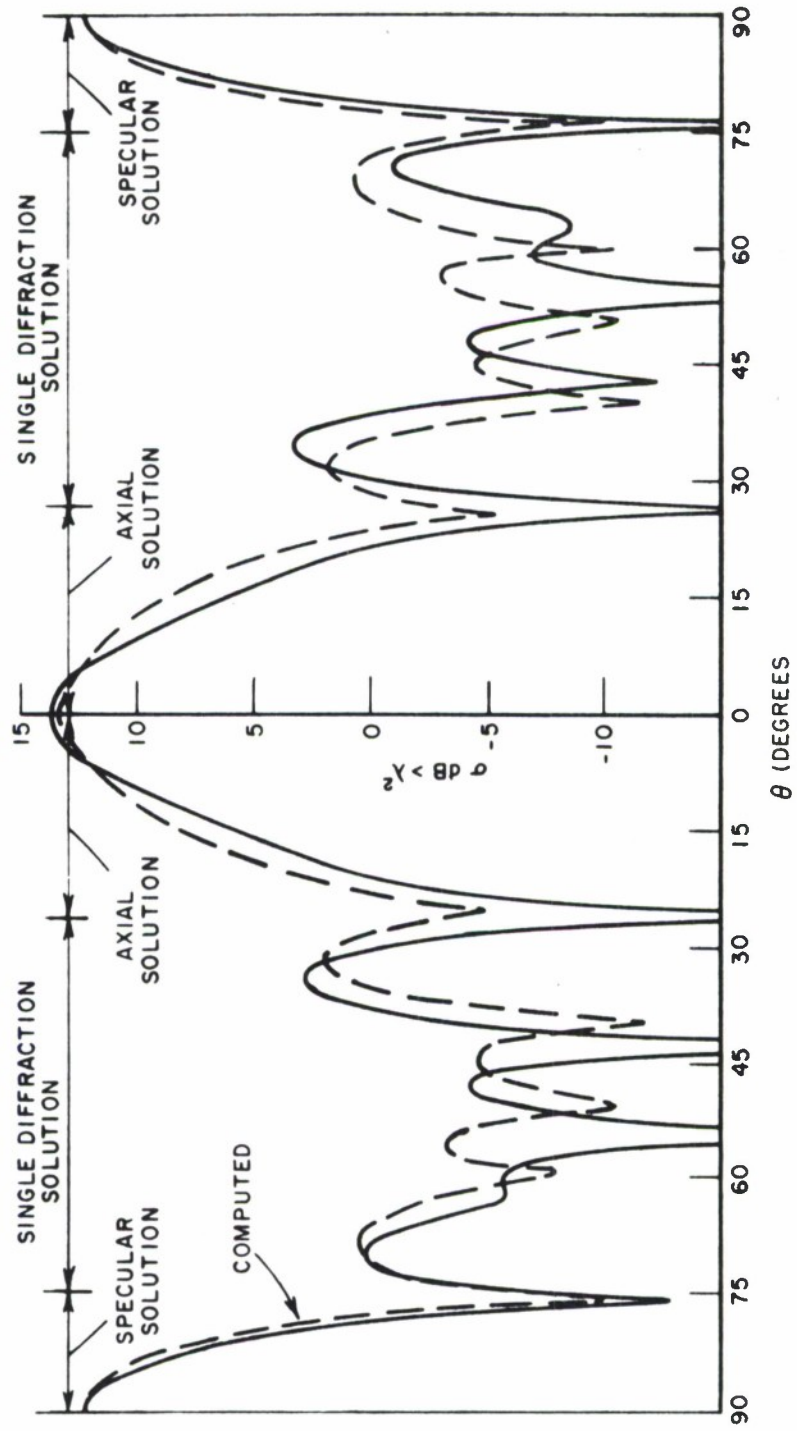


Fig. 44--Monostatic echo area of the circular cylinder.

singly diffracted components. These results demonstrate that the computer solution is valid for a cylinder.

### B. Cone

The measured and calculated patterns for the cone are presented in Fig. 45. The measurements were performed by Keys and Primich[ 46] . As indicated in the figure, the solution for the axial caustic, the single diffraction solution, and the solution for the specular direction have been used to calculate the echo area pattern. A diffraction solution for the cone has also been presented by Bechtel[ 47] which did not include an axial caustic correction and consequently is in error for axial incidence. The measured data is shown as a range of values. The calculated pattern is seen to be in good agreement with the measured values over the entire range of incidence angles. However, it is noted that the accuracy of the measurements is not good, having a variation of approximately 5 dB. Thus it is difficult to specify an absolute accuracy for the solution by comparison to the data. However, the agreement obtained indicates that the computer solution is valid within the accuracy of the measurements.

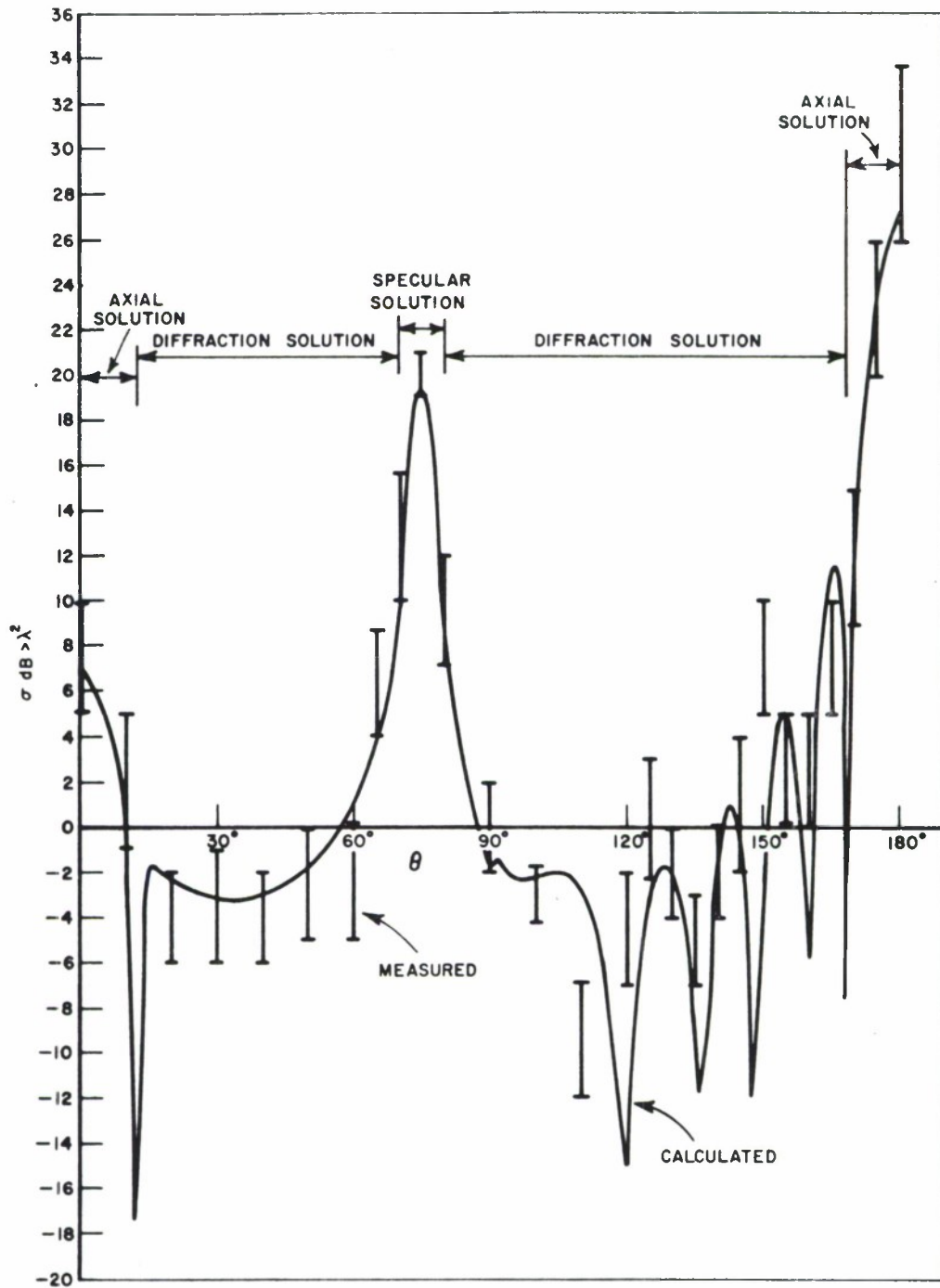


Fig. 45--Monostatic echo area of the cone.

### C. Double Cone

The measured and calculated patterns for a double cone are presented in Fig. 46. As shown in the figure the solution for the axial caustic, the single diffraction solution and the solution for the specular region have been used to compute the echo area pattern. As seen from the figure the agreement close to the axial caustics (i. e.,  $\theta$  close to  $0^\circ$  or  $180^\circ$ ) is excellent. On the caustic the measured and calculated echo areas are within  $\frac{1}{2}$  dB, and the location of the first nulls is in error by only  $2^\circ$ . The peaks of the specular solution are within 2 dB of the measured peaks. The remainder of the calculated pattern is not in good agreement with the measurement, although the characteristics of the pattern are indicated by the calculations. Comparison of the measured and calculated patterns shows that nulls which appear in the calculated pattern are filled in the measured pattern. In addition, there is a peak at  $\theta = 90^\circ$  which is not predicted by the calculations. These results indicate that higher-order diffraction terms are significant for this target, at aspects removed from the axis. Also as this target is small in terms of wavelength ( $a = 0.667\lambda$ ) higher-order interactions are to be expected. Improved results would be anticipated if the scattering from the tips of the cones, and the interactions between the joint and the cone tips were included in the

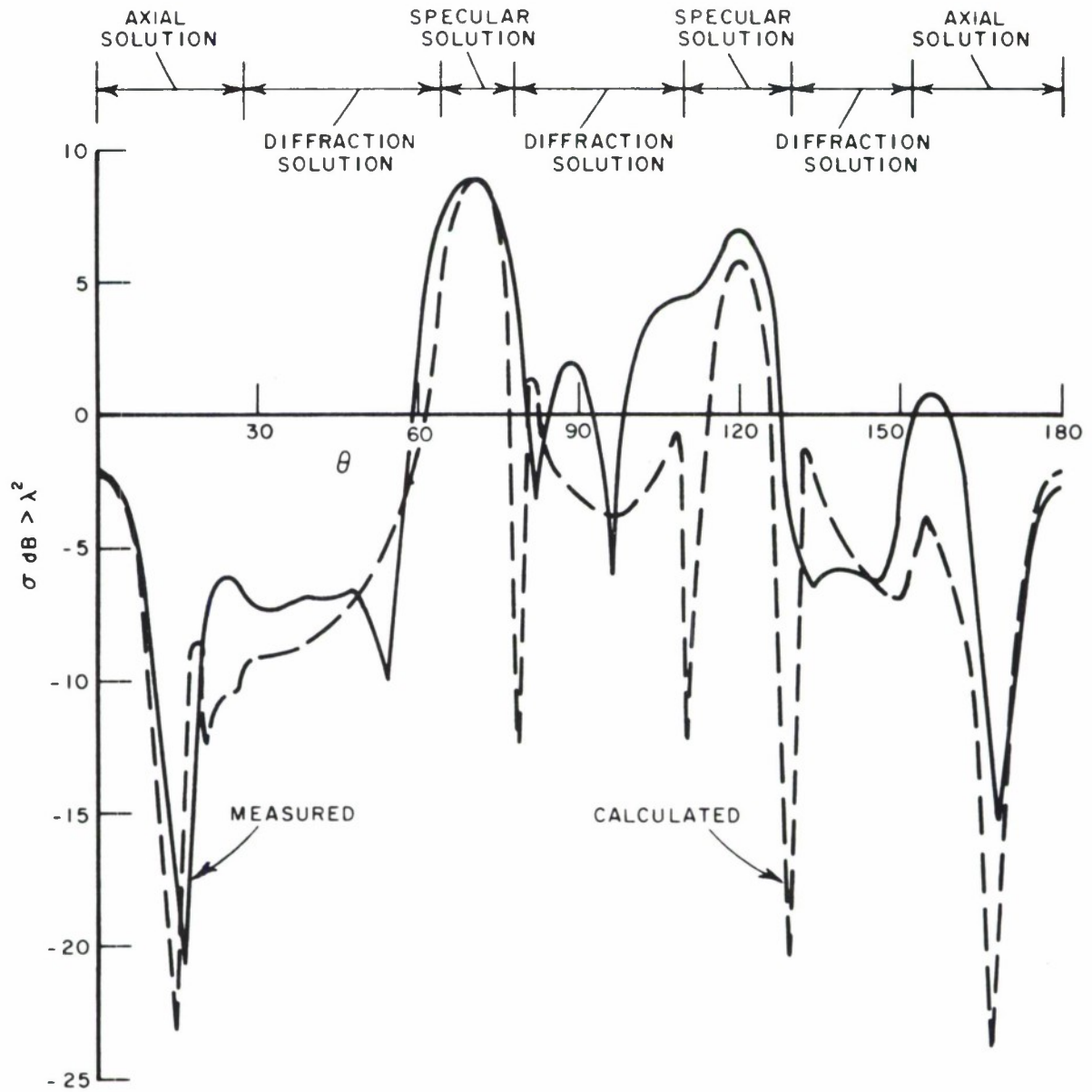


Fig. 46--Monostatic echo area of the double cone.



solution. In order to accomplish this task the diffraction coefficient for a cone tip is needed. Such a diffraction coefficient for arbitrary angles of incidence and diffraction is not known. Thus further theoretical study is required before a more accurate solution for this target can be obtained.

#### D. Conically Capped Cylinder

The conically capped cylinder represents a more complicated target, which approximates a practical target. The measured and calculated patterns are shown in Fig. 47. As indicated in the figure the solution for the axial caustic, the single diffraction solution and the solution for the specular region have been used to calculate the echo area pattern. The regions close to and on the axis (i. e.,  $\theta$  close to  $0^\circ$  or  $180^\circ$ ) are in agreement within 2 dB. The specular region ( $\theta$  close to  $90^\circ$ ) is in agreement within 1 dB. The specular region normal to the cone ( $\theta$  close to  $45^\circ$ ) is not in good agreement, having several nulls in the calculated pattern which do not agree. It is noted that these nulls occur at the angles where the solution shifts from a diffraction solution to the specular solution and vice versa. The peak of the specular solution is within 3 dB of the measured values in this region. It is noted that the diffraction solution is within 3 dB of the measurements except for the region close to the normal to the cone. As the error is due to the fact that the calculated nulls

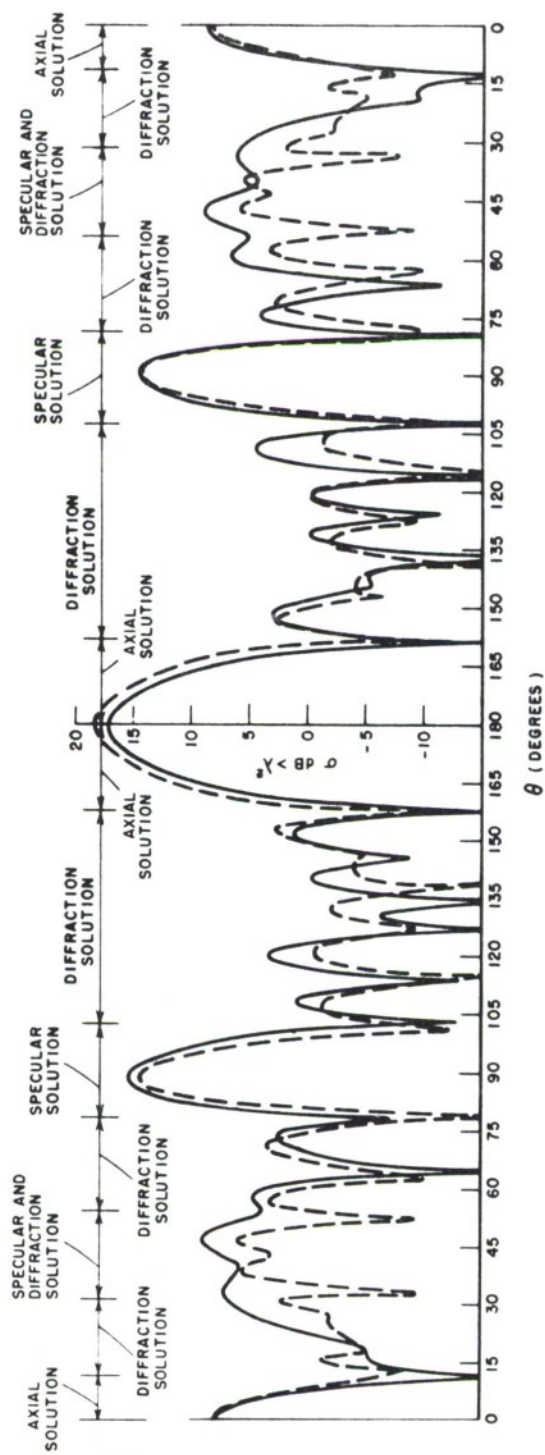


Fig. 47--Monostatic echo area of the conically capped cylinder.

in this region are filled in, this error may be attributed to higher-order diffractions between the cone tip and the junction between the cone and cylinder, and to scattering by the cone tip, both of which have been neglected in this solution. An additional source of error may be attributed to the target used for the measurement. The joint between the cone and cylinder was machined with a radius curve. Thus the wedge diffraction coefficient may not accurately describe the actual scattering mechanism at the joint. In spite of these disagreements the over-all character of the scattering pattern is predicted by the computer program, and except for the specular region of the conical section the average error is less than 3 dB.

#### E. Prolate Spheroid

The solutions used for this smooth target are the geometrical optics solution for the specular point, and the creeping wave solution. As a test of the general creeping wave program the 2:1 prolate spheroid patterns previously computed using a special case program which were presented in Fig. 31 were re-computed using the general program. The results were identical to the results presented in Fig. 31 for an attenuation coefficient magnitude of 0.55. Thus the error is the same as shown in Fig. 31, being less than 3 dB for a

minor axis greater than  $\frac{1}{2}$  wavelength. These results indicate that the generalized portions of the computer solution were operating correctly. Next, some composite shapes were examined.

#### F. Prolate Spheroid-Sphere Combination

The prolate spheroid-sphere combination represents a two section, continuously curved target with no discontinuity in the first derivative of the surface at the join. The measured and calculated patterns for this target are shown in Fig. 48. As in the case of the prolate spheroid, the geometrical optics and creeping wave solution were used for all aspect angles to calculate the scattered fields. The agreement between measured and calculated patterns is good, being within 3 dB for aspects more than  $30^\circ$  removed from the axis. Within approximately  $30^\circ$  of the axis of revolution the accuracy is not as good, having an error at the null of the calculated pattern of 5 dB. Away from the null the error is less than 3 dB. This inaccuracy close to the axis is attributed to the effects of the discontinuity in the second derivative of the surface at the join. This discontinuity results in a reflection at the joint as was previously discussed in the case of the spherically capped ogive. These reflections are not accounted for in this program. Improved results would be expected if

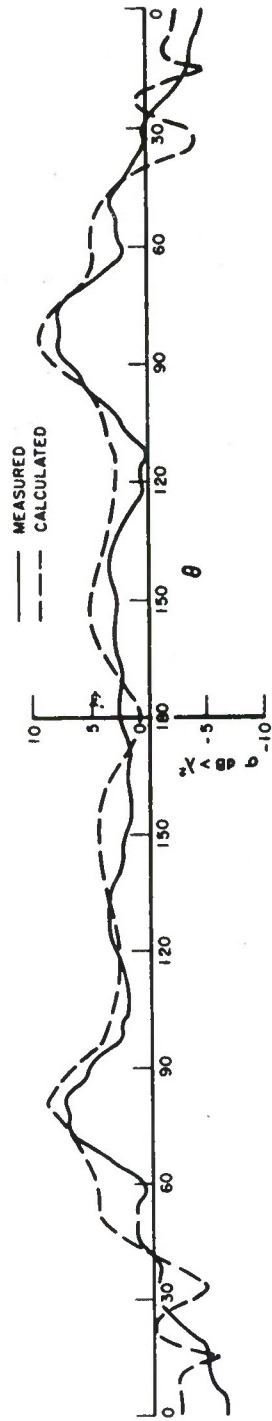


Fig. 48--Monostatic echo area of the prolate spheroid-sphere combination.

this reflection were accounted for. An additional improvement would be expected if a more accurate solution for the scattered fields due to the illuminated region were used.

G. Prolate Spheroid-Oblate Spheroid Combination

The measured and calculated patterns for the prolate spheroid-oblate spheroid combination are shown in Fig. 49. This target is similar to the prolate spheroid-sphere combinations with approximately the same results. That is, accuracy with 3 dB for aspects greater than  $40^\circ$  removed from the axis of revolution with errors as large as 8 dB at the calculated nulls within  $40^\circ$  of the axis. The greater discontinuity in the second derivative of the surface at the join for this case results in a larger error in the calculations near the axis than for the prolate spheroid-sphere combination. Again the addition of the reflections due to the join and a more accurate solution for the scattered fields due to the illuminated region would be expected to yield improved results.

The results obtained for the targets discussed above show that the general computer program, incorporating first order diffraction theory, geometrical optics, and creeping wave theory is operable. Improvements in this program have been suggested by the results, and include the use of multiple diffraction, improved

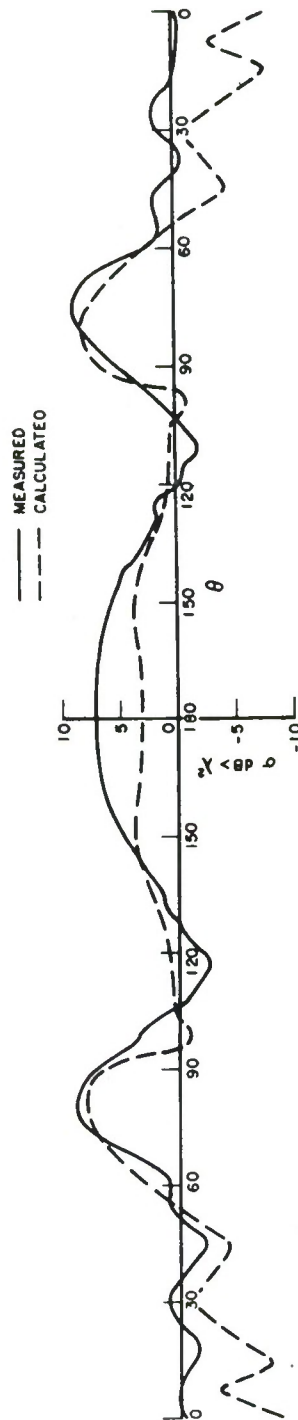


Fig. 49--Monostatic echo area of the prolate spheroid-oblate spheroid combination (parallel polarization).

solutions for the illuminated region and creeping wave reflections. The addition of multiple diffraction to the program is a straightforward but tedious problem. The problems of an improved solution for the illuminated region and of the reflections of the creeping waves, require further theoretical study before they can be included in a general computer solution.

It may be concluded that the general computer program yields results which are useful in the estimation of the radar cross section of composite targets. The size of the target in wavelengths will affect the accuracy of the solution. The restrictions on the size of the target for a class of targets can be determined by comparison of the measured and calculated values for a special case, as for a cylinder or spheroid.

In general, the accuracy of the computer solution will improve as the size of the target in wavelengths is increased. Thus if a lower limit on target size for a given accuracy is established for a class of targets, this accuracy will be maintained for larger targets.



## CHAPTER VI CONCLUSIONS

The geometrical theory of diffraction and creeping wave solutions described have been organized in computer programs to calculate the backscattered fields from sectionally continuous bodies of revolution. The results obtained indicate that these techniques are applicable to this problem. The programs have been used to investigate targets having either straight line or curved smoothly-joined profiles. Targets having combination profiles have not been examined. However, the results obtained indicate that targets having such combination profiles can be treated using this analysis, and that an extension of the present computer programs to treat these targets is feasible. This extension would combine the existing computer programs and provide the additional logic required to treat the more general combination target.

The computer analysis would also be improved by including the effects of interactions (i. e. , multiply diffracted waves and reflected creeping waves). The theory of multiple diffraction has been described. The reflection effects are of two kinds: reflection from tips, and reflection from discontinuities in surface derivatives at the junction between analytic sections. The reflection coefficients for tips could be obtained experimentally, and the results fitted by an empirical

curve. The effects of a surface derivative discontinuity can also be treated experimentally, although physical optics is known to give a valid result for this contribution. Thus the effects of reflections could be included in an improved computer analysis.

The effects of fins, ducts, antennas, or other special scatterers may be treated using special programming, and are compatible with the existing program. Also the extension of this analysis to concave targets appears feasible. The results of Hutchins [50] in determining an interior wedge diffraction coefficient could be applied for "corners", and geometrical optics used for the focussing effects of curved concavities.

The programs described in this paper have been tested and have given good results for sectionally continuous targets of revolution having straight line or curved smoothly-joined profiles. Extension of these programs using the techniques described above is feasible. Thus with more effort a computer program which is sufficiently general to treat a great number of practical targets would result.

APPENDIX I  
THE GEOMETRIC PROPERTIES OF A GENERAL  
SECOND ORDER SURFACE OF REVOLUTION

A general second order surface may be described in spherical coordinates by the following equation

$$\begin{aligned}
 (103) \quad & A_1 r^2 \sin^2 \theta \cos^2 \phi + A_2 r^2 \sin^2 \theta \sin^2 \phi + A_3 r^2 \cos^2 \theta \\
 & + A_4 r^2 \sin^2 \theta \cos \phi \sin \phi + A_5 r^2 \sin \theta \cos \theta \sin \phi \\
 & + A_6 r^2 \sin \theta \cos \theta \cos \phi + A_7 r \sin \theta \cos \phi \\
 & + A_8 r \sin \theta \sin \phi + A_9 r \cos \theta + A_{10} r \sin \theta + A_{11} = 0 \quad .
 \end{aligned}$$

For a surface of revolution (i. e., a surface having no  $\phi$  variation) we can reduce Eq. (103) to

$$\begin{aligned}
 (104) \quad & A_{r1} r^2 \sin^2 \theta + A_{r3} r^2 \cos^2 \theta + B_{r1} r^2 \sin \theta \cos \theta \\
 & + A_{r9} r \cos \theta + A_{r10} r \sin \theta + A_{r11} = 0
 \end{aligned}$$

by examining the profile of the surface in the plane  $\phi = 0$ . For the sake of convenience Eq.(104) is written as

$$(105) \quad r^2 U(\theta) + r V(\theta) + A_{r11} = 0 \quad .$$

The properties of this surface which are necessary for a geometrical theory of diffraction analysis are the unit normal vector ( $\hat{n}$ ), the differential arc length on the surface ( $ds$ ), and the radii of curvature in the co-ordinate directions ( $\rho_1$  in the  $\theta$  direction,  $\rho_2$  in the  $\phi$ -direction). The normal vector is most easily obtained through the use of the gradient. Thus

$$(106) \quad \hat{n} = \frac{\nabla [r^2 U(\theta) + r V(\theta) + A_{r11}]}{|\nabla [r^2 U(\theta) + r V(\theta) + A_{r11}]|}$$

Taking the gradient we have

$$(107) \quad \hat{n} = \frac{\hat{r} (2rU + V) + \hat{\theta} (rU_\theta + V_\theta)}{[(2rU + V)^2 + (rU_\theta + V_\theta)^2]^{\frac{1}{2}}}$$

where

$$U_\theta = \frac{\partial U(\theta)}{\partial \theta}$$

$$V_\theta = \frac{\partial V(\theta)}{\partial \theta}$$

for convenience we set

$$(108) \quad S_1 = (2rU + V)$$

$$S_2 = (rU_\theta + V_\theta)$$

Now, using the relations between unit vectors in the  $(r, \theta, \phi)$  and  $(x, y, z)$  systems,

$$(109) \quad \begin{aligned} \hat{r} &= \hat{x} \sin \theta \cos \phi + \hat{y} \sin \theta \sin \phi + \hat{z} \cos \theta \\ \hat{\theta} &= \hat{x} \cos \theta \cos \phi + \hat{y} \cos \theta \sin \phi - \hat{z} \sin \theta \end{aligned}$$

we may write

$$(110) \quad \begin{aligned} \hat{n} &= \frac{1}{[S_1^2 + S_2^2]^{\frac{1}{2}}} \{ \hat{x}[S_1 \sin \theta \cos \phi + S_2 \cos \theta \cos \phi] \\ &+ \hat{y}[S_1 \sin \theta \sin \phi + S_2 \cos \theta \sin \phi] \\ &+ \hat{z}[S_1 \cos \theta - S_2 \sin \theta] \} \end{aligned}$$

The differential arc length ( $ds$ ) may be expressed as the scalar product of the derivative of the position vector with itself.

For a curve given by the relation  $f(u, v) = 0$  we have[ 48]

$$(111) \quad d\bar{r} = \bar{r}_u du + \bar{r}_v dv$$

and the differential arc length is

$$(112) \quad ds^2 = d\bar{r} \cdot d\bar{r}$$

This relation may be written in what is called the First Fundamental Form of differential geometry[ 48] viz.

$$(113) \quad ds^2 = E du^2 + 2F du dv + G dv^2$$

where

$$E = \bar{r}_u \cdot \bar{r}_u$$

$$F = \bar{r}_u \cdot \bar{r}_v$$

$$G = \bar{r}_v \cdot \bar{r}_v$$

We may write the position vector in rectangular coordinates as

$$(114) \quad \bar{r} = \hat{x} r \sin \theta \cos \phi + \hat{y} r \sin \theta \sin \phi + \hat{z} r \cos \theta$$

The  $\theta$  and  $\phi$  derivatives are then

$$(115) \quad \begin{aligned} \bar{r}_\theta = & \hat{x} [r_\theta \sin \theta \cos \phi + r \cos \theta \cos \phi] \\ & + \hat{y} [r_\theta \sin \theta \sin \phi + r \cos \theta \sin \phi] \\ & + \hat{z} [r_\theta \cos \theta - r \sin \theta] \end{aligned}$$

$$(116) \quad \bar{r}_\phi = -\hat{x} r \sin \theta \sin \phi + \hat{y} r \sin \theta \cos \phi$$

The derivative of  $r$  with respect to  $\theta$  is obtained using Eq. (105) as

$$(117) \quad r_\theta = \frac{dr(\theta)}{d\theta} = - \frac{r^2 U_\theta + r V_\theta}{2rU + V} = - \frac{r S_2}{S_1}$$

Next, using Eq. (113) and algebraic manipulation one obtains in

$(r, \theta, \phi)$  co-ordinates

$$(118) \quad E = r^2 + r_\theta^2$$

$$F = 0$$

$$G = r^2 \sin^2 \theta$$

which results yield the arc length on the surface.

In order to obtain the radii of curvature on the surface it is necessary to evaluate the Second Fundamental Form of Differential Geometry[ 48] . This form is as follows,

$$(119) \quad -d\bar{r} \cdot d\hat{n} = e du^2 + 2f du dv + g dv^2$$

in this equation e, f, g can be computed as

$$\begin{aligned} e &= -\bar{r}_u \cdot \hat{n}_u \\ f &= -\bar{r}_u \cdot \hat{n}_v \\ g &= -\bar{r}_v \cdot \hat{n}_v \end{aligned} .$$

Equation (119) is not convenient for computation in the case being examined as it generates a great many terms which must be reduced. An equivalent form which in this case is easy to evaluate is given by Struik[ 48] as

$$(120) \quad \begin{aligned} e &= \bar{r}_{uu} \cdot \hat{n} \\ f &= \bar{r}_{uv} \cdot \hat{n} \\ g &= \bar{r}_{vv} \cdot \hat{n} \end{aligned} .$$

This form reduces the number of terms to be reduced by about 1/2.

Using Eq. (115) we have

$$(121) \quad \bar{r}_{\theta\theta} = \hat{x}[r_{\theta\theta} \sin \theta \cos \phi + 2r_{\theta} \cos \theta \cos \phi - r \sin \theta \cos \phi] \\ + \hat{y}[r_{\theta\theta} \sin \theta \sin \phi + 2r_{\theta} \cos \theta \sin \phi - r \sin \theta \sin \phi] \\ + \hat{z}[r_{\theta\theta} \cos \theta - 2r_{\theta} \sin \theta - r \cos \theta]$$

$$(122) \quad \bar{r}_{\theta\phi} = -\hat{x} r \cos \theta \sin \phi + \hat{y} r \cos \theta \cos \phi$$

$$(123) \quad \bar{r}_{\phi\phi} = -\hat{x} r \sin \theta \cos \phi - \hat{y} r \sin \theta \sin \phi$$

where

$$r_{\theta\theta} = - \frac{r_{\theta}[(S_1)_{\theta} + S_2] + r(S_2)_{\theta}}{S_1}$$

$$(S_2)_{\theta} = r_{\theta}U_{\theta} + rU_{\theta\theta} + V_{\theta\theta}$$

Performing the operations indicated in Eq. (120) we have, after reduction

$$(124) \quad e = \frac{S_1 r_{\theta\theta} + 2S_2 r_{\theta} - S_1 r}{[S_1^2 + S_2^2]^{\frac{1}{2}}}$$

$$f = 0$$

$$g = - \frac{S_1 r \sin^2 \theta + S_2 r \sin \theta \cos \theta}{[S_1^2 + S_2^2]^{\frac{1}{2}}}$$

Now the normal curvature may be written as [41]

$$(125) \quad K_n = \frac{e du^2 + 2f du dv + g dv^2}{E du^2 + 2F du dv + G dv^2}$$



which in our case reduces to

$$(126) \quad K_n = \frac{e d\theta^2 + g d\phi^2}{E d\theta^2 + G d\phi^2} .$$

Now the curvatures in the directions of the coordinates may be found by taking  $d\theta$  and  $d\phi$  equal to zero respectively.

$$(127) \quad K_1 = e/E$$

$$K_2 = g/G .$$

The curvatures  $K_1$  and  $K_2$  are called the principal curvatures. The total curvature along a tangent to a coordinate direction can be expressed by introducing the angle  $\alpha$  between the direction  $d\phi/d\theta$  and the curvature direction  $d\phi = 0$ , resulting in

$$(128) \quad K = K_1 \cos^2\alpha + K_2 \sin^2\alpha .$$

This relation which expresses the normal curvature in an arbitrary direction in terms of the principal curvatures is known as Euler's Theorem.

Two further expressions are useful. These are expressions for the Mean and Gaussian curvatures and are

$$(129) \quad M = \frac{Eg - 2fF + eG}{2(EG - F^2)}, \text{ the mean curvature}$$

and

$$(130) \quad K = \frac{eg - f^2}{EG - F^2}, \text{ the Gaussian curvature.}$$

As the radius of curvature in a given direction is the reciprocal of the curvature the above results yield the radii of curvature required in the evaluation of the diffraction and attenuation coefficients.

The above results allow the determination of the radii of curvature, differential arc length, and Gaussian curvature at any point on a surface of revolution defined by Eq. (104). These surfaces include the figures of revolution derived from the conic sections and the ogive.

APPENDIX II  
DIFFRACTION BY A PERFECTLY  
CONDUCTING WEDGE

In order to satisfactorily calculate diffracted rays it is necessary to determine the diffraction of plane and cylindrical waves by a wedge. This has previously been done ( see Reference 26) and an expanded treatment is presented here. Sommerfeld[ 49] obtained the solution for a perfectly conducting wedge composed of two half-planes with a plane wave incident on the wedge. Sommerfeld also obtained an explicit form of the solution for zero wedge angle; i. e. , a half-plane. Pauli[ 5] determined an explicit form for the general wedge. Oberhettinger[ 13] presents a different form for the general wedge which he obtained using Green's function techniques.

The diffraction of a cylindrical wave by a wedge is obtained by the use of reciprocity, together with Pauli's expressions for wedge diffraction. Pauli's expressions give the diffraction of a plane wave by a wedge for a general angle of incidence and for polarization either perpendicular or parallel to the edge of the wedge. The total field at observation point P of cylindrical co-ordinates  $(r, \psi)$ , as shown in Fig. 50a, is given by

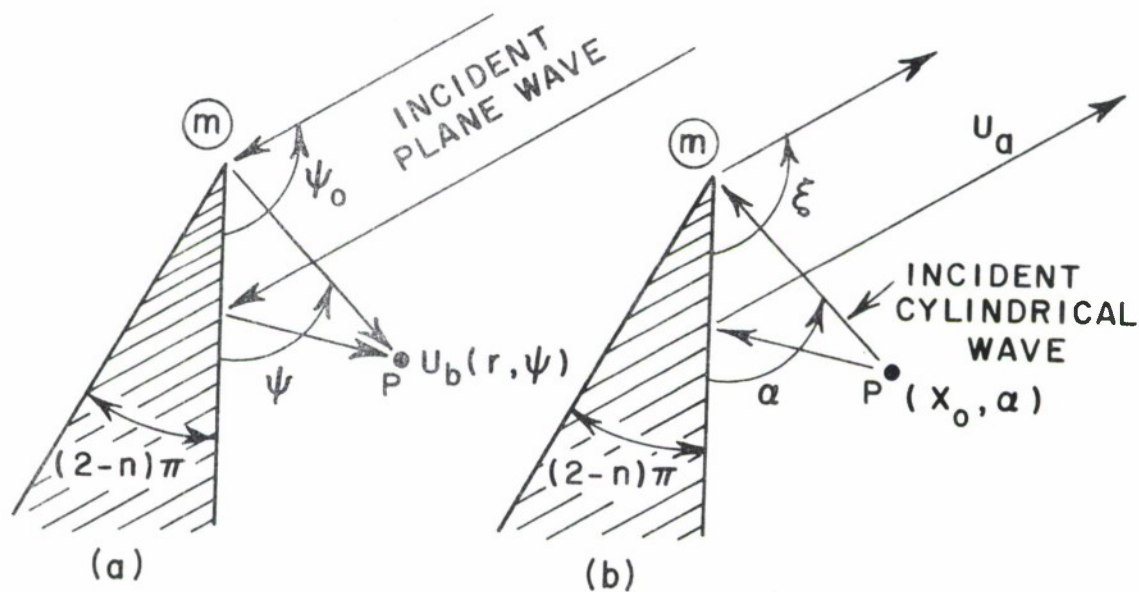


Fig. 50-- Diffraction by a wedge of included angle  $(2-n)\pi$ .

$$(131) \quad u(r, n, \psi) = v(r, n, \psi - \psi_0) \pm v(r, n, \psi + \psi_0)$$

for a plane wave incident from direction  $\psi_0$ . The plus sign applies for the polarization of the electric field perpendicular to the edge

$$\left( \frac{\partial u}{\partial n} \Big|_{\text{wedge}} \right) = 0 \quad ;$$

and the minus sign applies for polarization parallel to the edge

$(u|_{\text{wedge}}) = 0$ . The quantities  $v(r, \phi)$  are given by

$$(132) \quad v(r, n; \phi) = v^*(r, n, \phi) + v_B(r, n, \phi) ,$$

where  $v^*(r, n, \phi)$  is the geometrical optics field; and is given by

$$(133) \quad v^*(r, n, \phi) = \begin{cases} \exp[jkr \cos(\phi + 2\pi nN)] , & -\pi + 2\pi nN < \phi < \pi + 2\pi nN \\ 0 & \text{otherwise} \end{cases} ,$$

where

$$N = 0, \pm 1, \pm 2, \dots$$

$v_B(r, n, \phi)$  is the diffracted field for a wedge of angle  $(2-n)\pi$

and is given by

$$(134) \quad v_B(r, n, \phi) = \frac{2e^{j\frac{\pi}{4}}}{\sqrt{\pi}} \left( \frac{1}{n} \sin \frac{\pi}{n} \right) \frac{\left| \cos \frac{\phi}{2} \right|}{\cos \frac{\pi}{n} - \cos \frac{\phi}{n}} \\ \cdot e^{jkr \cos \phi} \int_{\sqrt{akr}}^{\infty} e^{-j\tau^2} d\tau \\ + \dots ,$$

where  $a = 1 + \cos \phi$ .

Equation (134) is composed of a leading term plus higher-order terms which are negligible for large values of  $kr$ . For large values of  $(akr)$  Eq. (134) becomes,

$$(135) \quad v_B(r, n, \phi) = \frac{e^{-j(kr + \pi/4)}}{\sqrt{2\pi kr}} \frac{\frac{1}{n} \sin \frac{\pi}{n}}{\cos \frac{\pi}{n} - \cos \frac{\phi}{n}} + \dots$$

The diffracted field, as expressed by Eq. (135), is that from which the asymptotic diffraction coefficients of the geometrical theory of diffraction are obtained[1]. Since this expression is valid only for large values of  $(akr)$ , it is not valid on the shadow boundary because  $a = 0$  there. Then Eq. (134) must be used, which gives the value of the diffracted field on the shadow boundary as

$$(136) \quad v_B(r, n, \pi) = \mp \frac{1}{2} e^{-jkr} + \dots \quad \left\{ \begin{array}{l} \text{upper sign for } \phi = \pi^- \\ \text{lower sign for } \phi = \pi^+ \end{array} \right. .$$

The value of  $v(r, \phi)$  on the shadow boundary can then be obtained from Eqs. (132), (133), and (136) as

$$(137) \quad v(r, n, \pi) = \frac{1}{2} e^{-jkr} + \dots ,$$

which is one-half of the incident field on the illuminated side of the shadow boundary.

The series representation of  $v_B$  given in Eq. (134) is valid everywhere except for the values

$$(138) \quad \phi = \pm \pi + 2\pi nN, \quad n \neq 2, \quad N = \pm 1, \pm 2, \dots .$$

Near these values the series representation converges slowly, and the periodicity property of the exact function  $v(r, n, \phi)$  can be used to overcome convergence difficulties near these values. The exact function  $v(r, n, \phi)$  is periodic in  $2\pi n$  so that

$$(139) \quad v(r, n, \phi + 2\pi nN) = v(r, n, \phi), \quad N = 0, \pm 1, \pm 2, \dots$$

Therefore, if the series representation of  $v_B$  converges slowly because  $\phi$  is near one of the values expressed by  $N \neq 0$  in Eq. (138), the periodicity property of Eq. (139) can be used to represent  $v(r, \phi)$  by employing the series representation near  $\phi = \pm \pi(N = 0)$ . The only case for which all boundaries are regular and the substitution of Eq. (139) is not necessary is for the thin half-plane, in which case  $n = 2$ .

We now examine the behavior of the diffraction coefficient  $v_B(r, n, \phi)$  for the case illustrated in Fig. 51 in which two reflected rays exist at angles  $\psi_1$  and  $\psi_2$ . We first examine the values of  $\phi = \psi + \psi_0$  for the diffracted rays corresponding to the directions of these reflected rays. The values of the pertinent angles are

$$(140) \quad \psi_1 = \pi - \psi_0, \quad \psi_2 = (2n\pi - \pi) - \psi_0$$

Thus the values of  $\phi = \psi + \psi_0$  are

$$(141) \quad \phi_1 = \pi, \quad \phi_2 = (2n\pi - \pi)$$

For  $\phi_1 = \pi$  Eq. (136) expresses the value of the diffraction coefficient and thus the total field at  $\psi = \psi_1$  is one-half the geometrical optics reflected field on the illuminated side of the shadow boundary, as given by Eq. (137).

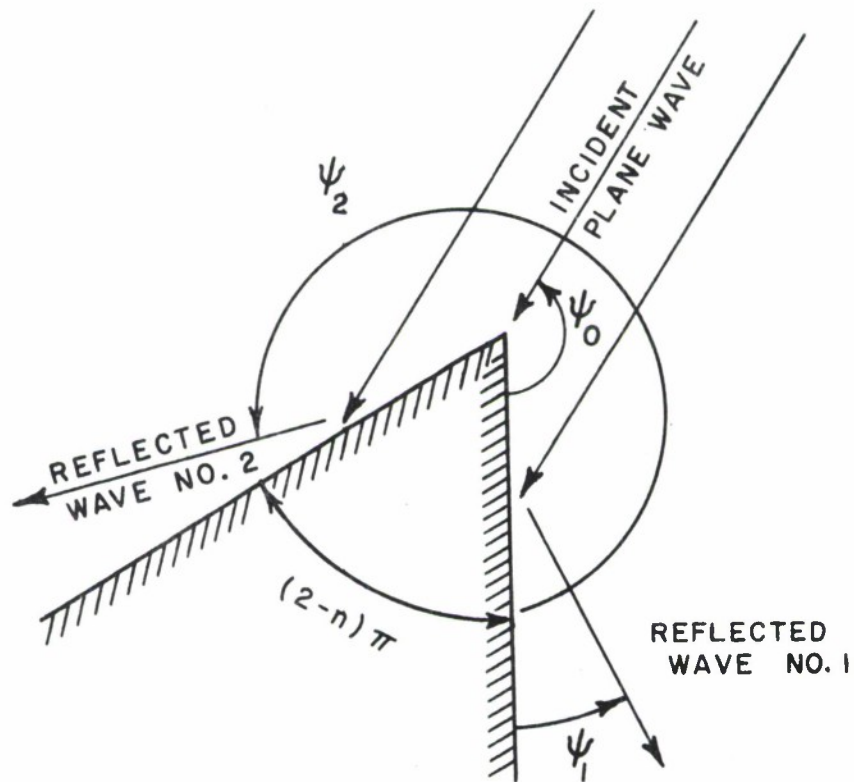


Fig. 51--Case of diffraction by a wedge where two reflected rays exist.

However, for  $\phi_2 = 2n\pi - \pi$  and  $n \neq 2$ , Eq. (134) is not analytic and consequently the following substitution is made:

$$(142) \quad v(r, n, \phi) \rightarrow v(r, n, \phi - 2\pi n)$$

for values of

$$(143) \quad \phi > \pi n .$$



The region over which the substitution of Eq. (142) is made, as expressed by Eq. (143) is determined from the symmetry property of  $v(r, n, \phi)$ ; i. e. ,

$$(144) \quad v(r, n, -\phi) = v(r, n, +\phi) \quad .$$

That is, if the substitution of Eq. (142) is made for values of  $\phi < \pi n$ , then the substituted values of  $\phi - 2\pi n$  are closer to the value of non-analyticity  $\pi - 2n\pi$  than the original values of  $\phi$  were to the value of nonanalyticity  $2n\pi - \pi$ . It is also noted that the value substituted for  $v(r, n, \phi_2)$  is  $v(r, n, -\pi)$ , which corresponds to the correct value for a shadow boundary.

The equations given in this Appendix apply for plane-wave incidence, but they can be used for cylindrical-wave incidence as shown below. Consider the two situations shown in Fig. 50. It is desired to find the field  $u_a$  in some direction  $\xi$  for the wedge illuminated by a cylindrical wave with its source located at  $(x_0, \alpha)$ . By reciprocity, the field  $u_a$  is equal to the field  $u_b$  which is located at the point  $(r = x_0, \psi = \alpha)$  and with a plane wave incident from the direction  $\psi_0 = \xi$ . The value of  $u_b$  is given by Eq. (134). Thus using the property expressed in Eq. (131) the solution for diffraction of a cylindrical wave by a wedge becomes

$$(145) \quad u_a = v(x_0, n, \xi + \alpha) \pm v(x_0, n, \xi - \alpha) \quad .$$

The field at infinity is given by Eq. (145) for a perfectly conducting wedge illuminated by a line source at  $(x_0, \alpha)$ .

If the quantity  $(akx_0)$  is sufficiently large for Eq. (135) to be valid, then the diffraction pattern for cylindrical-wave incidence has the same form as that for plane-wave incidence. In other words, the diffraction for cylindrical-wave incidence is the same as that for plane-wave incidence in regions sufficiently removed from the shadow boundaries. The region near the shadow boundary in which Eq. (134) must be used increases for decreasing values of  $x_0$  and may encompass all 360 degrees.

Hutchins [50] has generalized the Pauli solution presented above and has obtained a series solution which is valid for the exterior and interior regions of a wedge. In addition his solution is accurate for wedges of large included angles where the Pauli solution is not accurate.

APPENDIX III  
 APPROXIMATION FOR THE SPECULAR SCATTERING  
 BY A GENERATOR OF A CONE

Specular scattering by a generator or frustrum of a cone is shown in Fig. 52. An approximate solution for the backscattered field

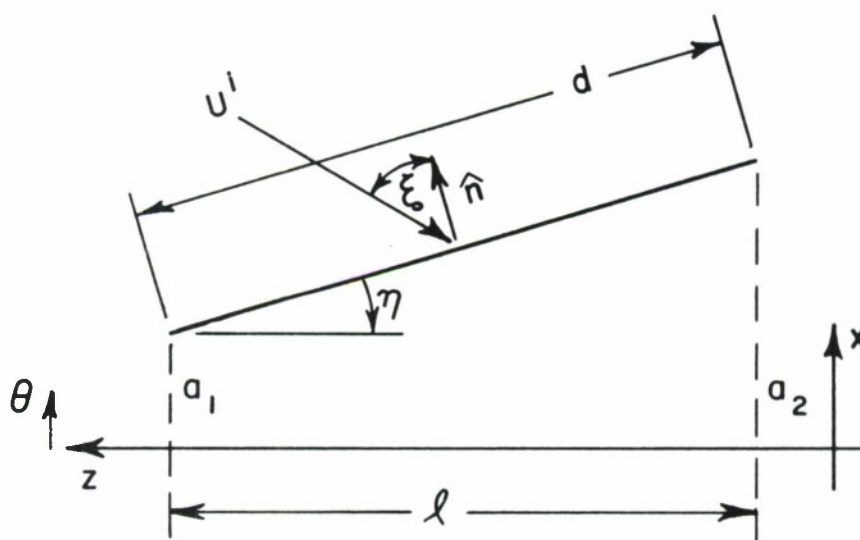


Fig. 52--Scattering by a conical frustrum.

in and near the specular direction may be constructed as follows. It is assumed that the backscattered field close to the normal to the cone can be written as

$$(146) \quad U^S(\xi) = + \frac{kd}{\sqrt{2\pi k}} F(r) \frac{\sin(kd \sin(\xi))}{kd \sin(\xi)} \frac{e^{-jkr}}{r} \cdot U^i.$$

Equation (146) combines the  $\sin(x)/x$  pattern function behavior previously discussed and the spatial attenuation factor  $F(r)$ . Proceeding from Fig. 52 we have that

$$(147) \quad \rho_1 = a_1 / \cos \eta$$

$$(148) \quad \rho_2 = a_2 / \cos \eta$$

where  $\rho_1$  and  $\rho_2$  are the finite radii of curvature at the ends of the frustrum.

$$(149) \quad F(r) \Big|_{\xi=0} = \sqrt{\frac{\rho}{2}}$$

where

$$(150) \quad \rho = \rho_1 + \frac{z}{l} (\rho_2 - \rho_1).$$

The average spatial attenuation for  $\xi$  small is approximated as

$$(151) \quad F(r)_{ave} = \frac{1}{l} \int_0^d \sqrt{\frac{\rho_1 + \frac{z}{l} (\rho_2 - \rho_1)}{2}} dz$$

with the result

$$(152) \quad F(r)_{ave} = \frac{\sqrt{2}}{3} \frac{1}{\rho_2 - \rho_1} [\rho_2^{3/2} - \rho_1^{3/2}] x.$$

The approximate scattered field from the generator of the cone is then

$$(153) \quad U_{app}^S(\xi) = + \frac{kd}{\sqrt{2\pi k}} F(r)_{ave} \frac{\sin(kd \sin \xi)}{kd \sin \xi} \frac{e^{-jkr}}{r} \cdot U^i.$$

APPENDIX IV  
THE DETERMINATION OF THE GEODESIC PATHS  
ON A GENERAL QUADRIC OF REVOLUTION

The determination of the geodesic paths on a general quadric surface of revolution is not an easy task in general. It is known that the geodesic paths on a body of revolution can be found by quadratures. However, in the case studied here it is convenient to utilize the differential equation for the geodesic given by Struik[ 48] as

$$(154) \quad v'' = A(v')^3 + B(v')^2 + cv' + D$$

where  $A = -\frac{G\theta}{2E}$

$$B = \frac{E\theta}{E} - \frac{G\theta}{2G}$$

$$C = \frac{E\theta}{2E} - \frac{G\theta}{G}$$

$$D = \frac{E\theta}{2G}$$

$$V = \phi(\theta)$$

and where E and G are given by Eq. (118) and  $E_\theta$  and  $G_\theta$  are the partial derivatives with respect to  $\theta$ .

We now assume a Taylor series solution for  $v = \phi$  in the form

$$(155) \quad \phi(\theta_{i+1}) = \phi(\theta_i) + \Delta\theta \left( \frac{d\phi}{d\theta} \right)_{\theta_i} + \left( \frac{\Delta\theta}{2} \right)^2 \left( \frac{d^2\phi}{d\theta^2} \right)_{\theta_i}$$

$$\Delta\theta = | \theta_{i+1} - \theta_i | .$$

The differential equation is then

$$(156) \quad \frac{d^2\phi}{d\theta^2} = A \left( \frac{d\phi}{d\theta} \right)^3 + B \left( \frac{d\phi}{d\theta} \right)^2 + C \frac{d\phi}{d\theta} + D .$$

And the following procedure will yield a numerical solution by iteration:

1. Determine  $d\phi/d\theta \big|_{\theta_i}$
2. Compute A, B, C, D, at  $\theta_i, \phi_i$
3. Compute  $d^2\phi/d\theta^2 \big|_{(\theta_i, \phi_i)}$
4. Compute  $\phi(\theta_{i+1})$  using the series
5. Compute  $d\phi/d\theta = (\phi_{i+1} - \phi_i) / \Delta\theta$
6.  $i = i+1$  and proceed.

APPENDIX V  
THE COMPUTER SOLUTION FOR BACKSCATTER  
BY A SECTIONALLY CONTINUOUS BODY OF  
REVOLUTION DESCRIBED BY A SECOND  
DEGREE EQUATION

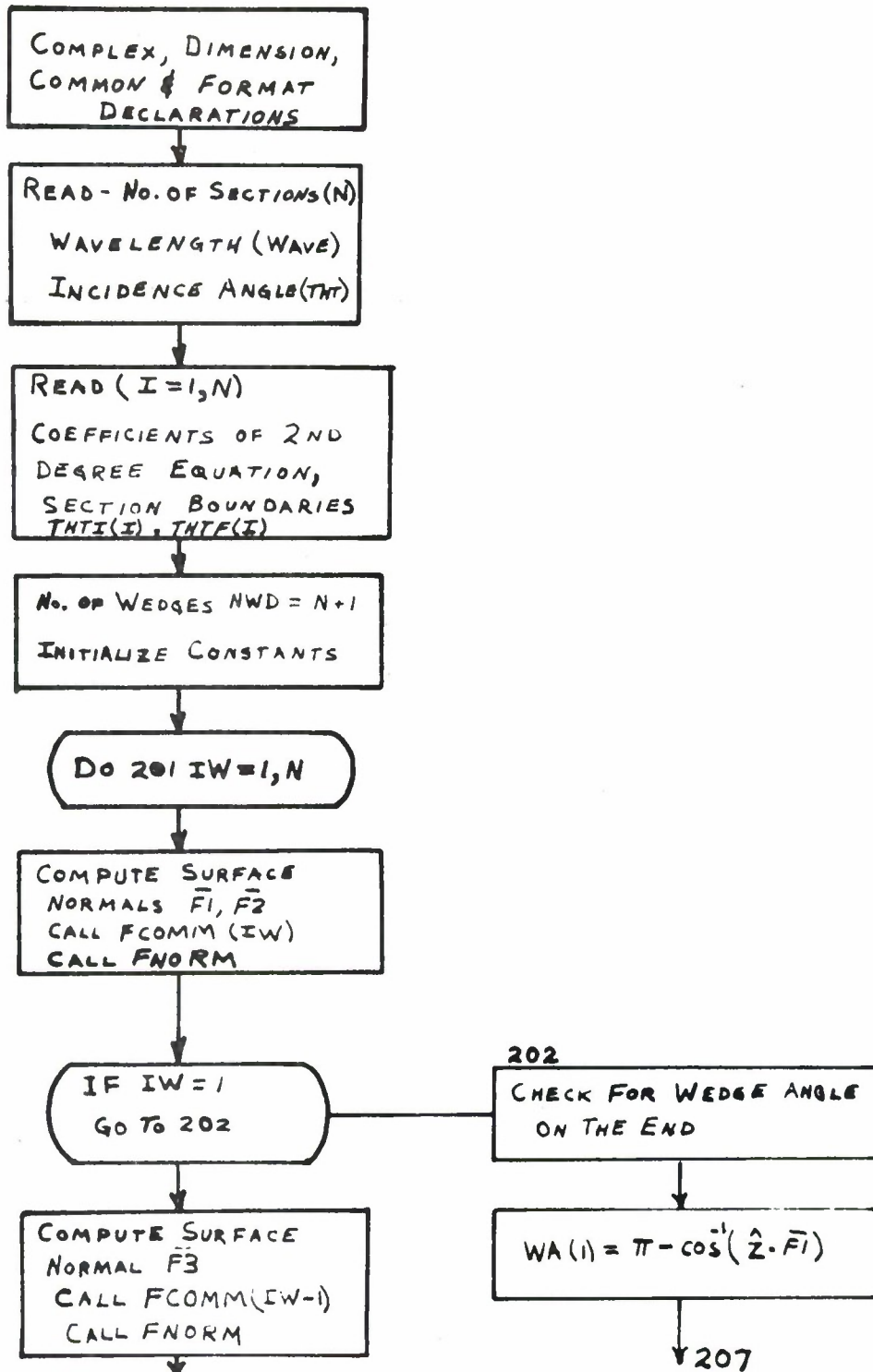
In the computer solution Eq. (104) is used to describe the profile of the target within a section defined by the angles  $THTI(I)$  and  $THTF(I)$ . The constants must be arranged so that Eq. (110) generates an outward normal to the surface. The angle of the incident wave is  $THT$  and the wavelength is  $WAVE$ . The following flow diagrams describe the computer programs which were coded in Fortran IV for the solution of the backscattered fields of the target. A list of the Subroutines and Functions, other than standard library routines which were used is also presented.

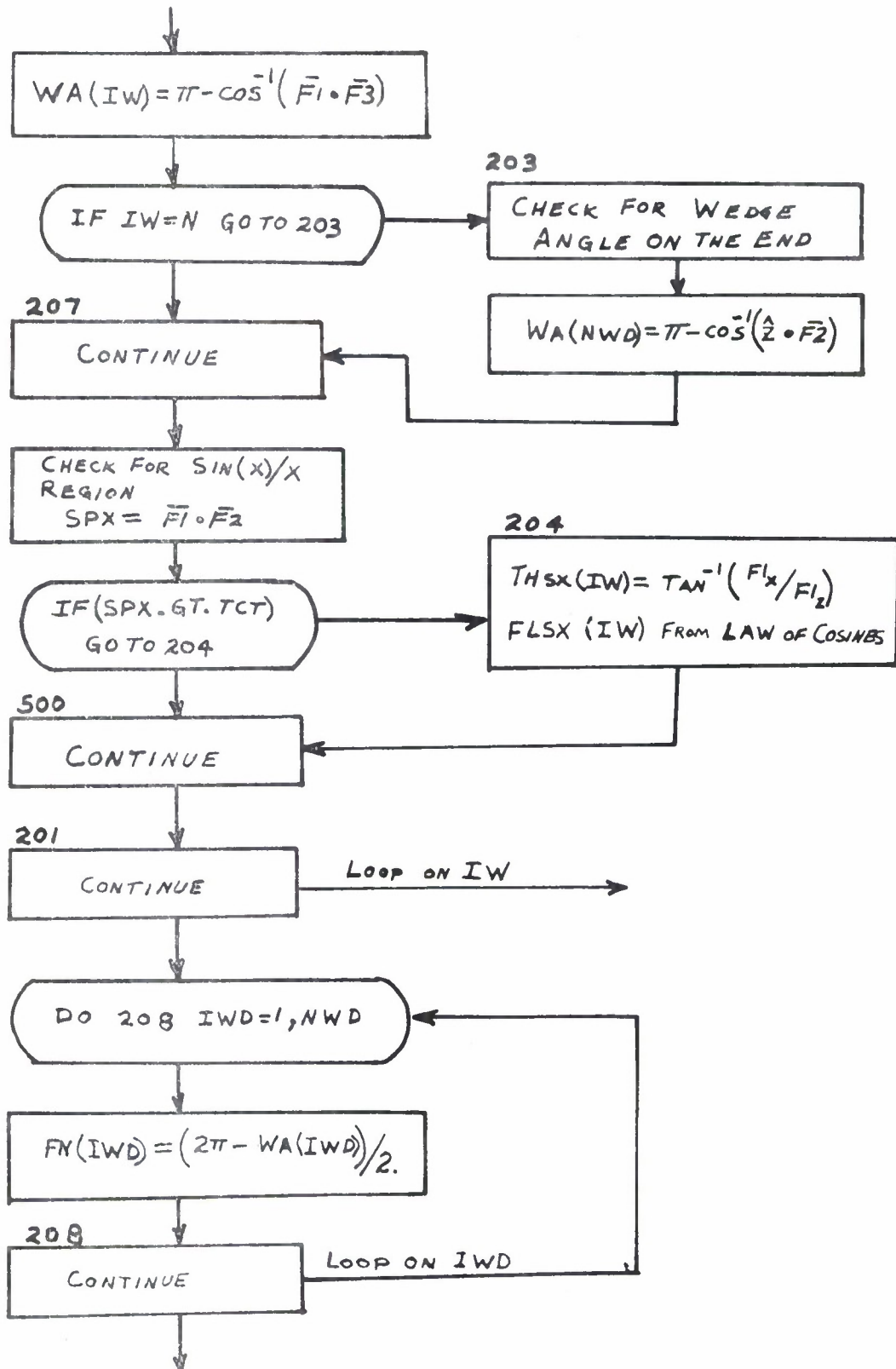
The programs, titled "Wedge Diffraction Computer Program" and "Creeping Wave Computer Program" utilize the analytic techniques presented previously. The Wedge Diffraction Computer Program uses the wedge diffraction coefficient, the diffraction by a pair of wedges, and the solution for the diffracted fields near the axis to construct the solution for the scattered fields due to single diffraction from locations on the target where the slope is discontinuous.

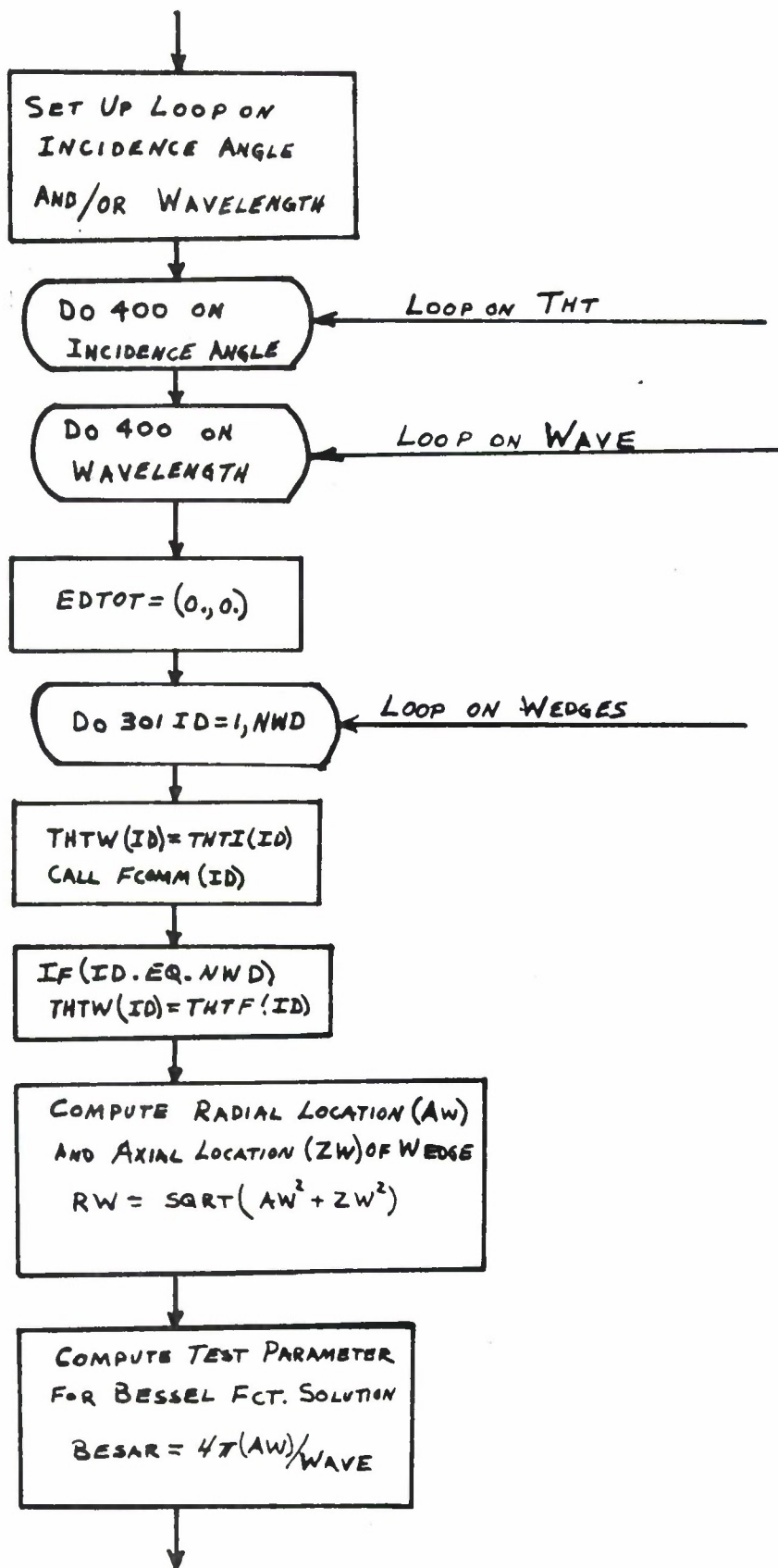
The creeping wave computer program uses the geometrical optics field from the specular point and the creeping wave solution for waves which propagate around the target to construct the solution for a target having no discontinuities in slope on its surface. The scattered fields for a target where both wedge diffraction and creeping wave contributions exist can be constructed using a combination of the results of both programs.

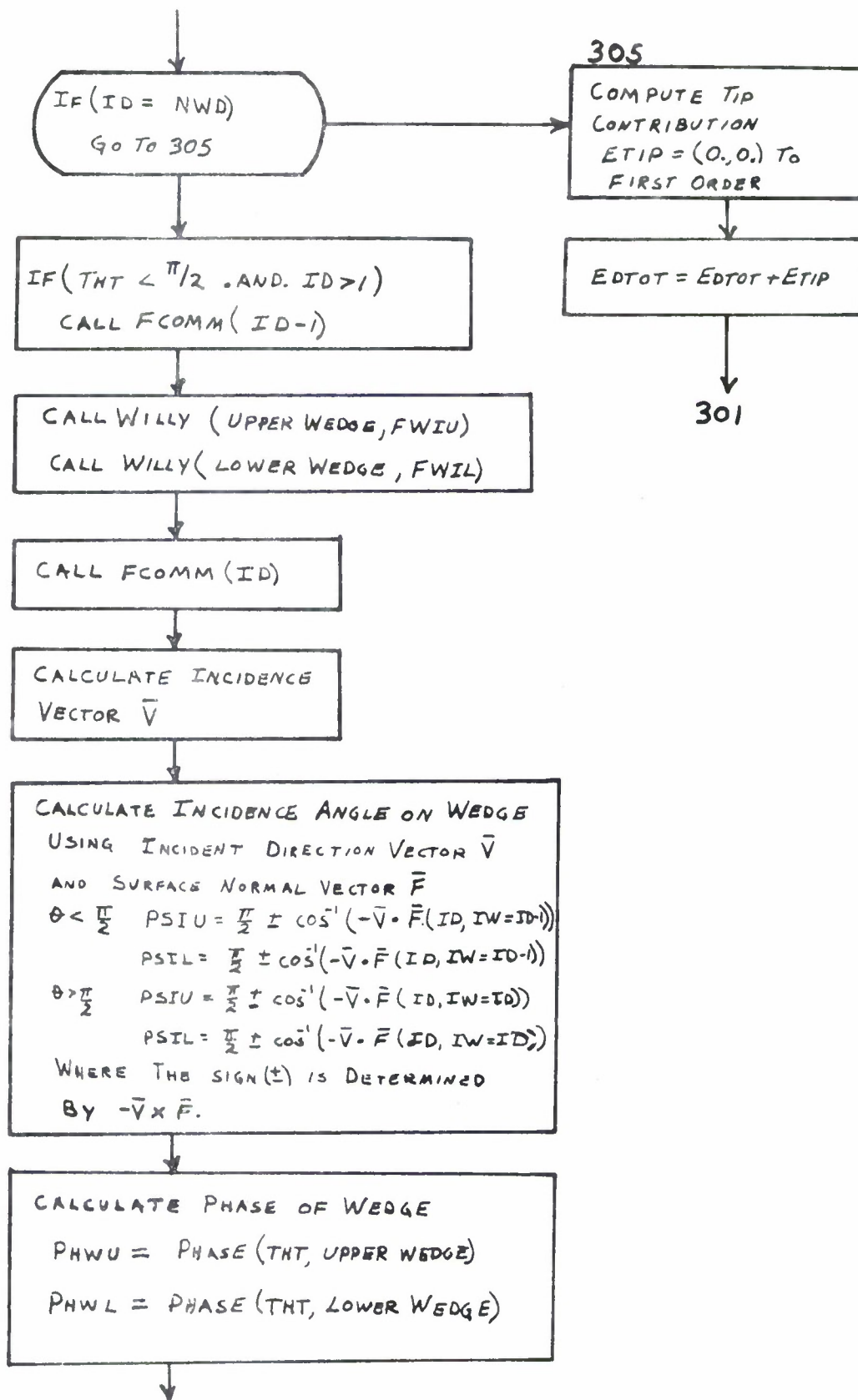


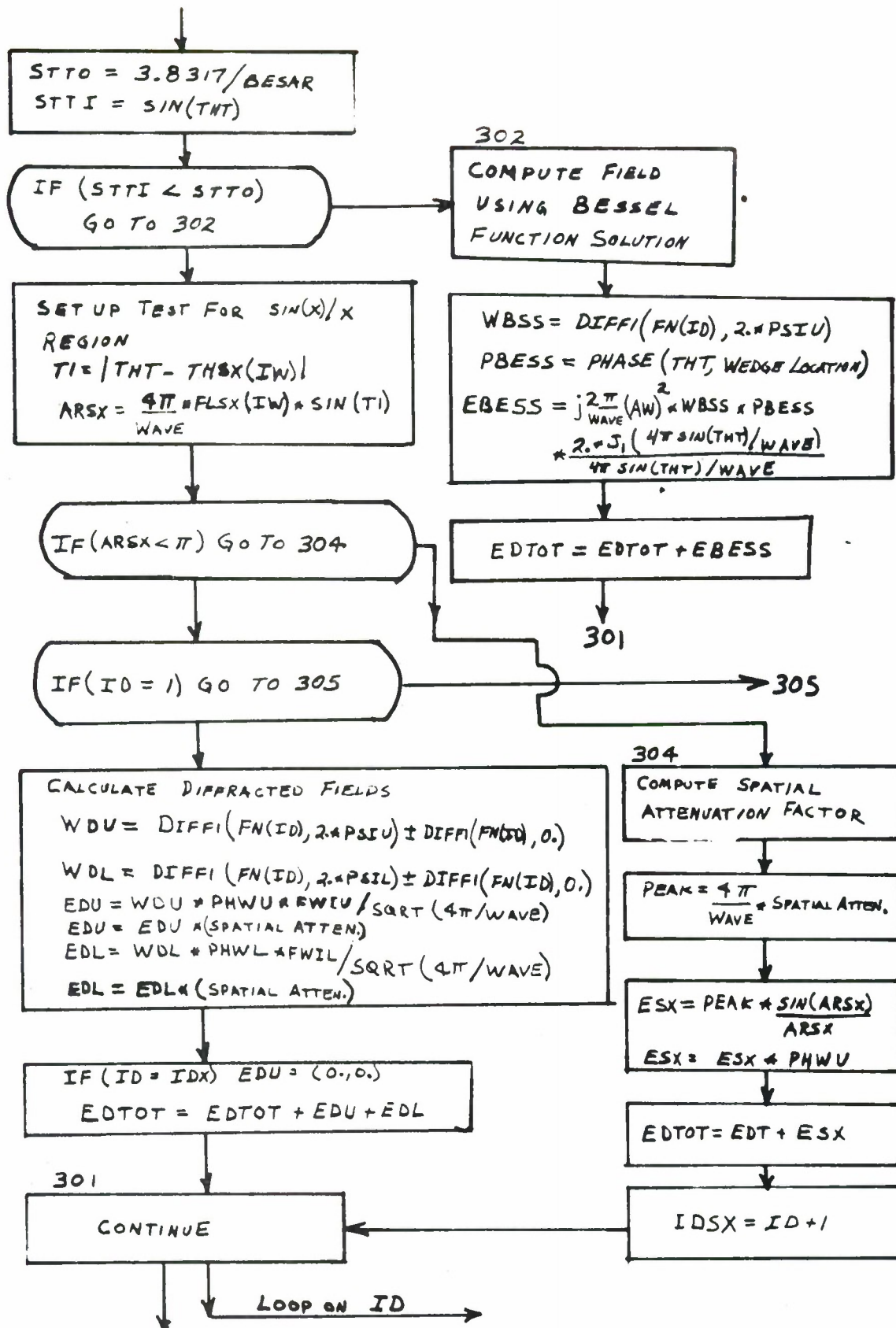
## WEDGE DIFFRACTION COMPUTER PROGRAM

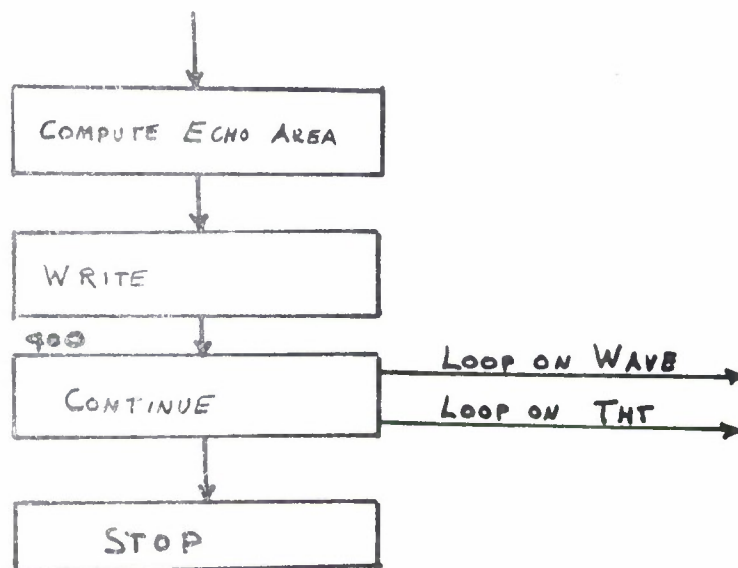






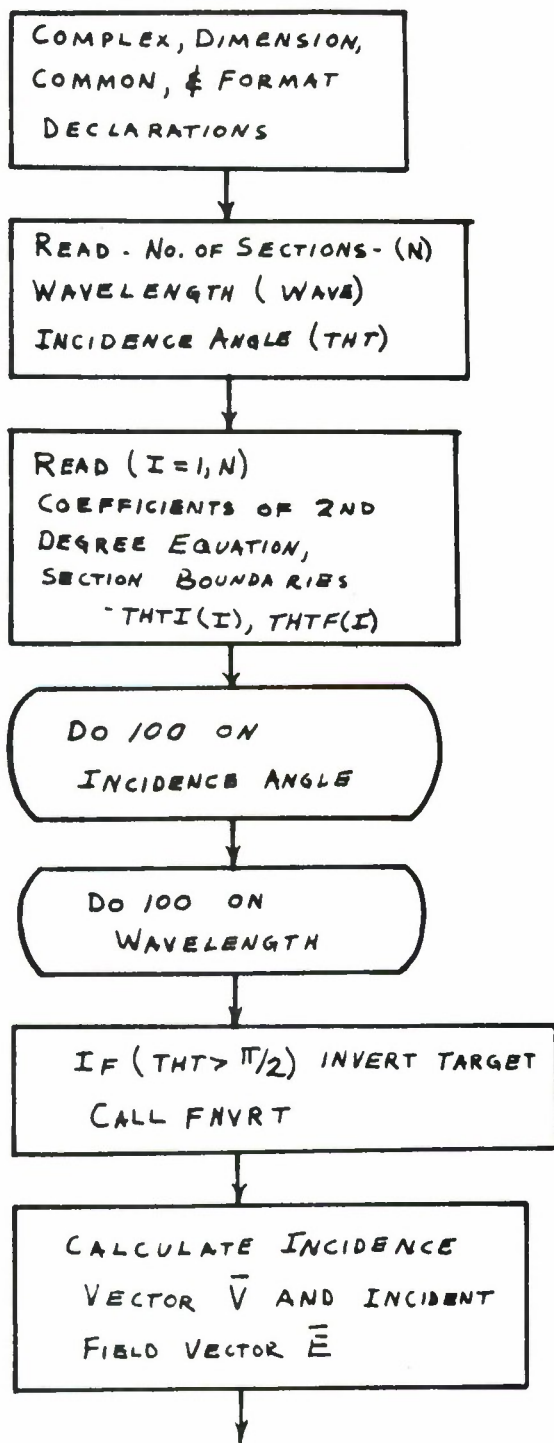


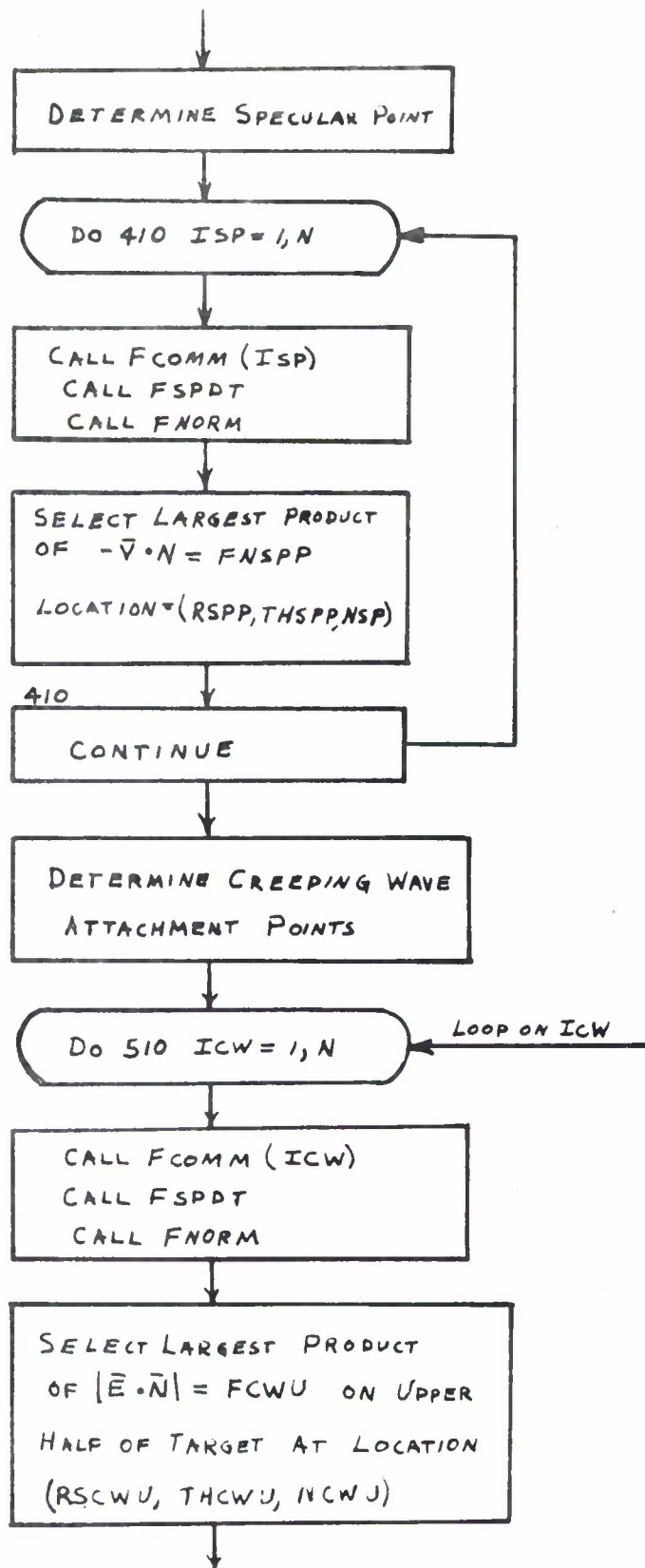




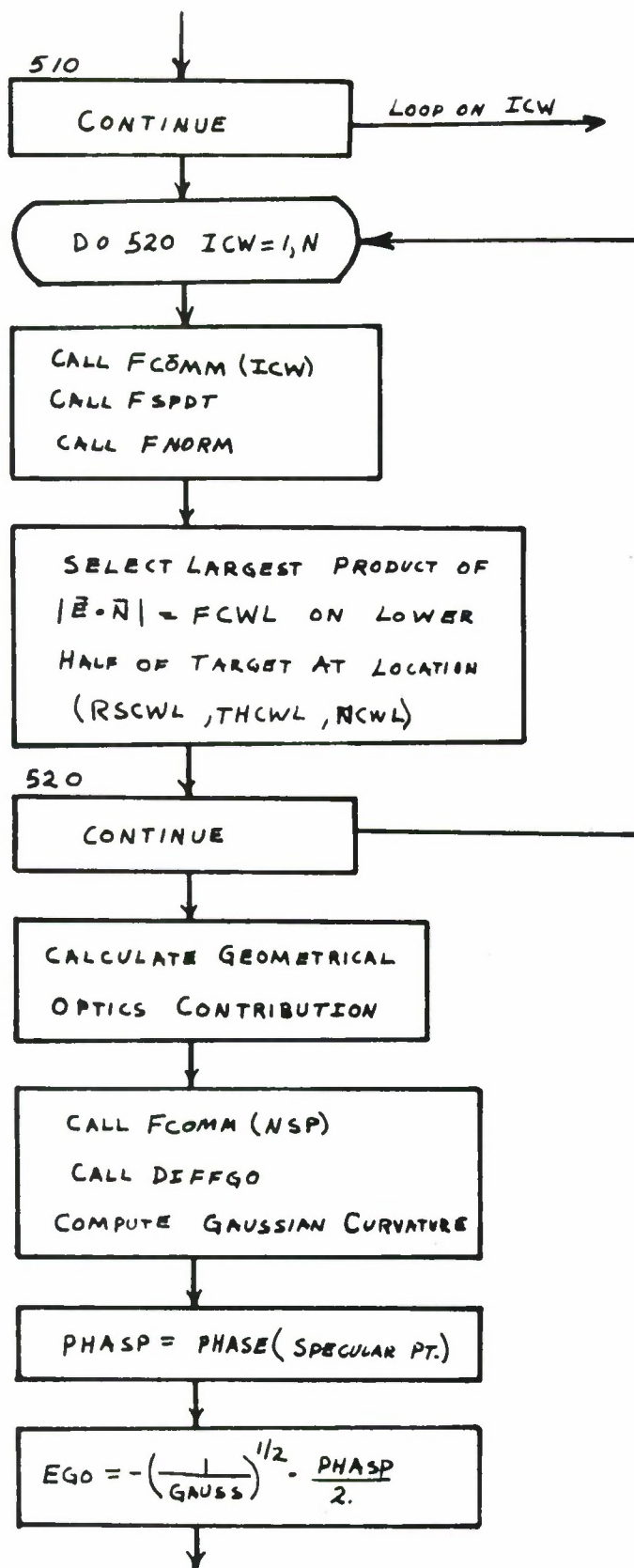
## CREEPING WAVE COMPUTER PROGRAM

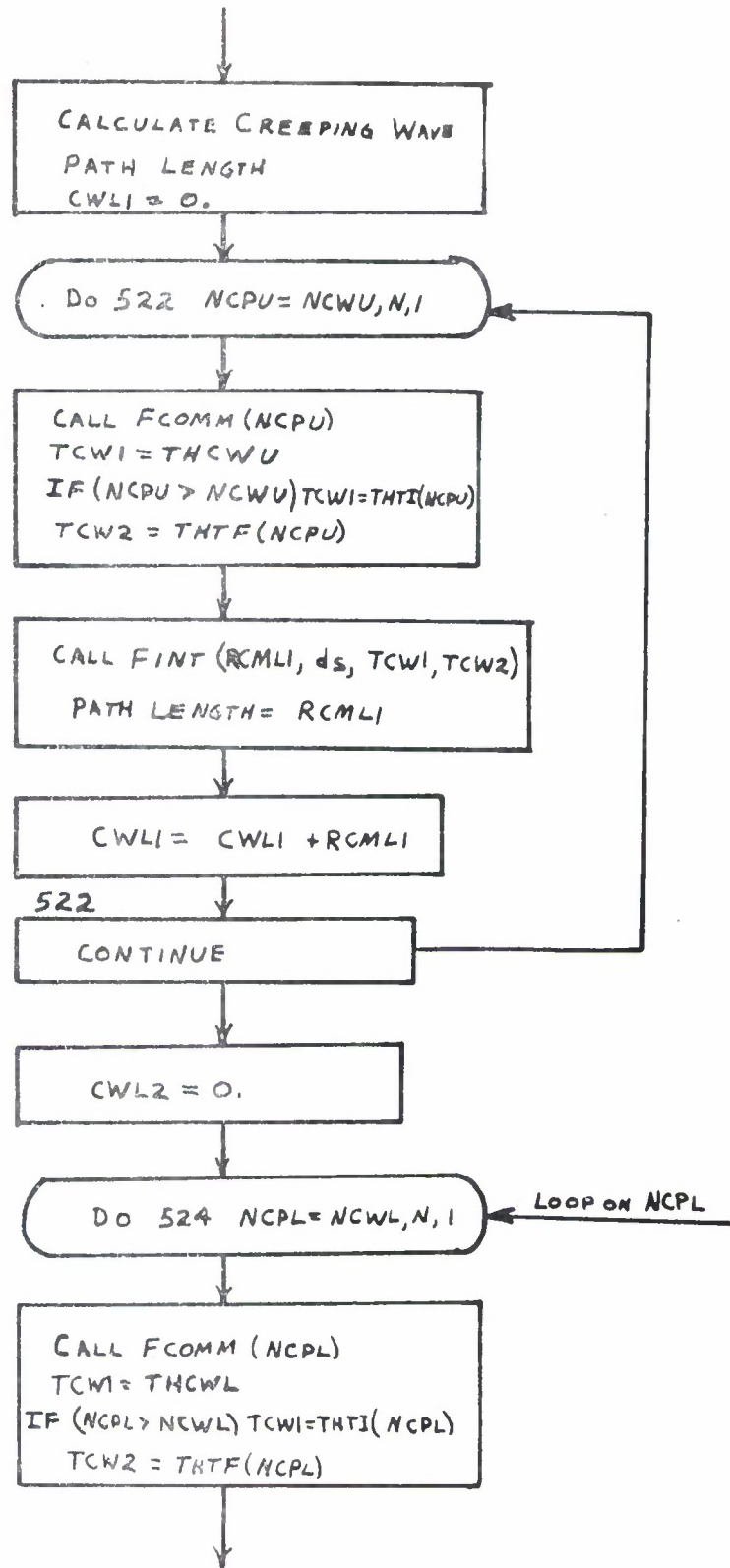
### HORIZONTAL POLARIZATION

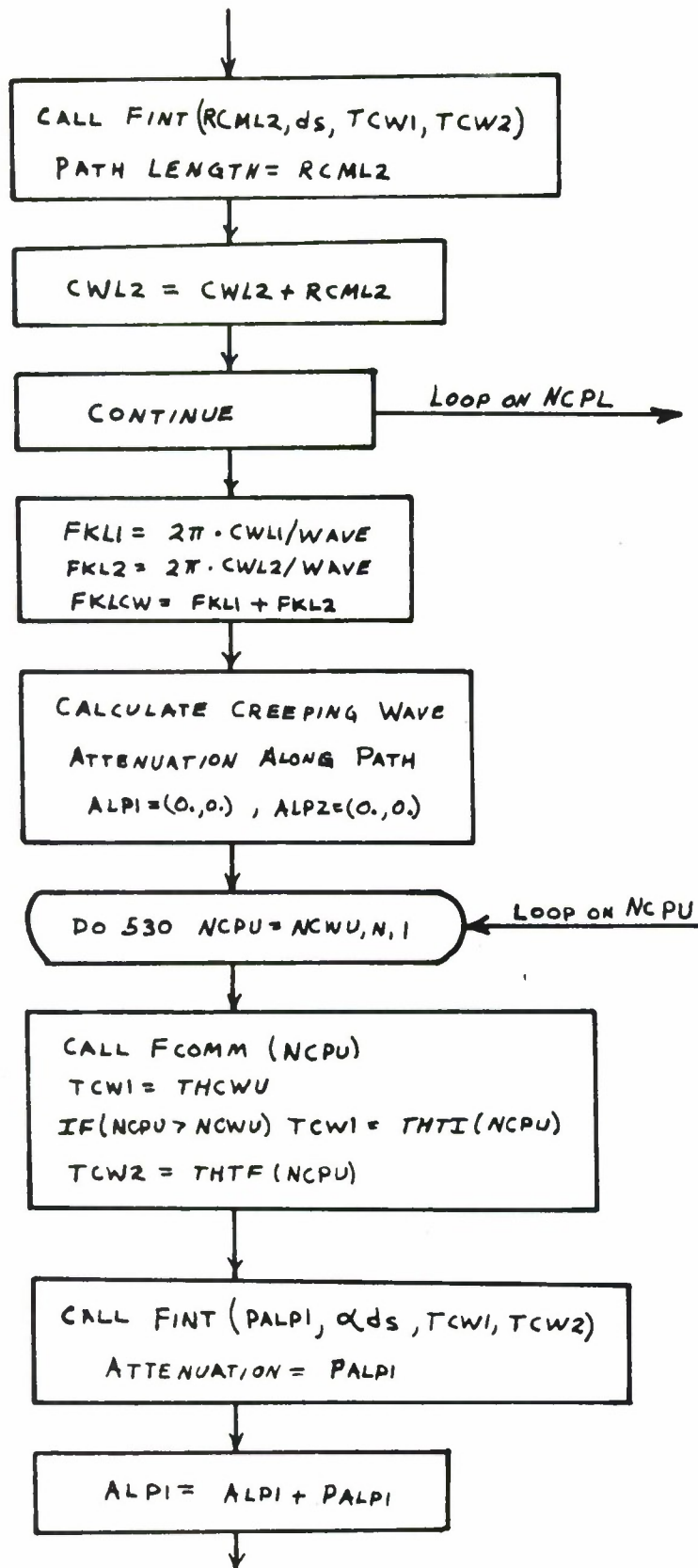


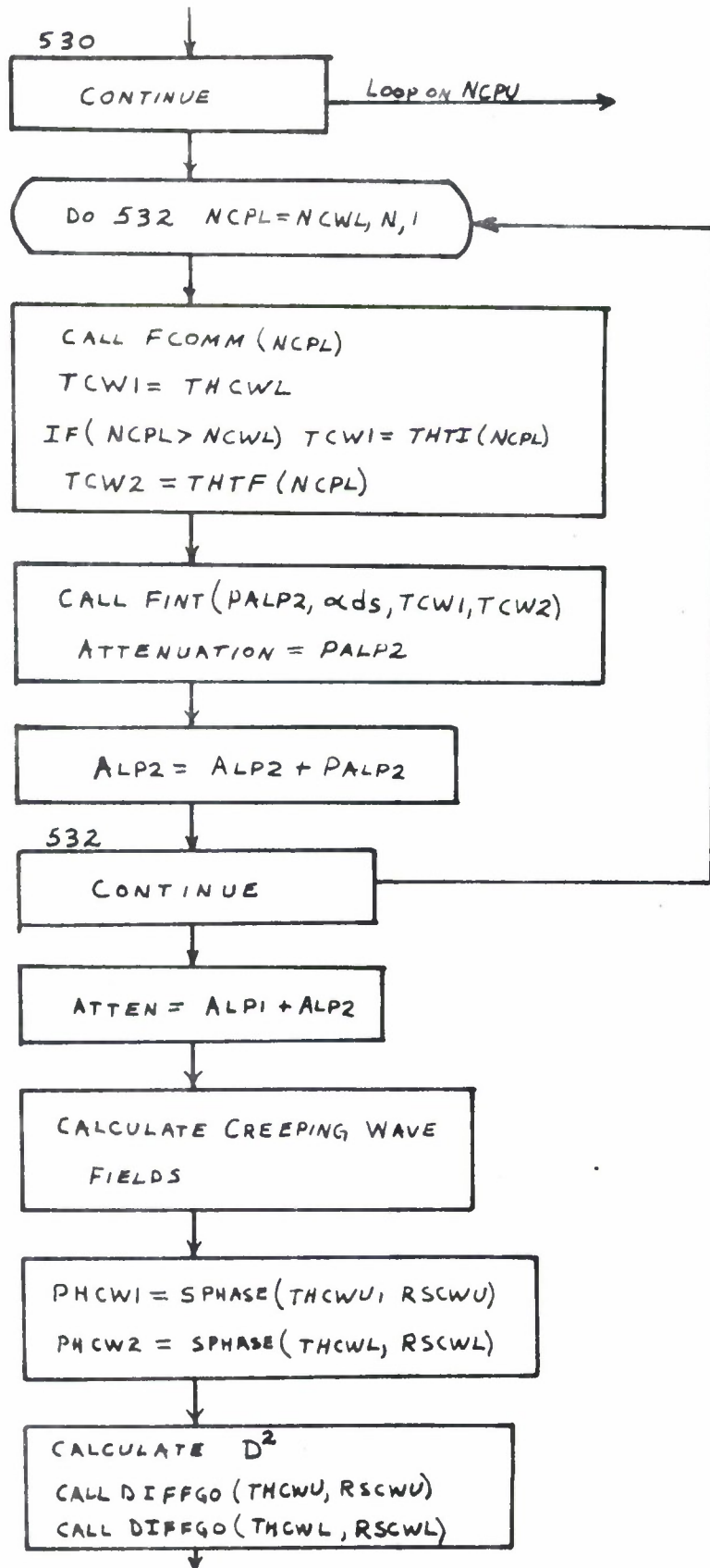


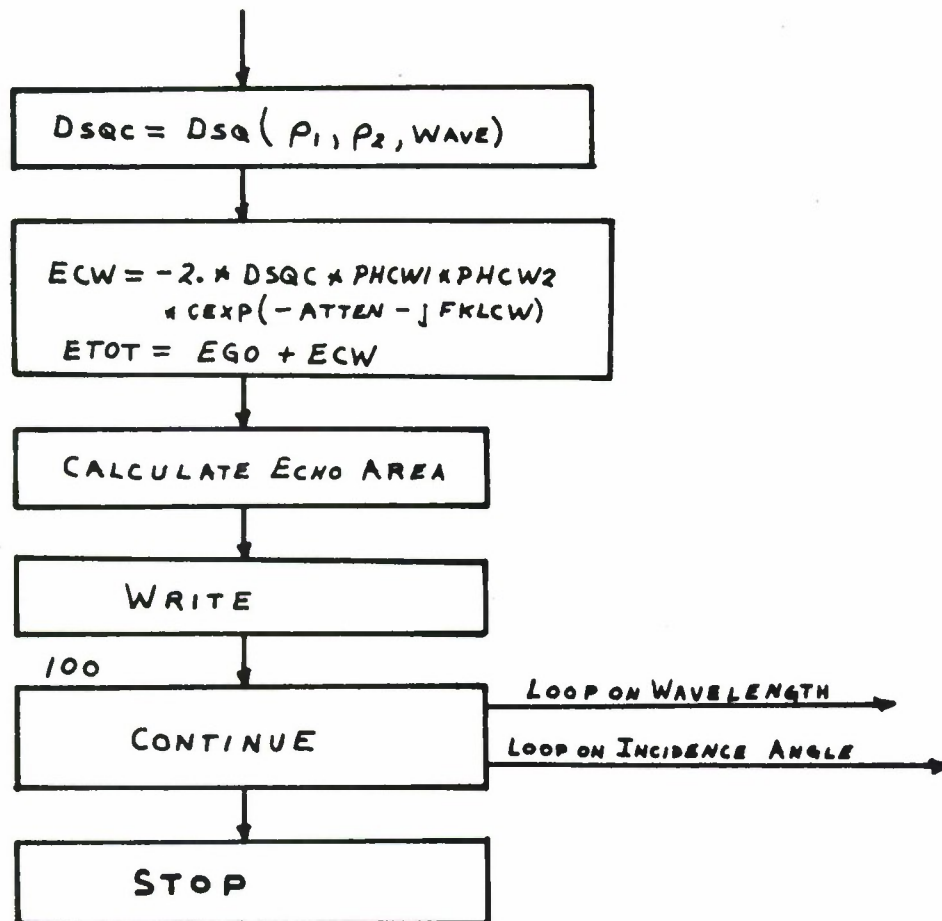












SUBROUTINES AND FUNCTIONS

FCOMM( I) Shifts constants describing each section from /DATA/  
COMMON to unlabeled COMMON, thus adjusting the constants  
to the current section ( I).

RAD( THT) Computes the radial distance to the surface at the angle  
THT.

FNORM( FNVX, FNVY, FNVZ, R, THT, PHI) Computes the surface  
normal  $\bar{N} = \hat{x}FNVX + \hat{y}FNVY + \hat{z}FNVZ$  at ( R, THT, PHI)

WILLY( FWI, THTI, PHI, THIN, PHIN) Indicates if the location  
( RAD( THTI), THTI, PHI) is illuminated ( FWI = 1.) or  
shadowed ( FWI=0.) with respect to the incident wave  
( THIN, PHIN).

CROSS( X, Y, Z, A1, A2, A3, B1, B2, B3) Computes  $\bar{X} = \bar{A} \times \bar{B}$ .

PHASE( THTI, PHII, THTB, RB, FK) Computes the backscattered  
phase of the location ( RB, THTB) for a wavenumber ( FK)  
and incident wave ( THTI, PHII).

SINXX( Y) Computes  $\sin ( Y) / Y$ .

DIFF1( FN, PHI, BETA) Computes 
$$DIFF1 = \frac{\sin ( \pi / FN)}{FN \cdot \sin( BETA)}$$
  
$$\cdot \frac{e^{-j\frac{\pi}{4}}}{\cos( \pi / FN) - \cos( PHI / FN)}$$

BESL1(X) Computes  $J_1(X)$ .

FSPDT(RSP, THSP, FNT, THTS, THTF, DTHT, PHI, VX, VY, VZ)

Increments by steps of DTHT within the limits THTS to THTF and finds the location (RSP, THSP) at which the scalar product  $FNT = \bar{N} \cdot \bar{V}$  is a maximum.

FINT(SSS, FCTI, FLL, FUL, ERRR, NX) Performs a numerical integration of the complex function FCTI between the limits FLL to FUL, within a percent error ERRR, returning the answer in SSS. If NX is 1 equal increments are used, if 2 adjusted increments are used.

DELSP(THT) Computes the incremental arc length at the angle THT.

SPHASE(THTI, PHII, THTB, RB, FK) Computes the incident phase of the location (RB, THTB) for a wavenumber (FK) and incident wave (THTI, PHII).

ALPH(RHO1, RHO2, WAVE) Computes the attenuation function (ALPH) for radii of curvature (RHO1, RHO2) and a wavelength (WAVE).

DSQ(RI1, RI2, WAVE) Computes the square of the diffraction coefficient (DSQ) for radii of curvature (RI1, RI2) and a wavelength (WAVE).

ALPHDS( THT)    Computes the product of the attenuation coefficient  
                  ( ALPH) and the incremental arc length ( DELSP) at the angle  
                  ( THT).

DIFFGO( R, THT, RTHT, RTTH, ECAP, FCAP, GCAP, ELC, FLC, GLC)

                  Computes the radial first ( RTHT) and second ( RTTH)  
                  derivatives of the surface and the differential geometry  
                  parameters ( ECAP, FCAP, GCAP, ELC, FLC, GLC) at a point  
                  on the surface ( R, THT).



## REFERENCES

1. Keller, J. B. , "Diffraction by an Aperture," *Journal of Applied Physics*, " 28, 4, April 1957, pp. 426-444.
2. Richmond, J.H. , "A Wire Grid Model for Scattering by Conducting Bodies," *IEEE Transactions on Antennas and Propagation*, Vol. AP-14, No. 6, November 1966, pp. 782-786.
3. Harrington, R. F. , "Theory of Loaded Scatterers," *Proc. of the Institute of Electrical Engineers*, Vol. 111, No. 4, April 1964, pp. 617-623.
4. Green, R. B. , "The General Theory of Antenna Scattering," Report 1223-17, 30 November 1963, ElectroScience Laboratory, The Ohio State University Research Foundation; prepared under Contract AF 33(616) -8039, Aeronautical Systems Division, Wright-Patterson Air Force Base, Ohio. AD 429 186
5. Pauli, W. , "On Asymptotic Series for Functions in the Theory of Diffraction of Light," *Physical Review*, 54, 1 December 1938.
6. Luneberg, R. K. , Mathematical Theory of Optics, University of California Press, Berkeley and Los Angeles, 1964.

7. Peters, L. , Jr. and Thomas, D. T. , "A Geometrical Optics Approach for the Radar Cross Section of Thin Shells," Journal of Geophysical Research, Vol. 67, No. 5, May 1962, pp. 2073-2075.
8. Kouyoumjian, R.G. , Peters, L. , Jr. , and Thomas, D. T. , "A Modified Geometrical Optics Method for the Scattering by Dielectric Bodies," IEEE Transactions on Antennas and Propagation, Vol. AP-11, November 1963, pp. 690-703.
9. Swarner, W. G. and Peters, L. , Jr. , "Radar Cross Sections of Dielectric on Plasma-Coated Conducting Bodies," IEEE Transactions on Antennas and Propagation, Vol. AP-11, September 1963, pp. 558-569.
10. Peters, L. , Jr. , Kawano, K. , and Swarner, W.G. , "Approximations for Dielectric or Plasma Scatterers," Proc. of IEEE, Vol. 53, No. 8, August 1965, p. 882.
11. Kay, L and Keller, J. B. , "Asymptotic Evaluation of the Field at a Caustic," J. Applied Physics, 25, 1954, 876.
12. Thomas, D. T. , "Scattering by Plasma and Dielectric Bodies," Report 1116-20, 1 August 1962, ElectroScience Laboratory, The Ohio State University Research Foundation; prepared under Contract AF 19( 604) -7270, Air Force Cambridge Research Laboratories, Bedford, Massachusetts. AD 286 854

13. Oberhettinger, F. , "On Asymptotic Series for Functions in the Theory of Diffraction of Waves by Wedges," Jour. Math. and Phys. , 34, 1955, pp. 245-255.
14. Nomura, Yukichi, "On the Complete Theory of Diffraction of Electric Waves by a Perfect Conducting Wedge," Reprinted from The Reports of the Research Institute of Electrical Communication, Tohoku University, Sci. Rep. RITU, B-(Elect. Comm. ), Vol. 14, No. 1, Sendai, Japan, December 1952.
15. Ryan, C. E. , Jr. and R. C. Rudduck, "Calculation of the Radiation Pattern of a General Parallel-Plate Waveguide Aperture for the TEM and  $TE_{01}$  Waveguide Modes," Report 1693-4, 10 September 1964, ElectroScience Laboratory, The Ohio State University Research Foundation; prepared under Contract N62269-2184, U. S. Naval Air Development Center, Johnsville, Pennsylvania.
16. Ryan, C. E. , Jr. and Rudduck, R. C. , "Calculation of the Far-Field Patterns of a Rectangular Waveguide," Report 1693-7, 20 November 1964, ElectroScience Laboratory, The Ohio State University Research Foundation; prepared under Contract N62269-2184, U. S. Naval Air Development Center, Johnsville, Pennsylvania. AD 462 764

17. Morse, P. M. and Feshbach, H. , Methods of Theoretical Physics, McGraw-Hill Book Co. , Inc. , New York, 1953, pp. 1069 and 1546.
18. Yu, J. S. and Rudduck, R. C. , "Diffraction by Conducting Walls of Finite Thickness," Report 1767-7, 15 May 1965, ElectroScience Laboratory, The Ohio State University Research Foundation; prepared under Contract AF 30(602) - 3269, Rome Air Development Center, Griffiss Air Force Base, New York. AD 623 077
19. Dybdal, R. B. , Rudduck, R. C. and Tsai, L. L. , "Mutual Coupling Between TEM and TE<sub>01</sub> Parallel-Plate Waveguide Apertures," IEEE Transactions on Antennas and Propagation, Vol. AP-14, No. 5, September 1966, pp. 574-580.
20. Karp, S. N. and Russek, A. , "Diffraction by a Wide Slit," New York University, Institute of Mathematical Sciences, Division of Electromagnetic Research, Research Report No. EM-75, 1955.
21. DeVore, R. V. and Kouyoumjian, R. G. , "The Backscattering from a Circular Disc," URSI-IRE Spring Meeting, Washington, D. C. , May 1961.

22. Ufimtsev, P. Ia. , "Approximate Calculation of the Diffraction of Plane Electromagnetic Waves by Certain Metal Objects II, The Diffraction by a Disc and by a Finite Cylinder," Zh. Tekh. Fiz. (USSR), Vol. 28, No. 11, (CC Trans. ), 1958, pp. 2604-16.
23. Kouyoumjian, R. G. , Notes in preparation for publication.
24. Harrington, R. F. , Time-Harmonic Electromagnetic Fields, McGraw-Hill Book Co. , Inc. , New York, 1961, p. 224 .
25. Richmond, J. H. , Notes in preparation for publication.
26. Franz, W. and Depperman, K. , "Theorie der Beugung Am Zylinder unter Berücksichtigung der Kriechwelle," Ann. Physik, Vol. 10, June 1952, pp. 361-373.
27. Franz, W. and Depperman, K. , "Theorie der Beugung der Kugel unter Berücksichtigung der Kriechwelle," Ann. Physik, Vol. 14, June 1954, pp. 253-264.
28. Senior, T. B. A. and Goodrich, R. F. , "Scattering by a Sphere," Proc. IEE, Vol. 111, No. 5, May 1964.
29. Kouyoumjian, R. G. , "An Introduction to Geometrical Optics and the Geometrical Theory of Diffraction," Antenna and Scattering Theory: Recent Advances Short Courses, Department of Electrical Engineering, The Ohio State University, August 1965 and August 1966.

30. Hong, S. , "Asymptotic Theory of Diffraction by Smooth Convex Surfaces of Nonconstant Curvature," Technical Report No. 2, The University of Michigan, Department of Electrical Engineering Radiation Laboratory, Contract AF 04( 694) -834, August 1966.
31. Keller, J. B. , and Levy, B. R. , "Diffraction by a Smooth Object," Research Report EM 109, New York University, December 1957.
32. Keller, J. B. , and Levy, B. R. , "Decay Exponents and Diffraction Coefficients for Surface Waves on Surfaces of Non-Constant Curvature," Symposium on Electromagnetic Theory, Professional Group on Antennas and Propagation, Institute of Radio Engineers, December 1959, pp. 552-561.
33. Kinber, B. Ye. , "Short-Wave Asymptotic Diffraction of Acoustic and Electromagnetic Waves from Surfaces of Revolution," Radiotekhnika, 1965, Vol. 20, No. 4, p. 101.
34. Kinber, B. Ye. , "Asymptotic Solution of the Problem of Diffraction by a Sphere," Telecommunications and Radio Engineering, No. 10, October 1966.

35. Moreland, J. P. , Peters, L. , Jr. and Kilcoyne, T. E. ,  
"Further Studies of Echo Area Contributions of Creeping  
Waves," Report 1815-5, 31 July 1965, ElectroScience  
Laboratory, The Ohio State University Research Foundation.
36. Kazarinoff, N. D. and Senior, T. B. A. , "A Failure of Creeping-  
Wave Theory," IRE Transactions on Antennas and Propagation,  
Vol. AP-10, No. 5, September 1962, pp. 634-638.
37. Voltmer, D. R. , Private communication.
38. Foch, V. A. , "Diffraction of Radio Waves Around the Earth's  
Surface," J. Phys. USSR, Vol. 9, No. 4, 1945, pp. 255-266.
39. Moffatt, D. L. , "Electromagnetic Scattering by a Perfectly  
Conducting Prolate Spheroid," Report 1774-11, 10 September  
1965, ElectroScience Laboratory, The Ohio State University  
Research Foundation; prepared under Contract AF 33( 615) -  
1318 , Research and Technology Division, Wright-Patterson  
Air Force Base, Ohio. AD 476 246
40. Ryan, C. E. , Jr. , "Memorandum on Analysis of Echo Area  
of Targets Using Geometrical Theory of Diffraction and  
Creeping Wave Theory," Report 2430-1, 22 May 1967,

- ElectroScience Laboratory, The Ohio State University Research Foundation; prepared under Contract F-19628-67-C-0318, Electronic Systems Division, L.G. Hanscom Field, Bedford, Massachusetts. AD 658 469.
41. Peters, L., Jr. and Ryan, C.E., Jr., "The Relation of Creeping Wave Phenomena to the Shadow-Zone Geometry," GISAT III Symposium, 1967.
  42. Peters, L., Jr., "Modifications of Geometrical Theory of Diffraction for Non-Cylindrical Curved Surfaces," Report 1815-2, 5 March 1965, ElectroScience Laboratory, The Ohio State University Research Foundation.
  43. Peters, L., Jr., "The End Fire Echo Area of Long Thin Bodies," IRE Transactions on Antennas and Propagation, Vol. AP-6, No. 1, January 1958.
  44. Blore, W.E., "The Radar Cross Section of Ogives, Double-Backed Cones, Double-Rounded Cones, and Cone Spheres," IEEE Transactions on Antennas and Propagation, Vol. AP-12, September 1964, pp. 582-590.



45. Bechtel, M. E. and Ross, R. A. , "Radar Scattering Analysis," Research Information Series, CAL Report No. ER/RIS-10, Cornell Aeronautical Laboratory, Inc. , August 1966.
46. Keys, J. E. and Primich, R. I. , "The Radar Cross Section of Right Circular Metal Cones," Defense Research Telecommunications Establishment, Ottawa, Canada, Report 1010, May 1959. AD 217 921
47. Bechtel, M. E. , "Application of Geometric Diffraction Theory to Scattering from Cones and Disks," Proc. of IEEE, August 1965, pp. 877-882.
48. Struik, D. J. , Differential Geometry, Addison Wesley Press, 1950.
49. Sommerfeld, A. , Optics - Lectures on Theoretical Physics, Vol. IV, Academic Press, New York, 1964, p. 245.
50. Hutchins, D. L. , "Asymptotic Series Describing the Diffraction of a Plane Wave by a Two-Dimensional Wedge of Arbitrary Angle," Ph. D. Dissertation, The Ohio State University, 1967.

UNCLASSIFIED

Security Classification

DOCUMENT CONTROL DATA - R&D		
<i>(Security classification of title, body of abstract and indexing annotation must be entered when the overall report is classified)</i>		
1. ORIGINATING ACTIVITY <i>(Corporate author)</i> ElectroScience Laboratory Department of Electrical Engineering, The Ohio State University, Columbus, Ohio	2a. REPORT SECURITY CLASSIFICATION Unclassified	2b. GROUP N/A
3. REPORT TITLE A Geometrical Theory of Diffraction Analysis of the Radar Cross Section of a Sectionally Continuous Second-Degree Surface of Revolution		
4. DESCRIPTIVE NOTES <i>(Type of report and inclusive dates)</i> Quarterly Report, 1 January to 31 March 1968		
5. AUTHOR(S) <i>(Last name, first name, initial)</i> Ryan, Charles E.		
6. REPORT DATE March 1968	7a. TOTAL NO. OF PAGES 180	7b. NO. OF REFS 50
8a. CONTRACT OR GRANT NO. F 19628-67-C-0308	9a. ORIGINATOR'S REPORT NUMBER(S) ESD-TR-68-211	
b. PROJECT NO.	9b. OTHER REPORT NO(S) <i>(Any other numbers that may be assigned this report)</i>	
c. TASK		
d.		
10. AVAILABILITY/LIMITATION NOTICES This document has been approved for public release and sale; its distribution is unlimited.		
11. SUPPLEMENTARY NOTES	12. SPONSORING MILITARY ACTIVITY Electronic Systems Division, Air Force Systems Command, United States Air Force, L. G. Hanscom Field	
13. ABSTRACT <p>The radar cross section of a continuous, convex, body of revolution composed of N sections, each section described by a second-degree equation has been analyzed using the geometrical theory of diffraction. Wedge diffraction has been applied to determine the scattered field due to discontinuities in slope between sections of the target, and creeping wave theory has been applied to determine the scattered field due to propagation of energy around the target. A solution for the diffracted field on an axial caustic is presented. An approximate solution for the scattered field near and at the normal direction to a conical generator is developed. A "simplified ray path geometry" for the creeping wave is presented and related to the scattering by spheres and prolate spheroids. The H-plane field of the sphere is calculated using creeping wave techniques for a ray geometry defined by the Poynting vector at the shadow boundary. The approximate creeping wave solution for the edge-on backscattering of disks is developed and applied to oval, circular and elliptical disks.</p> <p>The above techniques have been assembled into two computer programs for automatic computation of the radar cross section. These programs have been tested for cones, double cones, cylinders, conically capped cylinders, spheroids, and various prolate spheroid-sphere and prolate spheroid-oblate spheroid combination targets.</p>		

DD FORM 1473  
1 JAN 64

UNCLASSIFIED

Security Classification

UNCLASSIFIED

Security Classification

14. KEY WORDS	LINK A		LINK B		LINK C	
	ROLE	WT	ROLE	WT	ROLE	WT
Radar Cross Section Diffraction Theory Creeping Wave Theory Geometrical Optics Sectionally Continuous Target of Revolution						

INSTRUCTIONS

1. **ORIGINATING ACTIVITY:** Enter the name and address of the contractor, subcontractor, grantee, Department of Defense activity or other organization (*corporate author*) issuing the report.
- 2a. **REPORT SECURITY CLASSIFICATION:** Enter the overall security classification of the report. Indicate whether "Restricted Data" is included. Marking is to be in accordance with appropriate security regulations.
- 2b. **GROUP:** Automatic downgrading is specified in DoD Directive 5200.10 and Armed Forces Industrial Manual. Enter the group number. Also, when applicable, show that optional markings have been used for Group 3 and Group 4 as authorized.
3. **REPORT TITLE:** Enter the complete report title in all capital letters. Titles in all cases should be unclassified. If a meaningful title cannot be selected without classification, show title classification in all capitals in parenthesis immediately following the title.
4. **DESCRIPTIVE NOTES:** If appropriate, enter the type of report, e.g., interim, progress, summary, annual, or final. Give the inclusive dates when a specific reporting period is covered.
5. **AUTHOR(S):** Enter the name(s) of author(s) as shown on or in the report. Enter last name, first name, middle initial. If military, show rank and branch of service. The name of the principal author is an absolute minimum requirement.
6. **REPORT DATE:** Enter the date of the report as day, month, year, or month, year. If more than one date appears on the report, use date of publication.
- 7a. **TOTAL NUMBER OF PAGES:** The total page count should follow normal pagination procedures, i.e., enter the number of pages containing information.
- 7b. **NUMBER OF REFERENCES:** Enter the total number of references cited in the report.
- 8a. **CONTRACT OR GRANT NUMBER:** If appropriate, enter the applicable number of the contract or grant under which the report was written.
- 8b, 8c, & 8d. **PROJECT NUMBER:** Enter the appropriate military department identification, such as project number, subproject number, system numbers, task number, etc.
- 9a. **ORIGINATOR'S REPORT NUMBER(S):** Enter the official report number by which the document will be identified and controlled by the originating activity. This number must be unique to this report.
- 9b. **OTHER REPORT NUMBER(S):** If the report has been assigned any other report numbers (*either by the originator or by the sponsor*), also enter this number(s).

10. **AVAILABILITY/LIMITATION NOTICES:** Enter any limitations on further dissemination of the report, other than those imposed by security classification, using standard statements such as:

- (1) "Qualified requesters may obtain copies of this report from DDC."
- (2) "Foreign announcement and dissemination of this report by DDC is not authorized."
- (3) "U. S. Government agencies may obtain copies of this report directly from DDC. Other qualified DDC users shall request through \_\_\_\_\_."
- (4) "U. S. military agencies may obtain copies of this report directly from DDC. Other qualified users shall request through \_\_\_\_\_."
- (5) "All distribution of this report is controlled. Qualified DDC users shall request through \_\_\_\_\_."

If the report has been furnished to the Office of Technical Services, Department of Commerce, for sale to the public, indicate this fact and enter the price, if known.

11. **SUPPLEMENTARY NOTES:** Use for additional explanatory notes.
12. **SPONSORING MILITARY ACTIVITY:** Enter the name of the departmental project office or laboratory sponsoring (*paying for*) the research and development. Include address.
13. **ABSTRACT:** Enter an abstract giving a brief and factual summary of the document indicative of the report, even though it may also appear elsewhere in the body of the technical report. If additional space is required, a continuation sheet shall be attached.

It is highly desirable that the abstract of classified reports be unclassified. Each paragraph of the abstract shall end with an indication of the military security classification of the information in the paragraph, represented as (*TS*), (*S*), (*C*), or (*U*).

There is no limitation on the length of the abstract. However, the suggested length is from 150 to 225 words.

14. **KEY WORDS:** Key words are technically meaningful terms or short phrases that characterize a report and may be used as index entries for cataloging the report. Key words must be selected so that no security classification is required. Identifiers, such as equipment model designation, trade name, military project code name, geographic location, may be used as key words but will be followed by an indication of technical context. The assignment of links, rules, and weights is optional.